SOLIDIFICATION STUDY AND IMPROVED STRUCTURAL INTEGRITY OF ELECTROSLAG WELDS

Hee-Sung Ann
B.S., Hanyang University, Korea, 1978

A dissertation submitted to the faculty
of the Oregon Graduate Center
in partial fulfillment of the
requirements for the degree
Doctor of Philosophy
in
Materials Science and Engineering

August, 1987

The dissertation "Solidification Study and Improved Structural Integrity of Electroslag Welds" by Hee-Sung Ann has been examined and approved by the following Examination Committee :

Jack H. Devletian, Thesis Advisor
Professor

William E. Wood, Thesis Advisor
Professor

David G. Atteridge
Associate Professor

Russell Kremer
Associate Professor

ACKNOWLEDGEMENT

I express my appreciation and sincere thanks to Dr. J. H. Devletian and Dr. W. E. Wood for their valuable guidance and encouragement throughout this work. I also thank Drs. D. G. Atteridge and R. Kremer for their efforts in examining my dissertation.

I express my gratitude for the extensive help I received from Mr. R. B. Turpin, Mr. Dave Robert and graduate student fellows during this work. My sincere thank to Mr. D. Yu of my good partner for good cooperation during this work is greatly appreciated to complete the project successfully.

My sincere appreciation goes to Mr. Robin Churchill of the ESCO Corporation for his help in spectrographic chemical analyses of welds.

My appreciation also goes to my wife (Yeon-Sung Ann) for her assistance in the preparation of this dissertation.

I acknowledge the Federal Highway Administration of U.S. Department of Transportation for sponsoring this research work.

TABLE OF CONTENTS

LIST OF TABLES

LIST OF FIGURES

ABSTRACT

Solidification Study and Improved Structural Integrity
of Electroslag Welds

Hee-Sung Ann, Ph.D.
Oregon Graduate Center, 1987

Supervising Professors : Dr. Jack H. Devletian and
Dr. William E. Wood

Principles of solidification mechanics were applied to study solute band formation, dendrite reorientation and renucleation mechanisms during weld metal solidification of electroslag (ES) welds. Dendrite reorientation and renucleation were significantly affected by solute banding. Development of secondary and tertiary dendrite arms was dependent upon a unique combination of the temperature gradient vector and primary dendrite arm growth direction. Mechanisms were proposed to explain these solidification phenomena.

Mechanical properties of weld metal deposited by consumable guide electroslag welding (ESW) are controlled by the complex macro/microstructural features and impurity segregation developed throughout the weld. In order to understand this behavior, fundamental aspects in the design of high toughness welds in 50 mm and 76 mm thick A36 and A588 structural steels were investigated. Parameters such as voltage, current, gap size, welding speed, guide tube/plate designs, solid/tubular filler metals, flux variables (oxygen potential and basicity), and alloying additions (up to 2% Ni and 0.4% Mo in the filler metal) were examined and found to significantly influence the solidification structures, macro/microstructures, impurity segregation and fracture toughness of ES welds. From these comprehensive studies, five different characteristic grain

structures have been developed for electroslag welds, leading to new classifications for these welds.

Optimum conditions, based on parametric studies and macro/microstructure analysis in ESW, were determined with a narrow gap (19mm), unalloyed and wing or web guide plates. The optimum conditions provided increased welding efficiency, deposition rate, resistance to hot cracking, and improved microstructures.

Dramatically refined weld metal grain size was achieved in the as-welded condition by shielding the consumable guide tube or plate with a fused quartz sleeve. Intense stirring of the weld pool and significantly increased nucleation of polygonal and grain-boundary ferrite (due to excessive a high density of oxide inclusions) were responsible for grain refinement.

Charpy V-notch (CVN) tests were carried out for selected optimized and non-optimized ES welds. A substantial increase in CVN toughness was observed in optimized welds. The quartz grain refined welds exhibited identical toughness values throughout the weld.

I. INTRODUCTION

The electroslag welding (ESW) process was originally developed at the Paton Electric Welding Institute, USSR, in the early 1950's[1]. The process was further developed in Czechoslovakia (Bratislava Institute of Welding) and Belgium (Arcos Corporation)[2]. The technique eventually was introduced into the United States in 1959 by the Arcos Corporation[3]. Since then, it has been used in the U.S. for heavy structure fabrications, which include highway bridges.

A. Electroslag Welding Process

Electroslag welding is a joining method in which a molten slag simultaneously melts the filler metal and the surfaces of the work to be welded. Both the molten weld pool, which is shielded by the molten slag, and the molten slag extend along the full cross section of the joint as the weld progresses. Copper shoes are used on both sides of the plates being welded to contain the molten pool during welding and provide the final weld contour.

The process is initiated by an electric arc between the electrode and the bottom of the joint. Powdered flux is then added and subsequently melted by the heat of the arc. The arc stops and the welding current (500 to 700A) passes from the electrode through the slag by electrical conduction once a layer of molten slag is established (3.5 to 5 cm). The passage of the current provides the necessary heat for fusion. Electroslag welds are usually prepared in the vertical or the near-vertical direction and utilize a starting sump and runoff block to eliminate defects associated with the initiation and the termination of

the process.

The two types of electroslag welding are : a) conventional, and b) consumable guide. The conventional system utilizes a nonconsumable contact tube to direct the electrode into the molten slag pool. The contact tube is maintained about 50 mm above the slag pool surface. The entire welding head, along with the containment shoes, is moved upward at a predetermined rate consistent with the welding speed.

The consumable guide electroslag welding system uses a stationary consumable tube to guide the welding electrode into the slag pool (Figs. 1 and 2). The guide tube runs from the top of the weld to the bottom of the weld and is positioned with its tip about 37 mm above the bottom of the joint for weld initiation. As the name implies, the guide tube is consumed into the weld pool as the weld progresses. This method requires no moving parts except the welding electrode.

Electroslag welding offers the greatest productivity and cost effectiveness of any welding technique for joining thick section steel[4, 5]. However, ESW requires a large heat input, typically on the order of 100 KJ/mm for a 50 mm thickness plate, which results in a high base metal dilution (BMD) and a coarse weld grain structure. Multizoned weld metal structural features ranging from coarse to fine columnar grains and variable grain orientations(Fig. 3)[4, 5] lead to nonuniform weld properties. These structural variations combined with centerline segregation promote hot cracking of electrslag weldments.

As a result, the use of electroslag weldments has been prohibited on main structural tension members on any Federally-aided project[6]. However, due to the importance of this process for economical fabrication of large bridge components, the Federal Highway Administration has

undertaken several research programs to study and improve process control as well as to increase impact and fatigue properties.

B. Overview of Previous Study

This section presents an overview of the prior Oregon Graduate Center study results[4-5].

1. Weld Metal Solidification

The solidification structures for both standard weld and narrow gap, high current weld were revealed. The solidification structures for both welds were of cellular morphology with the average cell spacing in the narrow gap, high current weld 50 % smaller than in the standard weld.

2. Welding Variables

Several process variables exerted a strong influence on the resulting electroslag weld and on weld consistency and quality. The first process variable studied was guide tube centering for either single or double grounding. Grounding both plates, positioning the guide tube (electrode) within 1.5 mm from the geometric center of the joint gap, and eliminating electrode cast provided a symmetrical weld with equal penetration into both of the plates.

A second process control variable was the slag level. The slag level used during welding and the constant maintenance of this level (around 3.5-4.0 cm) were critical in establishing and maintaining steady-state welding conditions. Current and voltage fluctuations associated with intermittent flux additions were avoided by using a continuous flux feeding device.

Operating characteristic of the standard ESW consumable guide

technique were compared with those for narrow gap welding with a cylindrical guide tube, and with those for winged guide tube welding in a standard and a narrow gap configuration. The operating characteristics included voltage, current, and joint gap. The use of the winged guide tube design had the potential for reducing the susceptibility of electroslag welds to lack of penetration defects due to its shape symmetry with the joint gap.

The welding voltage was found to essentially control weld penetration and had a direct effect on the propensity for lack of edge penetration defects. The welding current had a minimul influence on the base metal dilution.

The high current, narrow-gap, winged guide tube welds were produced exhibiting about 50 % of the heat input of that required for standard welds. The welding time was also reduced to 1/3 of that required for the standard procedure, while the fusion zone width of the high current, narrow-gap, winged guide electroslag weld was much smaller than that of the standard weld. A marked reduction in the coarse-grained HAZ width was also achieved in high current, narrow-gap, winged guide electroslag welds

3. Weld metal microstructures

Structural steel electroslag welds are known to exhibit a high degree of undesirable solidification segregation and grain growth with undesirable microstructural constituents. Three basic approaches to modifying fusion zone microstructure were successful. One was the use of high current, narrow-gap, winged guide welds. significant refinement for high current, narrow-gap, winged guide welds, and the proeutectoid

ferrite films bordering the grain boundaries were well dispersed as opposed to continuous films present in standard welds. The second approach was quartz-shielded guide tubes. The use of quartz-shielded cylindrical guide tubes essentially eliminated fusion zone coarse columnar structure and resulted in a thin columnar structure across the complete fusion zone. The third approach was to add alloying elements to the filler material to suppress proeutectoid ferrite formation. Alloying element combinations made with Cr-Mo were added as weld wire filler metal. The microstructures consisted of a bainitic structure.

4. Charpy V-Notch Impact Toughness

Mechanical property assessment of electroslag welds is complicated by two major factors : a) the extreme anisotropy of the weld structure, and b) the very large grain size commonly associated with electroslag welds. The use of the narrow gap, winged guide tube technique increased the impact properties. The average impact value of the 2-1/4 Cr : 1 Mo weld wire weldment was over 20 Joules at $-18^{\circ}C$. The HAZ 1 impact energies showed considerable scatter and average HAZ 1 value was below 20 Joules at -18° C.

The prior studies, performed at Oregon Graduate Center[4, 5], addressed the fundamental relationships between process variables, microstructure, and properties of electroslag welds. The study of solidification structures is very important in electroslag weldments, because impurity segregations are controlled by solidification structures. In electroslag welding, the maximum temperature gradient is constantly changing direction as the heat source moves. Dendrites in

welds grow along the <100> direction and growth follows the steepest temperature gradient[7]. Since the maximum gradient vector is changing, it is often necessary for dendrites to change growth direction. However, the mechanism by which dendrites are reoriented and renucleated during solidification (to follow the changing temperature gradient) is not fully understood[8]. The methodology developed under prior studies in Oregon Graduate Center was not fully demonstrated and understood. The process was not fully optimized nor were limits defined.

The objectives of this investigation are therefore :

1) to determine the mechanisms which influence the dendrite reorientation, and renucleation during weld metal solidification

2) to study the effects of process variables, oxygen potential of the slag and minor alloying additions (Ni and Mo) on the solidification structure, and macro/microstructure and

3) to determine if innovative ESW procedures produce uniform, refined weld solidification structures, microstructures, resistance to solidification hot cracking, and consistently defect-free welds.

II. BACKGROUND

A. Weld Metal Solidification

1. Initiation and Development of Substructures

Solidification in fusion welding starts at the fusion boundary of weld metal-base metal interface, where virtually perfect wetting of the base metal occurs. Initial solidification characteristics in a molten weld pool have been studied by Savage et al.[9] and others[10-11]. They concluded that the nucleation event was insignificant, that epitaxial growth occurred from the unmelted base metal.

Solidification structures developed in weld metals are planar, cellular, cellular dendrites, columnar dendrites, and equiaxed dendrites(Fig. 4)[12]. Solidification structures directly depended on the solid interface growth rate (R), liquid temperature gradient (G) and solute content at the solid-liquid interface (Co)(Fig. 5). More detailed analysis of the conditions during weld metal solidification revealed that the following factors governed solidification structures development[13] : a) thermal gradient, b) growth rate, c) amount of supercooling, d) amount of superheating, e) weld metal turbulence, f) solute concentration, g) growth rate uniformity, and h) base metal grain crystallographic orientation.

Undercooling near the solid-liquid interface effects the growing interface and is a critical factor in solidification structure development. The overall undercooling (ΔT) can be expressed as the sum of three components[14] :

$$\Delta T = \Delta T_D + \Delta T_\sigma + \Delta T_K \qquad (1)$$

where ΔT_D , ΔT_σ , and ΔT_K are undercoolings due to solute accumulation, interface curvature, and interfacial kinetics, respectively. ΔT_σ and ΔT_K are, for metals, usually assumed to be negligibly small. Thus, the undercooling at the solid-liquid interface can be estimated by only considering solute accumulation at the interface[13, 15-16]. The constitutional supercooling (undercooling) due to solute accumulation introduced by Tiller et al. was[8] :

$$\frac{G}{R} = \frac{m_L C_o}{D_L} \frac{1 - k}{k} \qquad (2)$$

where G, R, m_L , C_o , C_I , D_L and k are temperature gradient in the liquid at the interface, growth rate of solid-liquid interface, slope of the liquidus line, composition of bulk liquid, composition at the solid-liquid interface, diffusion coefficient of solute in the liquid, and equilibbrium partition ratio (C_s/C_L), respectively. There is a lower limit below which the interface is unstable, which results in a cellular or dendritic solidification structures.

Fig. 6 summarizes the influence of growth rate of solid-liquid interface (R), the width of solute diffusion zone (δ), thermal super cooling (ΔT), effective liquidus temperature, and temperature gradient (G) on the region of constitutional supercooling.

The solute diffusion length (δ) ahead of the interface can be defined[17] as

$$\delta = \frac{2 D_L}{R} \qquad (3)$$

The solute diffusion length ahead of the interface is smaller (δ_1) in higher growth rate (R_1)(Fig. 6). Thus, effective liquidus temperature is steeper in higher growth rate. The growth rate of solid-liquid interface

(R) can be expressed as

$$R = V_W \cos \theta \qquad (4)$$

Growth rate of solid-liquid interface is different at all points of weld pool boundary as illustrated in Fig. 7.

The degree of thermal supercooling, which is controlled by local heat extraction, determines the actual temperature gradient. The larger the thermal supercooling (T_1 in Fig. 6), the larger temperature gradient (G_{L1} in Fig. 6). Thus, the conditions for a high degree of constitutional supercooling (small value of solute diffusion length) are fast welding speed (fast growth rate)(Eq. 3 and 4) and low thermal supercooling (low temperature gradient). The near-fusion-line region of the weld is normally associated with slow crystal growth and high temperature gradient, Thus, constitutional supercooling is likely to be low and the final structure is expected to be planar and cellular type (Fig. 5). The weld center region is just the opposite case of fusion line region. The structures are expected to be columnar and/or equiaxed dendrites depending on the degree of constitutional supercooling.

Fig. 8 further illustrates the effect of alloy addition on constitutional supercooling. Alloy additions promote the degree of constitutional supercooling, because alloy additions decrease the effective liquidus temperature and increase the steepness of curve as illustrated in Fig. 8.

2. Effect of Weld Puddle Shape

The maximum temperature gradient in fusion welding process is constantly changing direction as the heat source moves. Dendrites in

welds grow along the <100> direction and growth follows the steepest temperature gradient. Since the maximum gradient vector is changing, it is often necessary for dendrites to change growth direction. The frequency of variation in the dendrites direction of growth depends on weld pool shape. A nearly circular weld pool shows more frequent changes in dendrite growth direction, compared to kite shaped weld pool, because the maximum temperature gradient changes significantly from point to point in a nearly circular weld pool[18]. This requires dendrites to renucleate or reorient along more appropriate growth directions.

3. Dendrite Reorientation and Renucleation

In solidification, the dendrites try to change their direction of growth due to changing temperature gradient as discussed earlier. Savage et al.[18] and Arata et al.[19] observed dendrite reorientation at solute bands. Solute band in welds is caused by the non-uniformity of mixing in the molten pool and is very common in fusion welds because of the periodicity of the growth rate. Yoshimura et al.[20] found two kinds of relationships between the dendritic structure and solute band. The first involved the growth of dendrites through the solute band. The second type involved the nucleation and growth of new dendrites when the old dendrites entered a new band. They also found microsegregation at the bands by electron-microprobe analysis.

D'Annessa reported[21] that the molten pool turbulence and fluctuation significantly affected the competitive growth process, permitting favorable growth orientations to more conveniently win out over less favorably oriented ones. The possibility that dendrite fragmentation occurs by dendrite arm remelting has been suggested by

several investigators[22-26]. This remelting is thought to be due to solute accumulation, which drops the local solidification temperature. The melted-off dendrite arms are removed by liquid flow resulting from the local temperature gradient difference. Dendrites which survived fragmentation continue to grow in preferred growth orientations along the existing temperature gradient. This results in dendrite reorientation.

Dendrite bending and broken-off dendrites due to molten pool fluctuation have also been reported[27-28]. Dendrite bending is defined that dendrite grows straight following preferred growth direction and changes growth direction in another preferred growth direction by kink motion. In addition, dendrite curving has been observed in casting ingots with stirring[29]. Curved dendrite is a hook-shaped dendrite which is caused by continuous change of growth direction of dendrite. Fig. 9 illustrates dendrite curving with forced liquid flow in an electromagnetic stirring ingot. However, dendrite curving has not been observed in welding until this investigation.

Nakagawa et al.[22] observed that when the direction of maximum temperature gradient was different from primary dendrite growth direction, the primary dendrite arms diminished and secondary dendrite arms having only one direction toward the maximum temperature gradient developed. Devletian et al. [30] also observed a similar phenomena in capacitor discharge welding. Kato, et al.[31] reported that when the angle between the primary dendrite growth axis and the heat flow direction exceeded a critical value (15° to 30°), growth morphology changes from dendritic to a platelike structure.

4. Solute Band Formation

A number of mechanisms have been proposed for solute band formation. The essentials of these various mechanisms are considered below :

1) Growth rate change ;

A pulse type of solidification proceeds because of solute build up ahead of the interface to allow rapid solidification[32] (step one) and solidification halt due to the removal of supercooling at the solid-liquid interface by the rapid evolution of latent heat[32-33](step two).

D'annessa reported local periodic solidification rate variations due to a retardation in growth of primary dendrite arms caused by heat evolution during branching of secondary arms[21]. Arc force and heat input changes due to electrical fluctuations in the power supply cause periodic changes in solidification rate[12, 21, 27]. Finally, fluctuations in weld pool turbulence due to downward streaming of shielding gas have also been reported to cause solute bands[12, 34].

2) Hydrodynamic consideration

D'Annessa [27] proposed that solute segregation between interdendritic growth projections takes place by liquid flow. If the projections grow a finite distance into the liquid, vortices are likely to be generated in the depressions of the surface. These vortices can accentuate the segregation of solute by cavitation effects (Fig. 10).

3) Molten base metal penetration

The depth of the stagnant boundary layer (shown by the dashed line above the solid-liquid interface of Fig. 11) is controlled by the amount of convective mixing in the liquid metal, which, in turn, is controlled

by the depth of the molten pool in ESW process[35]. In general, increasing the welding speed increases the pool depth and decreases the thickness of the boundary layer (due to more effective convective mixing). The time available for the molten layer of base metal to slide into the weld pool is also decreased(Fig. 9). Projections of unmixed molten base metal into the molten metal pool become shorter and thinner as welding speed is increased. The opposite is true with decreasing the pool depth.

5. Dendrite Arm Spacing (DAS)

DAS and microsegregation are closely related to homogenizing kinetics [36]. The primary and secondary DAS decreases exponentially with increasing cooling rate (GR) or decreasing local solidification time (t_f)[37-39] according to :

$$DAS = f\ (\ GR\ )^{-n} = f\ (\ t_f\ )^{n} \qquad (5)$$

where the exponent n is in the range of 1/3 to 1/2 for secondary dendrite arm spacing and generally very close to 1/2 for primary dendrite arm spacing.

The effect of alloy content on DAS is not well established. Conflicting experimental results indicate that increasing alloy content can increase[16, 40-42], decrease[43-46] or have no effect[47] on DAS.

The effect of liquid flow on primary DAS has been investigated[48-49]. Liquid flow, which promoted solute mixing, caused the primary DAS to become larger because of inverse solute segregation. Takahashi et al.[50], however, showed that dendrites had smaller primary DAS when grown in a flowing melt. They measured the arm spacings as a

function of flow rate and distance from the chill. Fluid flow changed the local solidification variables such as the temperature gradient and cooling rate from those prevailing in a stagnant melt condition, which led to a decrease in DAS.

B. Process Variables of Electroslag Welding

The major objective for weld process control is to achieve the optimum conditions under which minimal penetration can be obtained without lack of fusion or overheating of the HAZ.

The interaction of the welding parameter variables, namely current, voltage, flux conductivity, joint gap, electrode types, electrode positioning, slag depth, guide tube geometry, and welding speed determines the final characteristics of the weld. Variations in one or more of these welding parameters result in significant variations in weld microstructures, uniform penetration, and properties. Hence, a complete understanding of the influences of these variables on the weld characteristics is necessary to produce welds with consistent structure and properties.

During ESW, the slag bath acts as a resistor in the circuit and the process operates purely on resistive heating. By the Ohm's law[51]

$$I = \frac{V \cdot Aeff \cdot \sigma}{\ell} \qquad (6)$$

where I, V, Aeff, σ, and ℓ are current, voltage, effective cross-sectional area of resistor (slag pool), specific electrical conductivity of slag, and length of resistor (defined as length between electrode tip and molten metal surface), respectively. In standard practice, ESW is performed using a constant voltage-dc power supply with reverse polarity mode. Reverse polarity mode indicates that the electrode is connected to positive terminal of power source(Fig. 1). Once the voltage is set, the current is directly influenced by joint gap (Aeff), flux chemistry, and electrode feed rate (welding speed). Flux chemistry and electrode feed

rate determine the specific electrical conductivity of molten slag (σ) and the length between electrode tip and molten metal surface (ℓ), respectively.

Heat input (H) is directly proportional to the base metal penetration and is a function of the voltage, current, and welding speed.

$$H = \frac{V \cdot I}{Vw} \qquad (7)$$

1. Welding Variables

Welding voltage has a major effect on heat input (Eq. 7), base metal penetration and on the stable operation of the ESW process. The voltage must be maintained within certain limits to optimize welding conditions.

If the voltage is too low, heat input is low(Eq. 7). In addition, short circuiting, or arcing to the molten metal pool may occur. Ohmic behavior (assuming constant current, cross-sectional area of slag pool and specific electrical conductivity of slag pool) requires a much lower effective resistance leading to electrode extension nearly to the bottom of the slag pool (Fig. 12). Most of the current will then flow from the tip of the electrode to the bottom of the slag pool providing less heat to be available for base metal penetration.

Too high a voltage may also produce unstable operation due to slag spatter and arcing on the top of the slag pool. High voltage causes a short electrode extension into the slag to maintain Ohm's law (Fig. 12). A majority of the heat will be generated near the top of the slag pool, much of which is lost by radiation. This causes less base metal penetration. Excessively high voltage eventually results in arcing at the slag surface[52]. As a result, voltage should be selected within an

optimum voltage range, where the electrode extends a moderate distance into the slag pool and the heat is primarily generated in the central region of the slag pool.

A linear relationship between the voltage and base metal dilution within certain voltage range and constant current was reported[4, 5, 53]. However, a parabolic relationship between voltage and base metal dilution was observed by Gurev et al.[54].

Welding current and electrode feed rate are directly related. Increasing welding current is accompanied by increased electrode feed rate and hence increased deposition rate (welding speed). Several investigators[4, 5, 35, 55] found a linear relationship between the current and electrode feed rate at a fixed voltage, but Frost et al.[56] reported that at constant voltage, the current was proportional to the square root of the electrode feed rate (Ve).

$$I = f\ (Ve)^{\frac{1}{2}} \qquad (8)$$

High currents can induce deep electrode extension into the slag pool (Fig. 12). This causes less heat to be available for base metal penetration because of heat concentration at the bottom of slag pool and the fast welding speed. However, low current can also produce less heat for base metal penetration due to short electrode extension into the slag pool (Fig. 12) and heat loss by radiation. Thus, the welding current (welding speed) must also be selected within an optimum range to maintain complete base metal penetration.

A linear relationship between the current and base metal dilution at constant voltage was reported[4, 5]. A non-linear relationship between base metal dilution and current at constant voltage has been

reported[52]. At lower current levels, increasing the welding current tends to slightly increase the width of the weld. Since the rise in the current is slower than the rise in the electrode feed rate at higher welding current range(Eq. 8), higher welding current reduces the energy input and decreases the weld penetration.

2. Joint Gap

Standard welding practice uses a joint gap of 32 mm[57]. The primary performance consideration is to provide guide tube clearance from the cooling shoes and weld members to avoid arcing. High speed consumable guide welds using welding gaps between 10mm and 19mm were reported with decreased heat input and improved properties[4, 5, 58, 59]. Vaidya et al. [59] proposed that the narrow gap approach had economic advantage of increasing welding speed. However, their results showed arcing problems.

3. Electrical Conductivity and Slag Volume

The electrical conductivity of the molten slag used in ESW was reported to be a primary factor in determining the heat generation efficiency[60]. The specific electrical conductivity of the slag is a function of both composition and temperature and depends on the concentration of cations available to carry the electrical charge and their mobility[51]. Generally, an increase in temperature or additions of CaF2 increases the electrical conductivity,

The conductivity of the slag (σ) changes with temperature (T) as follows[61],

$$\sigma = a + bT + cT^2 \qquad (9)$$

where a, b, and c are the constants for the slag. The empirical formula for the conductivity derived by Hara et al.[61] was

$$\sigma = \text{Exp}\,(1.911 - 1.38Nx - 5.69Nx^2) + 0.0039(T-1700) \qquad (10)$$

where $Nx = N_{Al_2O_3} + 0.75N_{SiO_2} + 0.5(N_{TiO} + N_{ZrO_2}) + 0.2(N_{CaO} + 2N_{CaS})$ and all N's represent component molar percent.

High slag resistance can restrict current flow and result in a cold slag bath. This promotes deep electrode extension into the slag pool. Low slag resistance allows excessive current flow, shallow electrode extension into the slag pool and exposed arcing (Fig. 12).

The slag pool must be deep enough for the electrode to extend into it and permit current to flow through the slag pool rather than by arcing to the molten slag pool surface. A shallow slag bath becomes too hot and results in low slag resistance(Eq. 9). This condition induces a shallow electrode extension (Fig. 12), which causes electrode feeding problems and a violent flux pool due to spitting slag and arcing between the electrode and the joint faces.

An excessively deep slag pool depth dissipates some of the heat produced by the welding current due to the greater contact area of heated base metal. This prompts pool circulation of the flux bath, a low slag temperature and a high slag resistance(Eq. 9)[62]. Deep electrode extension into the slag pool results(Fig. 12).

4. Electrode and Guide Tube Geometry

The electrode geometry and size also play an important role in controlling the heat distribution in the slag and the weld pools. As indicated by several investigators, a bend or a cast in the electrode

affects the heat distribution in the weld pool[63]. Thus, electrode straightening was essential to maintain symmetrical weld penetration about the weld axis.

Several investigators[4, 5, 63] showed that significant asymmetry occurred in the heat generation with off-centered electrode. This caused an excessive dilution in one plate while producing lack of fusion in the second plate. Venkataraman et al.[5] studied the effect of ground connections on symmetrical weld penetration about the weld axis in addition to electrode centering. They showed that when a single ground was used, weld penetration into the grounded plate was enhanced with either a centered or off-centered electrode. Grounding both plates, positioning the guide tube (electrode) within 1.5 mm from the geometric center of the joint gap, and eliminating electrode cast provided a symmetrical weld with equal penetration into both of the plates.

Both cylindrical and rectangular shaped strip electrodes were used in the past and Dilawari et al.[64] indicated a more efficient electrode melting with the use of strip electrodes.

The guide tube (or plate) is a key part in successful ESW. The standard consumable guide ESW utilizes a cylindrical guide tube to direct the welding electrode into the slag pool. In such cases, the guide tube and welding gap cross-sections are circular and rectangular, respectively. This combination leads to lack of penetration near plate edges when welding at low voltages and/or narrow gaps. Welding at high currents leads to resistance heating and warping of the guide tube due to limited current-carrying capacities.

Patchett[58] proposed using a guide plate with larger cross-sectional area to solve this problem. A wing guide tube design in which

rectangular fins were welded onto a cylindrical tube has been used by several investigators[4, 5, 58, 59]. A higher ratio of the guide to gap cross-sectional area helped to increase the welding speed. The wing guide tube also eliminated the necessity for electrode oscillation while welding thicker section materials[65]. Narrow gap welds could be made using the wing guide tube without edge penetration difficulties[4, 5, 66]. In addition, the wing guide tube could be used for welding plates with varying thickness.

Consequently, this method was a far more efficient way to distribute the heat across the slag bath and reduced the amount of filler metal while greatly increasing the current-carrying capacity. Finally, the guide tube/plate chemistry can be carefully manipulated to achieve the required weld properties since it constitutes a finite fraction of the weld metal.

5. Metal Powder Addition

An increase in welding speed was also achieved by several investigators through external metal powder additions to the slag pool[67-69]. The metal powder additions increased the metal deposition rate, thereby increasing the welding speed. The powder additions quenched the slag pool. Both of these effects lowered the heat input for the weld. The addition of alloyed metal powder was also used to decrease the heat input and improve properties[70].

C. Grain Refinement

ES welds generally have a large columnar grain structure which favors impurity segregation and solidification cracking. It is necessary to replace the columnar structure with an equiaxed one to reduce the hot-cracking problems and improve toughness. The different methods which lead to structure control are described as follows :

1. Inoculation

Inoculation by suitable nucleants has been used to produce fine equiaxed microstructures[71-74]. The requirements for nucleants are that nucleants should not melt in the molten pool, act as a delta-Fe nucleant and grain growth inhibitor. TiC promotes delta-Fe nucleation without melting due to stability in high temperature and inhibits grain growth in low carbon steels[71]. The most effective nuclei for delta-Fe were found to be TiN and TiC, SiC, ZrN and WC in order of decreasing effect[74].

The effective operation of this grain refining technique was shown to depend critically upon the rate of inoculant supply, the position of inoculation in the pool, the size of the inoculant powder and welding conditions[75]. In ESW, the introduction of artificial inoculants was concluded to be highly problematical since inoculants would not be expected to survive contact with the molten slag and molten metal for long times[76].

2. Molten Pool Stirring

Controlled stirring of solidifying melts is an important grain refining technique because crystal fragments generated by stirring are a prominent source of equiaxed crystals[84]. Various types of stirring

including electromagnetic, mechanical, ultrasonic and impact have been reported to produce grain refinement in solidifying castings and weldings[4, 5, 28, 29, 77, 78]. An alternative method to induce molten pool stirring was power supply variation. This was achieved by applying either a pulsed arc or current modulation, or even combination of the two[79, 80]. Campbell[81] has extensively reviewed the effects of vibration during solidification.

The mechanism of crystal fragmentation by stirring is believed to promote constitutional supercooling ahead of the growing dendrites through periodic fluctuations in the temperature gradient. The enhanced liquid motion can break the growing dendrite tips at the solid-liquid interface and sweep them out into the liquid where further solidification takes place from these fragments[23, 82].

In addition, molten pool stirring techniques to achieve grain refinement were developed for ESW[4, 5]. The techniques utilized shielding the consumable guide tube with either mullite or fused quartz. The basic concept of this process was to induce intense stirring of the molten pool by means of deep immersion of electrode into the molten slag pool. Some progress was reported with electromagnetic stirring of ES welds and with the use of ultrasonic vibration in ESW[8].

3. Cooling Rate

A rapid cooling rate supercools the solidifying weld metal considerably below the liquidus temperature and induces a high rate of nucleation[83]. In addition, the tendency toward finer DAS and equiaxed crystalization is favored by high freezing rates(Eq. 5)(Fig. 4). Also the critical degree of supercooling for the onset of equiaxed growth in a

molten pool is reached within a shorter distance with fast cooling rate[37].

Fast cooling rates can suppress transformation reactions and induce the formation of low temperature transformation products[84]. For plain C-Mn deposits, a high toughness and a low transition temperature can be achieved if the proportion of fine grained acicular ferrite is kept high and grain boundary ferrite and widmanstatten ferrite kept low. In general, the finer the plate size of the acicular ferrite the better the toughness in C-Mn and low alloy weld metals[85-94]. Harrison[88] reported the effect of cooling rate on acicular ferrite formation in Nb steel weldments. Increasing cooling rate was seen to increase the acicular ferrite and to refine the acicular ferrite grain size. The refinement was explained as due to the depression of transformation temperature which increased the nucleation to growth ratio.

4. Control by Oxygen Inclusions

Inclusion-assisted nucleation is a heterogeneous process like inoculation where interfacial energy (at the nucleating interface) and critical supercooling are the major controlling factors. Factors influencing the interfacial energy include chemical properties of nucleation agents, topography of the surface of nucleation substrate, and disregistry of crystal lattice between the two phases in the interface. The first two factors are not yet determined quantitatively. However, the lattice disregistry (δ) is well documented[95, 96]. Disregistry was expressed[96] as :

$$\delta = \frac{\Delta a_o}{a_o} \qquad (11)$$

where Δa_o is the difference between the lattice parameters of the substrate and the nucleated solid for a low index plane and a_o is the lattice parameter for the nucleated phase. The empirical relationship between disregistry and supercooling(ΔT) determined by Bramfitt[96] was

$$\Delta T = \frac{\delta^2}{8} \qquad (12)$$

The greater the disregistry between the substrate and the nucleating phase, the less effective the compound was in promoting nucleation.

The correlation of the increase in concentration of the oxygen inclusions and the onset of grain refinement suggested that these inclusions were the active nuclei in the melt for delta-Fe nucleation[71, 95]. Ohashi et al.[95] studied the effect of oxides on nucleation behavior and showed that the degree of critical supercooling in the case of rare earth metals (REM : La, Ce, Pr and Nd) addition was 3°C. This was small compared with the 14°C for Al2O3 addition, 30°C for SiO2 addition and 53°C for MnO addition. The minimum values of disregistry were 5% for REM oxides, 16.1% for Al2O3, 22% for SiO2, and 22.9% for MnO, which agreed with Bramfitt's relationship[96].

The effect of oxygen inclusions on room temperature microstructure has also been studied by many investigators[89-94, 98-104]. They suggested that oxygen inclusions in weld metal significantly influenced the transformation characteristics of weld metal. Kinetics and morphology of ferrite formation were changed by increasing the rate of nucleation of high temperature proeutectoid ferrite, particularly from austenite grain boundaries, to produce a fine grained structure of predominantly blocky and/or grain boundary ferrite. Ferrante et al.[102] demonstrated that the grain boundaries decorated by oxygen inclusions followed the

classical Zener precipitates-boundary interaction equation.

$$D_L = \text{Limiting grain size} = \frac{4r}{3f} \qquad (13)$$

where f and r are the inclusion volume fraction and inclusion radius, respectively.

Abson et al.[89] showed that inclusion size and type of distribution was substantially more important than the total inclusion volume fraction in influencing ferrite nucleation. Harrison et al.[99] reported that nucleation occurred on dislocations in the immediate vicinity of the inclusions rather than directly on the inclusion substrate. Strain fields can be produced within the matrix between a hard inclusion and a softer matrix. The dislocations produced in this manner not only had the normal advantages of providing nucleation sites, but also the region of matrix close to the inclusion might be depleted in alloying elements (such as Mn), making nucleation in this region energetically more favorable.

The role of non-metallic inclusions in the nucleation of acicular ferrite was demonstrated by Abson et al.[89] and Cochrane et al.[90] and was confirmed later by many other investigators[98-102]. An adequate number and appropriate dispersion of weld metal oxide inclusions (with a diameter around 0.3um) were an essential requirement for the nucleation of acicular ferrite. Thus, only the intermediate oxygen content (200-300ppm) produced a high volume fraction of acicular ferrite and refined weld metal microstructures[85].

5. Alloy Additions

Attempts to control the weld metal solidification structures as well

as the microstructures led to the introduction of welding consumables containing various alloying elements. Alloying elements present in the weld metal were either introduced deliberately through the filler electrode and flux or picked up from the base metal as a result of dilution.

Increasing the alloy content increases the constitutional supercooling, which induces earlier development of columnar or equiaxed dendrites. During solid state transformation, some elements helped to stabilize the austenite (austenite formers ; C, N, Mn, Ni, Cu and Zn) and others stabilize ferrite (ferrite formers ; Zr, Ti, P, V, Nb, W, Mo, Al, Si and Cr)[8]. Austenite stabilizers would be expected to delay the transformation to ferrite[105], whereas the role of strong carbide formers such as Cr and Mo would have more complex effects because of their effects on interface mobility as well as on the A3 temperature[8, 105]. But Cr and Mo were claimed to enhance transformation to acicular ferrite at the expense of proeutectoid ferrite[87]. Ni additions of up to approximately 3.5 % were considered to have a generally beneficial effect on increase of volume fractions of acicular ferrite [106, 107].

The role of each element was extensively discussed by Grong et al.[108], Dorschu[106] and Abson et al.[109]. However, the effects of various alloying elements on the austenite to ferrite transformation were inadequately explained and conflicting views are held about the major controlling mechanisms[108].

D. Mechanical Properties

Mechanical property assessment of electroslag welds is complicated by two major factors[4-6, 110, 111] : a) the extreme anisotropy of the weld structure, and b) the very large grain size commonly associated with electroslag welds.

Several investigators[4-6, 110, 111] have studied the CVN toughness of electroslag weldments. Charpy impact toughness evaluations of ES welds in general revealed low toughness values in both the weld centerline and the coarse grain HAZ [6]. None of several A588, standard gap (32 mm) electroslag weldments at weld center was capable of raising the average impact energy above 20 Joules at -18°C[4, 5].

The use of the narrow gap (19 mm), winged guide tube technique on A588 and A36 plates increased the impact properties. It increased the average impact values as well as increased the minimum impact values. The average impact value of the 2-1/4 Cr : 1 Mo weld weldment was over 20 Joules at -18°C, while the minimum value was 14 Joules [4, 5]. Culp[6] found that HSLA steel, A588, exhibited lower toughness than construction grade carbon steel, A36, due to weld metal chemistry and microstructure.

The HAZ impact energies showed that there was a considerable scatter and the minimum and average values were relatively independent of welding technique. The average HAZ value was below 20 Joules at -18°C[4, 5].

The design philosophy using transition temperature curves by Charpy toughness testing is the determination of a temperature above which brittle fracture will not occur at elastic stress levels. Obviously, the lower this transition temperature, the greater the fracture toughness of

the material. A common criterion to define the transition temperature was on the basis of an arbitrary low value of energy absorbed. As a result of extensive tests on world war II steel ship plates, it was established that brittle fracture would not initiate if the absorbed energy was equal to 20 Joules at the test temperature. A 20 Joules transition temperature has become an accepted criterion for low-strength steels for a design[112].

Several investigators [6, 110] believe that Charpy toughness evaluations don't rate welds in their true order, because the small size of Charpy specimens limits toughness information to several grains, especially in electroslag welds. Tuliani et al.[53] reported scatter in the CVN toughness along the weld length. This factor, as well as the small size of the charpy specimens, led to conflicting toughness results in certain weld evaluations. However, since full thickness KIc testing of the weldments was expensive and difficult, CVN test served as an initial qualification for ES welds.

III. EXPERIMENTAL PROCEDURES

A. Materials

The base metals used for this investigation included ASTM A36 and A588 structural steel plates in 50 mm and 76 mm thick sections. The wing and web guide plates were made of Type 1010 mild steel. The chemical compositions are given in Table 1. The microstructures of as-received plate materials are shown in Fig. 13.

The commercial Hobart PF 201 flux was used for starting and running in most welds. In order to improve the welding quality, high conductivity and low oxygen potential fluxes were introduced. Table 2 provides this information in detail. The basicity indices (B.I.) of the commercial and experimental fluxes were calculated by[103] :

$$B.I. = \frac{CaO + MgO + Na_2O + K_2O + \frac{1}{2}(MnO + FeO)}{SiO_2 + \frac{1}{2}(Al_2O_3 + TiO_2)} \qquad (14)$$

where each component is mole fraction.

Several electrode filler wires were used in this investigation. Low-carbon steel wire, Hobart 25P and Linde WS, respectively, matched the compositions of A36 and A588 base metals. To develop suitable alloy additions, Airco AX90, and Stoody TW8544 wires were deposited. Stainless steel wires, 17-4 PH, 309 and 304 were also utilized to study solidification phenomena. All chemical analysis data of the above filler metals are included in Table 1. All steel plates were ultrasonically tested to record the location of any rejectable indications.

B. Electroslag Welding

The standard welding head along with the flux feeding system, jet-line wire feed measuring device, oscillation mechanism, and a guide tube holder were mounted on one of the plates being welded. The rectangular shaped, modified consumable wing and web guide plates as well as a standard guide tube were centered in the various joint gaps (19 mm, 25 mm, and 32 mm). The configuration and dimension of the standard guide tube and the wing and web guide plates are shown in Fig. 14. All welds were made with a Hobart Model RC750, dc constant voltage power source using reverse polarity mode. The principle of this method is illustrated in Figs. 1 and 2. For the high conductivity and low oxygen potential flux, the flux was added manually at a rate of approximately 4 g/min, which was equivalent to automatic flux feeding by continuous flux adding device[4, 5]. All fluxes were baked for over 24 hours at 200°C in the furnace before use. Alloys were added to the ES welds by solid or tubular alloyed electrodes.

The methodology used to produce fine, uniform grain structures utilized a thin-walled quartz shroud placed around (a) the 12.5 mm diameter standard consumable guide, and (b) the rectangular shaped consumable guide plate (wing or web guide plates). A flare formed on the top edge of the quartz shroud facilitated securing the quartz to the guide tube (Fig. 14). This shroud provided a means for deep immersion and enhanced molten pool mixing by the electrode.

The methodology was used to produce standard gap (32 mm) and narrow gaps (25 mm and 19 mm) welds with different welding conditions in order to vary proper heat input and base metal dilution. Different electrodes

were also used for varying weld metal alloy contents. Quartz thickness and diameter were varied for use with the 12.5 mm diameter standard consumable guide to induce different degrees of molten pool stirring. Oscillation of the shrouded electrode was also studied. Different flux compositions were used to control oxygen transfer into the molten metal. In addition, current and voltage fluctuations were monitored during the welding process to detect and analyze arcing. A record of these variations was made with a Gulton strip chart recorder.

Furthermore, the solidification behavior of a limited number of GTAW welds was characterized. 304 stainless steel filler was deposited on the A36 base metal using GTAW and the welds were used for a solidification study, especially for the study of dendrite reorientation, and renucleation phenomena. Intensive molten pool stirring was induced by weaving the GTAW arc torch.

C. Weldment Evaluation

1. Metallography

Longitudinal and transverse section specimens were etched with a 10% nital solution to expose the macrocharacteristics of weld metal and HAZ. The microstructure of each weldments was evaluated using longitudinal and transverse section specimens. Solidification structures were revealed by a Stead's reagent with the following composition : 5g $CuCl_2$, 20g $MgCl_2$, 10ml HCl and 500 ml methanol. Solid state transformation products were examined by etching in a 2 % nital solution at room temperature. A subsequent light repolishing with alumina revealed the solidification substructure. In addition, the number and size of inclusions on selected

welds were measured by microscopical examination of the polished and unetched specimen.

Stainless steel welds deposited on A36 base metal by ESW and GTAW were sectioned longitudinally. After fine grinding and polishing, jet electro-etching of stainless steel welds were done using an electrolyte of 33 % water, 55 % phosphoric acid and 12 % sulfuric acid with 1.5 to 2V for 60 seconds. In addition, Stead's reagent was also applied. Dendrite structures of stainless steel welds were revealed by this both methods.

The base metal dilution (BMD) was measured on the transverse section and calculated by means of the expression :

$$BMD\ (\%) = \frac{bw - bg}{bw} \times 100 \qquad (15)$$

where bw, and bg are width of weld and joint gap, respectively. bg is taken as the mean value of measurements at the edges and at the center of the weld. Base metal penetration was measured at maximum sidewall weld metal penetration. A form factor (W/d), which is the ratio of the maximum weld pool width to its depth, was measured on the longitudinal section. The proportion of coarse columnar grain zone (CCG) was measured on the transverse section and calculated by :

$$CCG\ (\%) = \frac{Wm - Wt}{Wm} \times 100 \qquad (16)$$

where Wm and Wt are maximum size of weld width and weld width of thin columnar grain zone, respectively. The uniformity of penetration and HAZ widths were also measured on the transverse section.

2. Chemical Analyses

Chemical analyses of the base metal and selected welds were carried

out using a spectrographic analyzer. Oxygen and nitrogen potential of the base metal and selected welds were also determined. The International Institute of Welding (IIW) carbon equivalent (C.E.) was calculated on selected welds by :

$$C.E = C + \frac{Mn}{6} + \frac{Cr+Mo+V}{5} + \frac{Cu+Ni}{15} \qquad (17)$$

where the amounts of each element are given in weight percent. This equation was reported to be suitable for around 0.18% C and long cooling times[113].

3. Electron Probe Micro-analysis (EPMA)

The EPMA was utilized to reveal significant segregation detail. Selective scanning techniques coupled with metallographic data were used to obtain concentration profiling of substructure for quantitative analysis.

4. Hardness

The hardness was measured across the weld fusion zone, HAZ and base metal using a Rockwell B scale hardness tester. A C scale measurement was made whenever the hardness value exceeded Rb 100. In addition, Knoop micro-hardness testing was also applied to determine the hardness of segregated regions in weld metal. Also Knoop indentations were used to identify locations in weld metal for subsequent EPMA studies.

5. Charpy Impact Testing

Standard ASTM E23 Charpy impact specimens were machined in weld

locations and were tested individually in a 264 ft-lb Tinius Olsen pendulum type instrumented impact testing machine. The V-notch was ground perpendicular to the welding direction. Notches were located in the mid-thickness for the weld zone. The notch was precisely located by etching of the weld prior to sectioning.

Impact tests on these welds were conducted over a temperature range of -73 °C to +65 °C to determine the temperature transition characteristics. Two or three samples were machined for each test temperature, except the -18°C test for which 6 samples were machined.

Selected welds were also machined and notches were located in three regions, namely weld centerline, thin columnar grain, and coarse columnar grain (Fig. 15). A total of 6 samples were used for this test and were performed at -18°C.

6. Scanning Electron Microscopy (SEM)

SEM, using a JEOL (JSM-35) at 25Kv and a 39 mm working distance, was done on selected CVN specimens to reveal the fracture morphology and on radial type cracks of weldments to determine whether the crack was solidification-induced hot cracking or not. The surfaces of selected specimens were cleaned ultrasonically in acetone.

IV. RESULTS

A. Dendrite Reorientation and Renucleation during Weld Metal Solidification

Dendrites in welds grow along the <100> direction and growth follows the steepest temperature gradient. Since the maximum temperature gradient vector is changing as the heat source moves, it is often necessary for dendrites to change growth direction.

Dendrites were significantly affected by solute bands which facilitated reorientation of the growth direction parallel to the changing gradient vector(Fig. 16). Several dendrite characteristics were observed at the solute bands(Fig. 17) : a) direct dendrite arm growth through solute banding b) dendrite arm bending (dendrite arm kink) c) partial or complete dendrite arm melting d) new dendrite arm nucleation and e) change of dendrite morphology. Dendrite arm spacing (DAS) varied at the solute bands. DAS was finer, especially after growth passed through the white-etching band of a solute enrichment layer (Fig. 18).

One interesting observation in this investigation was the hook-shaped dendrite curving observed in welds deposited by GTAW (Fig. 19). The curving direction was the same as the direction of the tungsten electrode (travel). Metallographic studies showed that the curved dendrite was within the solute depletion dark band, while equiaxed dendrites developed in the solute enrichment white band near the weld center line, as shown in Fig. 19. This was in agreement with Bridge et al's observation[29] of dendrite structure change during electromagnetic stirring of strand-cast steel. Dendrite curving was not found in

electroslag welds primarily because of the insufficient temperature gradient and convection developed in ESW.

The development of tertiary dendrite arms (Fig. 20) in stainless steel welds deposited by ESW developed when the maximum temperature gradient vector was substantially different from the easy growth <100> direction. This same phenomenon was also observed in mild and low alloy electroslag welds. Because of this orientation difference between the primary dendrite arms and the temperature gradient vector, secondary side arms became dominant and developed tertiary side arms.

Alloying of mild steel ES welds significantly affected the morphology of the dendrite structures as displayed in Fig. 21. In mild steel welds having a fairly deep molten pool, primary dendrites grew straight toward weld center with the secondary dendrite arms growing preferentially toward heat source. As the alloy content and constitutional supercooling increased, the transition from columnar to equiaxed dendrites was promoted. Perfect equiaxed dendrites developed and grew with fast welding speed, alloy addition, and extremely low temperature gradient.

Solute bands occurred near the edge or the fusion line of the weld and diminished in intensity with increasing distance toward weld center. The solute band spacing and width near the fusion line of the weld was considerably smaller than the band spacing and width near center of the weld. The frequency of solute bands was greater near the edge of weld than toward the center of the weld. High form factor welds showed a higher density of solute bands and greater band penetration toward the weld center.

In the mild steel ES welds, a polygonal ferrite-rich, white etching

band was visible. This band was formed due to nucleation of polygonal ferrite in the solute-rich layer. However, in Ni-Mo alloyed ES welds, the polygonal ferrite nucleated at the solute depletion layer which represented the dark-etching band.

The Knoop hardness and electron probe micro-analysis (EPMA) study was performed to quantitatively characterize the solute segregation across the bands and dendrites. In mild steel electroslag weld specimens taken midway between fusion line and weld center, the hardness of the dendrite core averaged 79 Rb (converted to Rockwell from Knoop) and interdendritic space averaged 84 Rb. The relative concentration of Mn by EPMA in the interdendritic region was 23% higher than that of dendrite core.

Hardness variations across several solute bands near the fusion line in Ni-Mo alloyed welds were also determined. The soft dark band averaged 90.5 Rb as compared to the hard white band (94.5 Rb). Microprobe analyses of the solute bands near the fusion line also indicated that the darkened region was around 12% lower in Mn than the white region (etched with with Stead's etchant). The darkened region also appeared to be low in other solute elements. The concentration and hardness variations across the bands were associated with periodic changes in solidification rate.

B. Classification of Weld Structures

A new classification system representing five different types of grain structures produced in A36 and A588 weldments deposited by the ESW process are illustrated in Fig. 22 and Table 3. The characteristic structures were dependent upon welding parameters, alloy content and inclusion or oxygen content of the weld.

Type I weld structure consisted of only fine-grained, thin columnar crystals throughout the weld. Type II welds contained an outer zone of coarse columnar grains and an interior zone of thin columnar grains. Type III welds consisted of only coarse columnar grains throughout the weld. Type IV welds possessed not only the coarse and thin columnar grains (as in Type II), but also a zone of equiaxed grains in the weld center. And Type V welds contained an interior zone of equiaxed grains and a zone of thin columnar grains at the weld edges.

1. Type I

This weld structure, illustrated in Fig. 22, was obtained by applying high oxygen potential fluxes(made with over 40 wt.% SiO2, silicate manganese) resulting in weld metal oxygen concentrations exceeding about 600 ppm (Table 4). The size and number of non-metallic inclusions were determined and found to increase with increasing weld metal oxygen potential(Fig. 23), as expected, since the oxygen content is directly related to the volume fraction of oxide inclusions. The solidification structures were found to be equiaxed dendrites at the weld center(Fig. 22). The high volume fraction of oxide inclusions strongly favored producing a fine grained structure of predominantly blocky and grain-boundary ferrite(Figs. 22 and 23).

2. Type II

This weld structure was generated under normal welding conditions (including commercial welding practice) using a mild steel electrode, neutral flux and either standard or narrow gaps (Table 3). Solidification of Type II welds was characterized by cellular dendrites dominating near the weld edges and columnar dendrites near the weld center (Fig. 24). The cellular dendritic structure was associated with coarse columnar austenite grains which transformed to large amounts of acicular ferrite. The columnar dendritic morphology prevented lateral grain growth of austenite resulting in the thin columnar structure which transformed predominantly into blocky and grain boundary ferrite(Fig. 25).

3. Type III

This fully coarse grained weld structure was produced by ESW with low oxygen potential and high basicity fluxes containing CaF2-CaO-Al2O3. The weld metal oxygen and sulfur content were typically only 80 ppm and 0.012 wt.%, respectively (a standard weld using a neutral flux would contain O2 : 250 ppm and S : 0.025 wt.%)(Tables 3 and 4).

Larger dendrite arm spacing with noticeable side arms was observed at the weld center(Fig. 22). The low oxygen and impurity levels in the interdendritic regions were insufficient to retard the grain boundary migration of austenite. Thus, virtually unrestricted lateral austenite growth during weld cooling produced a fully coarse grain structure. Fig. 26 illustrates macrostructures as affected by weld metal oxygen content. The reduced oxygen content decreased the amount of acicular ferrite nucleation while increasing polygonal ferrite(Figs. 22 and 27). Another

interesting fact was a noticiable reduction of widmanstatten ferrite throughout the weld.

4. Type IV

This weld was developed using a mild steel electrode, neutral flux and the highest values of current and welding speeds to produce an extremely deep weld pool with a form factor of only 0.9. This solidification structure was characterized by a small zone of equiaxed dendrites at the weld center.

Subsequent solid state transformations produced equiaxed grains containing large amounts of acicular ferrite and proeutectoid ferrite at prior austenite grain boundaries (Fig. 22). The equiaxed grain structure of the weld was so resistant to hot cracking that small radial type hot cracks (usually less than 6.4 mm in length) developed intergranularly in the thin columnar grain zone. Fig. 29 shows SEM micrograph of radial type cracks illustrating solidification induced hot cracks.

5. Type V

When the low alloyed filler metal (AX90 and TW8544) containing Ni and Mo was added to the medium and high oxygen welds, equiaxed dendrites at the weld center resulted without the aid of rapid welding speeds. Unlike Type IV, the equiaxed dendritic structure in Type V welds could occur at much lower growth rates and high temperature gradients. The solid state microstructure also showed equiaxed grains at the weld center with a high volume fraction of acicular ferrite(Fig. 22).

The role of the Ni-Mo alloy addition to the weld metal appeared to promote the following: (a) equiaxed dendritic and equiaxed ambient temperature grain structures around the weld center, (b) grain boundary

and blocky ferrite reductions, (c) acicular ferrite increases up to about 90%, and (d) elimination of the coarse columnar austenite grain structure near the fusion line. The Ni-Mo alloying additions tended to reduce the nucleation rate of high temperature transformation products (blocky, grain boundary and widmanstatten ferrite). The Ni-Mo alloy additions provided the further benefits of substantially increased resistance to hot cracking because of the development of equiaxed grains in the weld center zone.

C. Slag Conductivity

The electrical conductivity of the slag was calculated using an empirical formula(Eq. 10)[61]. Fig. 28 illustrates the marked influence of the slag conductivity on the base metal dilution produced during ESW and also clearly demonstrates the optimum conductivity of slag for the highest welding efficiency which is around $3/(\Omega cm)$ at 1700°C. Welding efficiency (P) is defined as[114] :

$$P = \frac{Vw\ bw}{4a} \qquad (18)$$

where Vw, bw, and a are welding speed, weld width, and thermal diffusivity, respectively.

Excessive slag conductivity produced a small exposed arc between the guide tube and surface of molten slag, while highly resistive slags tended to develop a submerged arc between the electrode and weld pool (Fig. 12). In either case, arcing wasted energy and reduced efficiency. Thus, there was an optimum slag conductivity that produced the most efficient ohmic heating of the slag as shown in Fig. 28.

D. Narrow Gap, High Deposition Rate ESW

The joint gap directly controls the heat input of the weld per unit thickness of plate since the welding speed is a function of the volume of filler metal that is required to fill the weld joint cavity in ESW. Thus, in this study, a combination of narrow gap (19 mm), high welding current and rectangular shaped modified guide plates were selected and used to decrease the heat input, refine the weld metal microstructures and improve the mechanical properties. The commercial neutral flux (PF 201) was applied, because it provided optimum oxygen potential (200-250 ppm) in the weld. Only mild steel electrodes (25P and WS of Table 1) were utilized in this study. The narrow gap welding parameters were studied and optimized to produce the greatest weld toughness while maintaining sufficiently high form factors to ensure good resistance to solidification hot cracking.

1. Functional Relationships between Welding Variables

Heat input was directly proportional to the base metal penetration within the limits of this study as shown in Fig. 30. A substantial decrease of heat input was observed for the narrow gap versus the standard gap ESW process, primarily because of the increased welding speed and decreased joint gap spacing.

The base metal dilution (BMD) increased exponentially with increasing voltage at a fixed current as shown in Fig. 31. The BMD was slightly higher in narrow gap welds compared to the standard weld of 50 mm thick plate (compared at 40 V). Figure 31 also indicates the onset of lack of fusion. The exponential character of BMD at higher voltages

(Fig. 31) was probably due to shallow extention of electrode into the slag pool at high voltages. This resulted in initiation of exposed arcing at the top of the slag pool and loss of heat near the top of the slag pool by radiation(Fig. 12).

A non-linear relationship between BMD and current was also observed at a given voltage. BMD increased with increasing current at a low current range and decreased with increasing current at a high current range(Fig. 32). Dilution increased at low currents because the rise in the current is higher than the rise in the electrode feed rate (welding speed)(Eq. 8). Thus the rate of heat generation out-paced the rate at which heat was removed through the surrounding metal. For a high current, the effect was just the opposite.

The current increased as electrode feed rate increased. The current was approximately proportional to the square root of the electrode feed rate. The current was also dependent on the welding voltage even if the voltage dependence was not strong. The current was approximately proportional to the cube root of the welding voltage. Fig. 33 illustrates these relationship.

The increase of current with increased electrode feed rate was probably because the increase of electrode feed rate reduced the gap between electrode tip and molten metal pool surface thus decreasing the effective resistance of the current path. Current increased with an increase of voltage. The increase of voltage increased the molten slag temperature inducing an increase in effective current conducitivity and a resultant increase in current(Eq. 9)(Fig. 12). Too high a voltage will reduce the molten slag temperature because of heat losses due to exposed arcing or radiation. This increases the resistivity of the molten slag

and thereby reduces the current.

The effect of guide plate geometry(Fig. 14) on uniformity of penetration was also studied as a function of voltage variation at fixed current. Wing, web and standard guide tubes/plates were compared in 50 mm thick plate. Only wing and web guide plates when compared in 76 mm thick plate. The 50 mm thick plate with web guide plate showed the most uniform penetration when compared to wing guide plate or standard guide tube with electrode oscillation. However, welds deposited between 50 mm thick plates with a wing guide plate exhibited greatly increased uniform welding penetration, compared to the standard guide tube. The use of the web guide plate resulted in welds having better uniformity of penetration in the 76 mm thickness than did the wing guide method. This was due to the efficient distribution of heat towards the plate edge. However, web guide plate consistently produced greater BMD than the wing guide as shown in Figs. 31 and 32. This was probably due to the production of a high form factor and greater penetration at plate sides in web guide weld.

Form factor was a useful parameter for describing the geometry of the liquid pool and susceptibility to hot crack formation. The relative orientation of the grains, and therefore the encounter angle, could be related to the form factor. Smaller form factor (higher encounter angle) produced greater center line impurity segregation and, as a consequence, a higher susceptibility to center line hot cracking. Form factor increased with increasing voltage at constant current (Fig. 34) and was inversely related to the current at a constant voltage (Fig. 35).

For ESW 50 mm and 76 mm thick plates, the dual electrode web guide technique had a higher form factor (Fig. 35) and thus

greater resistance to hot cracking than the single electrode wing guide. The majority of current and heat transfers from the tip of the electrode to the bottom of the pool. Therefore a high current and a high heat were concentrated at the tip of the one centrally located electrode wing guide plate. This induced a deeper weld pool. The current density was reduced in the web guide plate electrodes as it was split between two electrodes which were at the guide plate edges(Fig. 36).

In the standard weld, in Fig. 37, the current could not exceed 800A because of guide tube overheating and hot crack formation in the weld. The narrow gap welds, however, could survive up to around 1250A or 1400A without introducing any hot crack formation in the weld. Figure 36 clearly illustrates the improvement in hot cracking resistance for the narrow gap welds, especially in the web guide plate weld. No wing or web guide plates were studied in standard gap (32 mm) electroslag welding.

The reasons for the change in hot cracking resistance could be deduced by referring to Fig. 36. If the same current and voltage were applied in both standard weld and narrow gap welds, the following weld characteristics result(Fig. 36). In standard welds fabricated with a single cylindrical guide, the heat and current density are concentrated at a point and the electrode penetrated deeply into the slag pool to maintain an Ohm's law, thus inducing a low form factor. In narrow gap welds fabricated with plate guides, the current and heat density were distributed across the weld joint more uniformly via the guide plates, thus inducing a higher form factor and shallower weld pool. This effect was greatest with the dual electrode web guide plate, because heat was distributed more efficiently to the plate surfaces, resulting in less current density.

Since the solidification front followed the steepest temperature gradient, impurities segregated at the weld center in the standard weld. However, the impurities were more evenly distributed along the weld centerline in the narrow gap welds due to the elongated, shallow temperature gradient induced by the wing or web guide plates.

In ESW, the weld surface is in compression while the weld center experiences triaxial tension as it solidifies last. Narrow gap, high current ESW exhibits lower stresses due to a smaller weld pool. This led to less shrinkage stresses, better form factor, and lower hot cracking susceptibility.

The effect of heat input on total HAZ size was also studied. From this study, total HAZ size at the maximum penetration region was observed to be relatively independent of heat input in narrow gap welds. Local heat generation and distribution patterns appeared to be more critical because maximum temperature gradient or heat flow direction was significantly affected by molten pool shape. Factors affecting local heat generation and distribution patterns included electrode extension into the slag pool, pool shape, and electrode positioning and straightening.

2. Characteristic Grain Structures

Narrow gap ESW of A36 and A588 steels using mild steel electrodes (25P and WS) results in Type II structures. The macrostructure characteristics for Type II welds were categorized in Fig. 22. High toughness is associated with fine grained acicular ferrite. For this reason, it has become increasingly important to understand the factors which would maximize the volume fraction of acicular ferrite in the weld

metal.

The coarse columnar grain (CCG) zone in the Type II structure contained abundant acicular ferrite ($\sim$ 90%). On the other hand, the thin columnar grain (TCG) zone and weld center showed low acicular ferrite but increased proeutectiod and widmanstatten ferrite at prior austenite grain boundaries(Fig. 25). Thus attempts were made to obtain the largest CCG zone without introducing any hot cracking in the weld.

The extent of the CCG zone decreased with increasing voltage at constant current(Fig. 38) and increased with increasing current at constant voltage(Fig. 39). The narrow gap welds exhibited a greater extent of the CCG zone in the weld than standard welds. This was promoted by the higher current and higher welding speed in narrow gap weld. From Fig. 36, the single electrode wing guide plate exhibited a slightly more favorable macrostructure for toughness than the dual electrode web guide plate. Generally, the best macrostructure for high toughness was often accompanied with low form factor, which led to poor resistance to hot cracking.

The proportion of specific grain structures found in a given Type weld varied as a function of welding parameters. These structure changes observed for Type II narrow gap ESW can be broken down into three cases, as illustrated in Fig. 40.

a) Case I - The weld metal macrostructure consisted of a small outer zone of CCG and a large interior zone of elongated TCG. The center line of the weld contained grains running vertically, or parallel to the direction of heat source. The structure was obtained with low weld current (600-800 A), high voltage (42-47 V) and slow welding speeds (0.25

- 0.30 mm/sec.). The electrode extension into the slag pool was small and heat input was high, producing great base metal penetration. Thus, the weld pool shape was shallow and wide (Form factor : >2.0).

The dendritic structures at the weld center possessed the lowest susceptibility of center line hot cracking because dendrites could not impinge upon the weld center line to form a "plane of weakness". So interdendritic impurities were dissipated uniformly through out the weld zone. The nearly circular weld pool and slow welding speeds tended to allow the growing austenite columnar grains to follow the heat source by curving in behind the moving heat source. The microstructure contained large amounts of grain boundary ferrite and widmanstatten ferrite due to the slow cooling rate. Thus the impact toughness tended to be low because the crack propagated along the direction of grain boundary ferrite[4, 5].

b) Case II - The weld metal macrostructure consisted of around 50% CCG zone and 50% TCG zone. The central part of the weld structure pattern consisted of rows of thin columnar grains impinging gradually at the center line. This structure was obtained by increasing both welding current (800 - 1100 A) and welding speed (0.35 - 0.60 mm/sec.) The electrode extension into the slag pool was optimum (Form factor : 1.2 - 2.0) for best microstructure and toughness without hot cracking. This structure also showed low susceptibility to center line hot cracking due to dissipation of impurities throughout the weld. In addition, the microstructure was favorable for good toughness because it contained less proeutectoid ferrite and more acicular ferrite than the Case I welds.

c) Case III - The weld metal macrostructure consisted of a large outer

zone of CCG and small interior zone of TCG. In these welds, grains and dendrites grew directly to the weld center line and impinged abruptly giving rise to a "herring bone" appearence. The structure was obtained for welding conditions with higher current(1100 - 1300A) and welding speed(0.6 - 0.75 mm/sec.) than Case II. The electrode extention into the slag pool was large, thus the weld pool shape was narrow and deep(Form factor : 0.9 - 1.2). Although these welds contained a high percentage of acicular ferrite, the grain structure at the weld center line was susceptible to hot cracking because impurities were segregated to the center line. The higher the obtuse encounter angle, the greater the susceptibility to center line hot cracking.

In addition, when the highest values of current (1300 - 1550A) and weldng speed (>0.75 mm/sec.) were applied, the electrode extension into the slag pool was a maximum. This produced a narrow and extremely deep weld pool (Form factor : <0.9) and Type IV structure, seen in Fig. 22 and described earlier.

Fig. 41 summarizes volume percent of coarse columnar, thin columnar and equiaxed zones in the weld metal as a function of welding speed at constant 40V. Fig. 42 also represents the encounter angle and the range of hot cracking and equiaxed grain formation as a function of welding speed at constant 40V.

4. Optimum Conditions

Based on all parametric studies, macrostructure and especially microstructure analysis (Fig. 40), the optimum conditions for sound narrow gap, unalloyed ESW (Case II welds) were summarized in Table 5. Typical microstructures at the weld center and HAZ 1 of optimized welds

of A36 and A588 plates are shown in Fig. 43. Wing guide plate was preferred in 50 mm thick plates. But the web guide plate was recommended for ESW 76 mm thick plates because of uniform side wall penetration.

The technical data comparison (Table 6) between standard and optimized narrow gap ESW taken from 50 mm thick plate pointed out the great reduction in heat input that was achieved by utilizing the optimized narrow gap ESW procedure. Welding efficiency and welding speed were also greatly improved. The optimized narrow gap ESW showed slightly higher BMD. But the base metal penetration was greatly reduced due to more uniform side wall penetration. The HAZ was reduced in the optimized narrow gap ESW process compared to standard weld. Fig. 44 schematically compares the base metal penetration, dilution and HAZ size between standard and optimized narrow gap ESW.

The encroachment of the slag pool into the base metal in the standard weld produced a pendulant overhang where the slag would be easily entrapped when abrupt voltage and current change occurred during welding. The encroachment of the slag pool into the base metal was smaller and more uniform in the optimized narrow gap welds. Thus pendulant overhang and slag entrapment were not problems in narrow gap ESW.

E. Quartz Grain Refinement

In addition to the above weld metal alloy and process modification, quartz grain refinement through dynamic stimulation in large ES welds was also tried. This was because substantial grain refinement in the weld fusion zone can play an important role in preventing severe hot cracking while enhancing weld metal fracture toughness without the need for expensive alloyed filler metals.

1. Welding Parameter Study

The quartz sleeve effectively shielded the guide tube from the molten slag and resulted in deep extension of the quartz and guide tube into the slag pool (Fig. 45). Current and voltage fluctuations occurred right after the quartz sleeve was immersed in the slag pool. Persistent arcing, current and voltage fluctuations, and intense stirring of molten pool continued throughout the ES weld process(Fig. 46).

A decrease in the effective conductivity (and increasing viscosity) of the slag by quartz dissolution decreased both the generation and local transport of the Ohmic heat (Fig. 47). A decrease in the effective conductivity of the slag further promoted deep extension of the electrode into the slag pool to maintain Ohm's law, which was further accelerated by confinement of heat by quartz tube. All of these effects resulted in an increase in the local temperature only near the electrode and, consequently, caused an increase in the electrode melting rate. Due to confinement of heat by quartz tube and decreased transport of heat to the base metal sides, local heat generation patterns were extremely sensitive to electrode location and wire straightening. Even minor misalignment of the electrode resulted in a markedly asymmetrical heat generation

pattern. The use of electrode oscillation provided more uniform heat generation patterns (Fig. 48).

The narrow gap (19 mm) technique using a web guide plate shrouded with quartz was tried in the hope of achieving fast welding speed and turbulent stirring of molten pool. The technique, however, was not successful. Narrow gap spacing didn't allow room for slag bath formation along with the quartz around the guide plate. The slag was forced up the spacing along the guide and weld plates and frozen there.

Standard gap (32 mm) techniques using web guide plate shrouded with quartz were also tried. But problems still existed because of high silica content and extreme flux turbulence. Narrow gap (19 mm) quartz shrouded guide tube and powder cored tubular electrode (PS 588) was also performed in the hope of less extension of electrode into the slag pool. Deep extension was detrimental, because deep electrode extension into the slag pool induced kite-shaped molten pool and heat concentration in the vicinity of electrode tip. This work was also not successful as consistent lack of fusion occurred. Slow welding speed was required to modify the heat generation and distribution pattern.

When a single standard quartz shrouded guide tube was used in ESW 50 mm thick plates, non-linear relationship between BMD and voltage was observed at constant current (Fig. 49). In order to generate sufficient heat to melt the base metal, the thermal shielding behavior of the quartz shroud resulted in the need to apply a higher voltage (around 48V) than that used in welds without quartz shielding.

Welding voltage above 48V led to severe arcing. This was because the jet stream of superheated/vaporized slag generated by Joule heating in extremely high voltage at the electrode tip area was sufficient to

blow the slag out and locally boil the slag. This introduced a gas envelope and severe arcing. Form factor was not greatly influenced by either the welding voltage or current (Fig. 50). Ironically, the conditions necessary to produce sound, tough welds by the standard ESW process were the worst conditions for quartz shielded guide grain refined ESW.

The effect of mechanical oscillation of the shrouded guide on the grain refinement was investigated on 76 mm thick plate. Different oscillation speeds (8 seconds, 5 seconds and 3 seconds) with or without dwell time(1 second) were tried. Grain refinement across the entire weld section resulted in every weld metal. Lack of fusion still existed. Quartz shielded dual electrode (50 mm spacing) ESW with or without oscillation was also tried on 76 mm thick plate. Grain refinement resulted. But lack of fusion still existed.

An increase of silica content due to melting of the quartz shroud reduced the basicity of slag. This caused a large increase of the silicon and oxygen concentrations in the deposited metal (Fig. 51)(Table 4). Weld metal carbon content was found to be substantially decreased with increasing weld metal oxygen content because of the degassing of carbon monoxide formed during vigorous agitation(Table 4). Therefore, the weld metal carbon equivalent was decreased with increasing oxygen content. Table 7 illustrates the chemistries of major elements of PF201 flux and slag before and after quartz shroud dissolution.

The high conductivity slag (CaF_2 - CaO - Al_2O_3) was used to increase the thermal efficiency in an effort to solve the lack of fusion problem. High electrically conducting slags are formed by addition of CaF_2. Their use considerably facilitated the starting and the stabilizing of the

shrouded consumable guide tube produced a substantial grain refinement (Fig. 53). Microstructural analysis of the quartz grain refined welds revealed significantly increased nucleation of polygonal, grain-boundary and widmanstatten ferrite due to an excessive oxygen potential induced in the manganese silicate fluxes by quartz dissolution. The high oxygen potential also led to many inclusions (Fig. 23) interdendritically and at the austenite boundaries, which helped to nucleate ferrite early in the austenite-ferrite transformation. By increasing the oxygen in the weld [illegible] dissolution, the amount of acicular ferrite was

blow the slag out and locally boil the slag. This introduced a gas envelope and severe arcing. Form factor was not greatly influenced by either the welding voltage or current (Fig. 50). Ironically, the conditions necessary to produce sound, tough welds by the standard ESW process were the worst conditions for quartz shielded guide grain refined ESW.

The effect of mechanical oscillation of the shrouded guide on the grain refinement was investigated on 76 mm thick plate. Different oscillation speeds (8 seconds, 5 seconds and 3 seconds) with or without dwell time(1 second) were tried. Grain refinement across the entire weld section resulted in every weld metal. Lack of fusion still existed. Quartz shielded dual electrode (50 mm spacing) ESW with or without oscillation was also tried on 76 mm thick plate. Grain refinement resulted. But lack of fusion still existed.

An increase of silica content due to melting of the quartz shroud reduced the basicity of slag. This caused a large increase of the silicon and oxygen concentrations in the deposited metal (Fig. 51)(Table 4). Weld metal carbon content was found to be substantially decreased with increasing weld metal oxygen content because of the degassing of carbon monoxide formed during vigorous agitation(Table 4). Therefore, the weld metal carbon equivalent was decreased with increasing oxygen content. Table 7 illustrates the chemistries of major elements of PF201 flux and slag before and after quartz shroud dissolution.

The high conductivity slag (CaF_2 - CaO - Al_2O_3) was used to increase the thermal efficiency in an effort to solve the lack of fusion problem. High electrically conducting slags are formed by addition of CaF_2. Their use considerably facilitated the starting and the stabilizing of the

A typical macrostructure of weldments made using the quartz shrouded consumable guide tube is shown in Fig. 46. The use of fused quartz shrouded consumable guide tube produced a substantial grain refinement (Fig. 53). Microstructural analysis of the quartz grain refined welds revealed significantly increased nucleation of polygonal, grain-boundary and widmanstatten ferrite due to an excessive oxygen potential induced in the manganese silicate fluxes by quartz dissolution. The high oxygen potential also led to many inclusions (Fig. 23) interdendritically and at the austenite boundaries which helped

blow the slag out and locally boil the slag. This introduced a gas envelope and severe arcing. Form factor was not greatly influenced by either the welding voltage or current (Fig. 50). Ironically, the conditions necessary to produce sound, tough welds by the standard ESW process were the worst conditions for quartz shielded guide grain refined ESW.

The effect of mechanical oscillation of the shrouded guide on the grain refinement was investigated on 76 mm thick plate. Different oscillation speeds (8 seconds, 5 seconds and 3 seconds) with or without dwell time(1 second) were tried. Grain refinement across the entire weld section resulted in every weld metal. Lack of fusion still existed. Quartz shielded dual electrode (50 mm spacing) ESW with or without oscillation was also tried on 76 mm thick plate. Grain refinement resulted. But lack of fusion still existed.

An increase of silica content due to melting of the quartz shroud reduced the basicity of slag. This caused a large increase of the silicon and oxygen concentrations in the deposited metal (Fig. 51)(Table 4). Weld metal carbon content was found to be substantially decreased with increasing weld metal oxygen content because of the degassing of carbon monoxide formed during vigorous agitation(Table 4). Therefore, the weld metal carbon equivalent was decreased with increasing oxygen content. Table 7 illustrates the chemistries of major elements of PF201 flux and slag before and after quartz shroud dissolution.

The high conductivity slag (CaF_2 - CaO - Al_2O_3) was used to increase the thermal efficiency in an effort to solve the lack of fusion problem. High electrically conducting slags are formed by addition of CaF_2. Their use considerably facilitated the starting and the stabilizing of the

quartz-shrouded ESW process. Increasing slag conductivity increased the melting efficiency (Fig. 52) giving melt-back of the quartz shroud. Penetration of the quartz shielded guide tube into the slag pool was greatly reduced. This eliminated the intense stirring and grain refinement present in previous quartz shroud welds. Thus, the conductivity of slag was very important in quartz-shroud induced grain refinement. A flux exhibiting less than 2/(Ωcm) at 1700°C was required for substantial grain refinement.

2. Metallurgical Structures

A typical macrostructure of weldments made using the quartz shrouded consumable guide tube is shown in Fig. 46. The use of fused quartz shrouded consumable guide tube produced a substantial grain refinement (Fig. 53). Microstructural analysis of the quartz grain refined welds revealed significantly increased nucleation of polygonal, grain-boundary and widmanstatten ferrite due to an excessive oxygen potential induced in the manganese silicate fluxes by quartz dissolution. The high oxygen potential also led to many inclusions (Fig. 23) interdendritically and at the austenite boundaries, which helped to nucleate ferrite early in the austenite-ferrite transformation. By increasing the oxygen in the weld metal through quartz dissolution, the amount of acicular ferrite was decreased. With further increase of weld metal oxygen up to 800ppm, the amount of acicular ferrite approached zero (Figs. 23 and 27).

The advantages of the refined grains and lowered carbon equivalent were offset by increased proeutectoid ferrite. The amount of acicular ferrite was significantly increased (~75%) by alloy modifications (AX90 : high Ni electrode), which also induced refined grain boundary ferrite.

Composition control through the introduction of low alloyed filler metal was necessary in order to maximize the volume fraction of acicular ferrite.

Quartz shrouded welds were fabricated using basic fluxes in an attempt to control flux oxygen potential. Basic fluxes have low reactivity due to the high thermodynamic stability of the compounds which make up the flux. This minimizes oxygen pick up and promoted deoxidation of the weld metal. When the weld metal oxygen level reached below around 550ppm, coarse columnar grains started to develop and 100% coarse columnar grains were generated below 100ppm of oxygen (Type III of Fig. 22). Thus, the basicity of slag (oxygen potential) was very important for development of quartz-shroud induced grain refinement.

F. Mechanical Properties

The impact requirements for A36 and A588 plates are 20 Joules at 4°C according to the zone 2 requirement of American Association of State Highway and Transportation Officials (AASHTO)[115]. All base metals used in this study successfully qualified according to AASHTO zone 2 requirement (Table 8). AWS D1.1 does not require base plates toughness but does require weld toughness[116]. The AWS D1.1 impact requirements for ES welds are 20 Joules at -18°C for the quarter thickness location on the weld center line[120].

The variations of CVN toughness at -18°C with respect to each structure type (Fig. 22) and test specimen location are compared in Fig. 54, which illustrates the upper and lower impact energy limit. Type I structures exhibited low impact energy due to the large amount of oxygen inclusions, blocky and grain boundary ferrite. In Type II, wide variations of fracture toughness values were experienced between conventional welds using standard practices and welds using process modifications (narrow gap, fast weld speed, etc.) that decrease heat input. A substantial increase in Charpy toughness in A36 welds was observed in the weld center region of the narrow gap (19 mm) with wing or web guide welds when compared to the standard welds (Table 8). Welds deposited on A588 developed slightly lower toughness than similar A36 welds (Table 8), despite the large amount of acicular ferrite in the A588 welds. This was because the A588 weld metal had a microstructure containing greater amounts of pearlite(Fig. 43) and a higher hardness (A588 : 94 Rb, A36 : 84 Rb).

Type III welds averaged 37 Joules at weld center in A36 welds(Fig.

54). These welds provided less preferential crack initiation sites during impact testing due to less oxygen inclusions, a high volume fraction of blocky and coarse acicular ferrite and less grain boundary ferrite. The number and size distribution of inclusions played an important role in influencing weld metal microstructure and toughness. Type IV structures showed extremely nonuniform properties throughout the weld. The low toughness value of the thin columnar grain region was believed to be associated with microcracks developed interdendritically. This was induced by high solute accumulation interdendritically. Type V structures exhibited substantially increased fracture toughness. This was due to uniform distribution of impurities by development of equiaxed dendrites and also fine acicular ferrite formation throughout the weld. An important achievement in Types I, III and V structures was the uniformity of CVN impact toughness. This was consistent with a uniform distribution of impurities due to earlier development of columnar and equiaxed dendrites and uniform grain structures throughout the weldment.

The variations of CVN toughness at -18°C, with respect to each case (Fig. 40) and test specimen location in A36 welds of narrow gap ESW, are compared in Fig. 55. This figure illustrates upper and lower impact energy limits. Case I structures exhibited low impact energy at weld center because dendrites, interdendritically segregated impurities and grain boundary ferrites were running parallel to the direction of notch crack propagation path (Fig. 40). The low toughness at weld center of Case III was believed to be associated with high solute accumulation interdendritically and microcracks developed interdendritically. All data from optimized narrow gap ESW (Case II welds) successfully met the recommended AWS criterion, even at midthickness.

The quartz grain refined welds exhibited almost identical toughness values throughout the weld, which was consistent with a uniform fine grain structure in entire fusion zone. Average mid-thickness CVN impact toughness values tested at -18°C for various structural zones of quartz grain refined A36 and A588 ES welds are given in Fig. 56. A great CVN toughness increase was observed in the weld center region of the grain refined A588 weld when compared to the standard weld. In A36 welds the quartz grain refined welds at weld center region showed a slight decrease of impact energy compared to standard welds. This was obviously due to the increased blocky and grain boundary ferrite and high inclusion contents in quartz welds.

Complete Charpy temperature transition curves for selected unalloyed, optimized welds and standard welds, together with base metal, are shown in Figs. 57 through 62. The 20 Joules transition temperature is tabulated in Table 9. The optimized narrow gap welds increased fracture toughness and lowered the ductile/brittle transition temperature of the weld metal as shown in Figs. 58 through 62 and Table 9. The high oxygen (quartz grain refined welds with alloy addition) welds exhibited somewhat lower toughness than medium oxygen welds (Figs. 54 and 62).

V. DISCUSSION

A. Dendrite Reorientation and Renucleation during Weld Metal Solidification

1. Solute Banding

Solute banding in welds is caused by the non-uniformity of mixing in the molten pool and is very common in fusion welds because of the periodicity of the growth rate. There is a critical growth rate below which the solutes are pushed by the interface and above which they are enriched in the solid[32-33].

Solute banding contributes substantially to dendrite reorientation and renucleation. Dendrites can change growth direction by one or a combination of following mechanisms :
(a) dendrite arm bending (b) partial and complete dendrite arm remelting (c) new renucleation of dendrites and (d) dendrite curving. In addition, (e) development of tertiary dendrite arms also contributes to dendrite reorientation when solute enrichment band is absent or weak. Dendrite bending is defined that dendrite grows straight following preferred growth direction and changes growth direction in another preferred growth diretion by kink motion. Curved dendrite is a hook-shaped dendrite which is caused by continuous change of growth direction of dendrite. Fig. 63 is a schematic sketch illustrating several dendrite characteristics observed in the solute bands.

2. Dendrite Bending

When partially solidified metallic dendrites are subjected to a shear stress induced by liquid flow at its solidus temperature, the soft metallic dendrite arms may deform plastically in the direction of the

maximum temperature gradient. Since the growth rate and thermal gradient in welds are orders of magnitude greater than those of ingots[18], dendrite bending is undoubtedly operative in welding. The nature of the pulse type stress exerted on the partially solidified dendrites intensifies the dendrite bending, especially at solute bands, because solute bands are formed by pulse type movement of solidification front.

If the bending angle, which is defined in Fig. 64(top), is greater than 20°, the dendrites are completely broken and totally wet by the liquid according to the surface-energy controlled grain boundary wetting concept[28]. Even when the dendrites are misoriented from the original dendrite growth direction by an angle greater than about 20°, the surface energy of the boundary (γ_{gb}) becomes unstable according to :

$$\gamma_{gb} > 2\gamma_{S-L} \qquad (19)$$

where γ_{S-L} is the surface energy of the solid-liquid interface. The grain boundary is replaced by a thin layer of liquid and the dendrites can break apart along the prior boundary as reported by Doherty et al.[28].

In ESW of mild steel, a crude estimation of the region of constitutional supercooling (x) was given by the Eq. 20 [117]. Calculations considering Mn as the major alloying element showed that the weld center region was around 40 times larger than the fusion line region.

$$\Delta T = T_L - T_A = m_L C_o \frac{1 - k}{k} \left[1 - \exp\left(-\frac{R\,x}{D_L}\right)\right] - G\,x = 0 \qquad (20)$$

where T_L, and T_A are equilibrium liquidus temperature corresponding to different points ahead of the solid-liquid interface and actual

temperature in the liquid, respectively and values used for calculations were as follows ; m_L = 5.0, Co = 1.2, k = 0.74, $D_L = 5 \times 10^{-3}$ mm^2 /sec, R = 0.025 - 0.05 mm/sec (near fusion line), R = 0.3 - 0.58 mm/sec (weld center) and G = 120 - 160° C/mm (near fusion line), G = 3.3 - 3.5° C/mm (weld center) . Thus, the dendrites will tend to project into the liquid substantially longer distances at weld center region than at fusion line region. The further the dendrites project into the liquid, the easier the partially solidified dendrites will be bent or broken by liquid flow.

3. Partial and Complete Dendrite Arm Remelting

The localised thermal fluctuations around the growing dendrites, caused by the effect of disturbances in growth rate (identified by the presence of solute bands), is to produce conditions conducive to dendrite arm remelting. In this regard, solute-enriched bands alter dendrite morphology because remelting at the roots of dendrite arms is induced by local solute accumulation, which drops the local equilibrium liquidus temperature. If the degree is severe, complete remelting of dendrite arms may be occur. Fluid flow by convection and pulse-type thermal stress will also result in dendrite arm remelting. Once the dendrite arm fragments are loose, they are able to grow in a more favorable direction.

4. Dendrite Renucleation

Three factors promoting renucleation are (a) substantial undercooling (b) nucleating substrates like innoculant and solid inclusions and (c) dynamic nucleation (dendrite multiplication). The nucleation rate (I) was assumed to be of the form[96].

$$I = Io\ (No - N)\ \exp\ [\ -\ \frac{u}{(\Delta T)^2}\ ] \qquad (21)$$

where No is the total number of heterogeneous substrate particles, N is the number that have already nucleated, ΔT is the undercooling and Io and u are constants. If the nucleants are carried into the supercooled liquid and survive, new dendrites grow with their <100> directions parallel to the temperature gradient. Oxide inclusions could be transported by liquid convection through the weld pool and segregation of oxide inclusions would be maximum in the solute enriched band because of fast movement of solidification front.

Ohashi et al.[95] studied the effect of oxides on nucleation behavior and showed that the degree of critical undercooling in the case of rare-earth metals (La, Ce, Pr and Nd) addition was 3°C, while that for Al203 was 14°C, for Si02 was 30°C, and for MnO was 53°C. In ESW, the rough estimation of maximum undercooling calculated from Eq. 22 given by Davies[117] considering Mn as a major alloying element was around 20-40°C near fusion line and 1-2° C at the weld center region.

$$\Delta T_{max} = \frac{m_L Co(1 - k)}{k} - \frac{GD_L}{R}\ [1 + 1n\ \frac{m_L C_o(1 - k)R}{GD_L k}] \qquad (22)$$

Thus, oxide particles (mostly, Si02, MnO, Al203 or combination of these) in welds can promote nucleation of dendrites. The solute enriched band is suitable for the nucleation of new dendrites because it accentuates local constitutional supercooling and contains copious amounts of oxide segregation. All the oxide particles which survived in the supercooled liquid region will grow following the preferrential growth direction. These large number of crystals will give a fine dendrite arm spacing

after growing through the solute enrichment band (Fig. 18) because of copious heterogeneous nucleation by localised constitutional supercooling.

5. Dendrite Curving

The observation of dendrite curving in a solute depletion band in GTAW was particularly interesting because it is generally believed that dendrites grow straight following <100> direction. Several investigators[50, 118-120] studied the effect of fluid flow on the deflection of growth direction and found that if the bulk liquid flows in the process of dendritic growth, the dendrite is deflected against the direction of fluid flow due to disruption of the radial diffusion fields around the dendrite tips (Fig. 72, Bottom). Doherty et al[28] reported that the dendrites grow toward the flow direction by liquid flow.

The dendrite curving observed in GTAW was directed toward the heat source. The influence of the liquid flow direction on the growth direction could not be related in this study. However the vortical liquid flow induced by severe arc torch weaving in GTAW -together with the maximum temperature gradient- was believed to continuously stress the dendrite during growth to produce curving. Dendrite curving was not found in electroslag welds due to low temperature gradient and low fluid flow as compared to GTAW.

6. Development of Tertiary Dendrite Arms

Tertiary dendrite arms developed when the growth direction of the primary dendrite arms differed substantially from the maximum temperature gradient vector and forced liquid flow was absent or weak. As a result, tertiary arm development always occurred near the weld center. The

primary dendrites growing with a large deviation from the maximum temperature gradient vector diminish and secondary and tertiary dendrite arms develop. From Fig. 20, the deviation angle between maximum temperature gradient vector and dendrite growth direction is believed to be around 45°.

7. Effect of Alloy and Oxygen Content

Alloy and oxygen contents will also significantly affect the amount of solute bands and dendrite rearrangements. Higher alloying accelerates the degree of constitutional supercooling and results in earlier development of columnar or even equiaxed dendrites.

Oxygen content(ie. oxide particles) also promotes equiaxed dendrites by nucleation. The size of the equiaxed zone in alloy/oxygen welds affects the solute bands. The smaller the equiaxed dendrite zone, the larger the solute bands, because once equiaxed dendrites develop, uniform distribution of solutes develops and solute bands cease to form.

The dense spacing of transverse solute bands near the fusion line region was probably due to the hydrodynamic effect in the molten pool in addition to molten base metal penetration. Pulse motion of liquid flow is expected to be maximum at the molten pool edges because of shallow pool depth. In addition, strong convection would also be intense at the weld edges due to a high thermal gradient[121].

Microstructural characteristics of the weld metal were dependent upon solidification induced compositional variations. In mild steel ES welds, the white-etching band contains comparatively high segregation of impurities. Polygonal ferrite easily nucleated at these preferred sites with a small undercooling below the A3 temperature. Similary, in Ni-Mo

alloyed welds the white band also had high segregation of solutes such as Ni. The presence of Ni in the white band shifts the austenite decomposition curve or CCT diagram downward and to the right and suppresses the ferritic transformation temperature. Acicular ferrite formed in the solute rich bands, while polygonal ferrite nucleated in the Ni-depleted regions associated with the dark etching bands.

B. Effect of Welding Parameters on Solidification Structure and Microstructures

The solidification of low alloy steel weld deposits involves the epitaxial growth of delta-ferrite from the plate grains at the fusion boundaries[122]. The liquid metal ahead of a solidifying interface is constitutionally supercooled and the interface is unstable. Thus dendrites break down into one of the several dendritic growth modes. The resulting solid delta-ferrites have an anisotropic columnar morphology with their major axes following the direction of maximum heat flow. On further cooling, austenite allotriomorphs nucleate at the delta-ferrite boundaries. Anisotropic austenite growth along delta ferrite boundaries leads to the formation of columnar austenite grains which closely resemble the original delta ferrite morphology[123, 124]. During the austenite to ferrite transformation, a large variety of microstructures develop. The final weld metal microstructures depend on complex interactions between several important variables such as the weld thermal cycle, the solidification structure, the prior austenite grain size, the total alloy content and concentration, chemical composition, and size and distribution of non-metallic inclusions[108].

In normal ES welds (including commercial welding practice), relationship between weld metal solidification structure and subsequent solid state macro/microstructure has been established (Fig. 65)[125] based on fundamental solidification and solid state transformation mechanics [108, 122, 123, 124]. Solidification in the cellular-dendritic mode resulted in coarse columnar austenite grains which transformed to predominantly acicular ferrite. Columnar dendritic solidification produced thin columnar austenite grains which transformed to mostly grain

boundary and widmanstatten ferrite. Thus, if the solidification structures are predicted, the macro/microstructures can also be predicted in normal ES welds.

1. Welding Variables

Voltage, current, and welding speed are closely related to heat input (Eq. 7). The solidification structures are determined by $G/R^{\frac{1}{2}}$ and Co (Fig. 5). The temperature gradient was reported to be inversely proportional to the cube root of heat input[121].

$$G = f\left(\frac{1}{H^{1/3}}\right) \tag{23}$$

More specifically, the temperature gradient was a function of melting point (Tm) divided by the distance between the heat source and the weld pool boundary (x)[126].

$$G = f\left(\frac{Tm}{x}\right) \tag{24}$$

Thus, from the Eq. 4 and 24,

$$G/R^{\frac{1}{2}} = f\left(\frac{Tm}{x(VwCos\theta)^{\frac{1}{2}}}\right) \tag{25}$$

$G/R^{\frac{1}{2}}$ is influenced by the weld pool shape and welding speed and is different at all points of the pool boundary, because weld pool shape and welding speed respectively determine the x and Vw terms of Eq. 25.

In the nearly spherical weld pool, slow welding speed and high heat input weld (Case I shown in Fig. 40), the range of $G/R^{\frac{1}{2}}$ from fusion line to weld center is small because the distance between the heat source and the weld pool boundary (x) is almost identical from fusion line to weld center. The value of $G/R^{\frac{1}{2}}$ at the fusion line is also small,

compared to the high speed, kite shaped weld pool because the x value of Eq. 25 at the fusion line is higher in the nearly spherical weld pool than in the kite-shaped weld pool (Fig. 40). The small range of $G/R^{\frac{1}{2}}$ from fusion line to weld center and small $G/R^{\frac{1}{2}}$ value at the fusion line developed in the nearly spherical weld pool induce a small exterior cellular dendritic structures and a large interior columnar dendritic structures (Case I of Fig. 66), when superimposed on the diagram of solute content and solidification parameter diagram (Fig. 5).

Columnar dendrites reject more solutes to the interdendritic region than to the dendritic tip. Thus, the solute distribution in the solidifying front is thought to be constantly increased because of earlier development of columnar dendrites and frequent change of dendrite orientation to follow the maximum temperature gradient (Case I of Fig. 66). Thereby, the weld metal macrostructures consisted of a small outer zone of coarse columnar grains (in the region of cellular dendrite) and a large interior zone of thin elongated columanar grains (in columnar dendritic region). The microstructure contained large amounts of grain boundary and widmanstatten ferrite due to the slow cooling rate and high proportion of columnar dendrites in the fusion zone.

However, in the kite shaped weld pool (high welding speed and low heat input weld : Case III of Fig. 40), $G/R^{\frac{1}{2}}$ values at fusion line and weld center are larger and smaller, respectively, compared to the nearly spherical weld. A larger range of $G/R^{\frac{1}{2}}$ is generated from fusion line to weld center. Thus, the outer large range of cellular dendrites and interior small zone of columnar dendrites appeared in the weld metal(Case III of Fig. 66). The weld metal macrostructures consisted of a large outer zone of coarse columnar grains (predominantly consisting of

acicular ferrite in the region of cellular dendrites) and a small interior zone of thin columnar grains (mostly consisting of a high volume fraction of grain boundary and widmanstatten ferrite in the columnar dendrite region). These conditions are responsible for hot crack formation due to high solute accumulation at the weld center region.

In the fastest welding speed and the lowest heat input welds (with extremely deep molten pool and lowest form factor welds : Type IV weld of Fig. 22), the fast cooling rate allows less time for lateral diffusion of the rejected solutes giving finer dendrite arm spacing and less segregation. This acceralates more solute accumulation to the weld center region. The development of a large zone of cellular dendrites further helps the solute rejection to the weld center. The transition from columnar to equiaxed dendrites (Type IV of Fig. 22) is associated with fast growth rate, high amount of solute content and low thermal gradient at the weld center (Type IV of Fig. 66). The high degree of constitutional supercooling provided the driving force for dendrite arm remelting resulting in nucleation of equiaxed dendrites at the weld center.

The observation of pearlite islands in A588 and widmanstatten ferrite in A36 steel welds along the grain boundary ferrite provided good contrast in mild steel ES welds and HAZ 1(Fig. 43). Since the ferrite is very low in carbon (less than 0.02 wt.%C at A1 temperature), its growth is associated with a rejection of carbon from the ferrite-austenite interface back into the austenite. When the undercooling below AC3 is large due to thermal supercooling by local heat extraction, carbon diffusion needed for carbon removal from the interface is not efficient, forming a steep carbon gradient. The only way to break the

carbon solute barrier is the formation of separate ferrite needles, which is widmanstatten ferrite. So once grain boundary ferrite is formed from the austenite grain boundaries, further growth of widmanstatten ferrite normally occurred in A36 welds.

When strong carbide forming elements, such as Cr, are added to A588 welds, carbon concentration at the interface is large and the austenite is unstable with respect to both ferrite and cementite so that Fe3C precipitation occurs. Ferrite will continue to grow until a carbon barrier is again formed which introduces pearlitic structures along the grain boundaries[8].

2. Flux Chemistry and Conductivity

The slag basicity is related to conductivity and oxygen potential of the slag. In general, conductivity of the slag increases with increasing slag basicity while the oxygen potential decreases.

Strong slag pool convection occurs when high resistivity, high oxygen potential flux is used, due to the steep temperature gradient between the fusion line and the weld center. This results in dendrite fragmentation. Oxide particles may also act as nucleants for dendrites, resulting in finer dendrites. In addition, an excessive oxygen potential and low basicity flux will increase the amount of inclusions. It has already been suggested[89-94, 97-104] that oxygen inclusions at the interdendritic boundaries and the subsequent austenite boundaries in weld metal significantly influence the transformation characteristics of weld metal and kinetics and morphology of ferrite formation. They do this by moving the transformation curve to shorter delay time and higher temperature (Fig. 67). The inclusions tend to reduce the austenite

grain size, favoring the formation of blocky, grain boundary and widmanstatten ferrite because the inclusions inhibit the movement of the extensive planar front of the proeutectoid phase by pinning and dragging effects(Type I of Figs. 22 and 26).

In the welds using high conductivity and high basicity flux, the columnar dendrites develop earlier with large dendrite arm spacing due to greatly increased heat input efficiency (Fig. 28)(Eq. 18) and increased local solidification time. The established relationship between the weld metal solidification structure and subsequent solid state macro/microstructures in normal ES welds[125] can not be applied to the ES welds made using these fluxes. Even if the solidification structure showed the columnar dendrites with noticiable side arms, the subsequent solid state macrostructure did not show thin columnar grains (Type III of Fig. 22). The reason for the development of only coarse columnar grains was probably due to low impurity levels. The weld pool was vigorously desulfurized and exhibited extremely low oxygen potential (Table 4). The low impurity level at the intercolumnar dendritic region did not restrict lateral austenite growth and thereby induced coarse grain structures.

The formation of a high volume fraction of blocky and coarse acicular type ferrites was presumably due to high heat input and low oxygen content. The effect of oxygen concentration on the ferrite content in ES welds is shown in Fig. 27. Many investigators [85-90] postulated that oxygen inclusions can directly nucleate acicular ferrite and showed that intermediate weld metal oxygen level (200-300ppm) along with appropriate dispersion and size (around 0.3 um dia.) gave a primarily acicular ferritic structure. The results of this study also demonstrated

that both adequate number and appropriate dispersion of weld metal oxygen inclusions were an essential requirement for the nucleation of acicular ferrite. The best microstructures for maximum acicular ferrite were obtained with fluxes having a basicity index of about 1.2, which corresponds to around 200 ppm of oxygen and 50 % acicular ferrite at weld center of A36 welds using mild steel electrodes(Fig. 68).

From this study, the coarse and thin columnar grains in welds were directly influenced by weld metal oxygen content (Fig. 26). In normal welds, around 50 % of thin columnar grains in the weld was observed in the range of 200-300ppm of oxygen content. The percentage of thin columnar grains was substantially decreased with decreasing weld metal oxygen content, and 100 % coarse columnar grains were obtained at around 80 ppm of oxygen. This is equivalent to a basicity index of 3.6 (without CaF2 term) and flux electrical conductivity of 3.3/(Ωcm) at 1700 ^{c}C. 100% thin columnar grains were obtained at oxygen contents exceeding 600 ppm in welds.

3. Alloy Addition

Small additions of Ni-Mo into the weld pool dramatically influenced the solidification structures as well as the microstructures of A36 and A588 weld metals (Type V structures of Fig. 22) deposited by ESW. Increasing the alloy content increases the constitutional supercooling (Fig. 8), which induces earlier development of columnar or equiaxed dendrites. As already discussed, the solidification structures follow a particular order, ie. planar -- cellular -- cellular dendrite -- columnar dendrite -- equiaxed dendrite with increasing constitutional supercooling. Thus the solidification structures will be one step to

several steps upgraded by alloy additions, depending on the amount of addition. This was analogous to a decrease in the $G/R^{\frac{1}{2}}$ ratio. The development of equiaxed dendrites was believed that the fragile tips of growing dendrites were broken away from the main dendrites and carried into the supercooled region to provide nuclei to form equiaxed dendrites.

In addition to the formation of equiaxed dendrite, the rightward displacement of the maximum delta-Fe composition in the Fe-Ni and Fe-Mo phase diagrams, (compared to the Fe-C diagram), also promotes long range primary delta-ferrite dendrites. This increases the temperature stability range of delta-ferrite, which results in longer homogenization time. All of these effects provided a relatively beneficial (crack resistant) solidification structure.

Solid state microstructure also showed perfect equiaxed grains with high volume fraction of acicular ferrite (Type V of Fig. 22). Nickel is an austenite stabilizer and therefore tends to shift the transformation curve to a longer delay time. Thus nucleation of high temperature transformation products (blocky, grain boundary and widmanstatten ferrite) can be suppressed to a large degree of under cooling below the AC3 temperature by the addition of Ni. The retarded austenite grain growth was due to interdendritic impurity segregation, because alloy additions promoted early development of columnar dendrites. The thin austenite grains subsequently transformed to refined thin grain boundary ferrite with a high volume fraction of acicular ferrite.

Fig. 69 illustrates the combining effect of oxygen and alloy contents on the volume fractions of coarse columnar, thin columnar and equiaxed zones in the weld metal. The proportions of the coarse columnar, thin columnar and equiaxed zones varied with alloy content and

oxygen concentration in the weld. Generally, as these variables increased, the size of the thin columnar zones increased, and with further increase of alloy content and oxygen concentration in the weld, the size of the equiaxed zone increased at the expense of the thin columnar zone. Increased welding speed also increased the equiaxed zone size.

C. Slag Conductivity

The relationship between experimentally determined electrode feed rate and empirically calculated[61] conductivity of slag at 1700° C at constant current and voltage is shown in Fig. 70. The decrease of electrode feed rate with increasing slag conductivity at constant current and voltage is associated with Ohm's law in ESW.

An increase in electrode feed rate drives the electrode closer to the molten metal pool. This decreases the current path between the electrode tip and the molten metal pool surface. The current path length must decrease with increasing slag resistivity if absolute resistance is to be kept constant, as required in the constant current and voltage case. This leads to the current path length, in a high resistivity slag, being effectively decreased by means of deep electrode extension into the slag pool, ie. short distance between the electrode tip and molten metal pool surface in order to maintain constant voltage and current (Fig. 12). For a low resistivity slag, the effect is just the opposite.

The high resistivity slag is not efficient in transferring heat to the side wall. This results in build up of heat at the electrode tip inducing localized boiling of the slag and submerged arcing. These effects increase the electrode melting rate and lower base metal dilution, since most of the heat is generated in the proximity of the electrode tip.

An exposed arc between guide tube and surface of the molten slag occurs while using a high conductivity slag. At low electrode feed rate, the current path length through the molten slag is long and the area in which heat is generated is large and diffused. As a result, high base

metal dilution was observed even if some of the heat generated is consumed in exposed arcing (Fig. 28).

D. Heat Input on HAZ Size

The magnitude and direction of the thermal gradient are direct measures of the ability to extract heat from the weld pool to the cooler surroundings. Therefore, the larger the value of the thermal gradient, the greater the heat-extraction capacity[127]. In the case of high heat input, an elliptical-shaped weld pool was observed and the direction of the maximum thermal gradient continuously changes from the fusion line to the weld centerline. This reflects the ability to extract more heat in the longitudinal direction (weld metal side) as compared to the transverse direction (base metal side) as solidification proceeds from the fusion line towards the weld centerline. However, the opposite is true in the low heat input case, which results in a kite-shaped weld pool. The kite-shaped weld pool shows a larger maximum temperature gradient in the fusion line region, compared to an elliptical weld pool.

If a standard weld (600A, 40V and 32mm gap) and a narrow gap weld (1000A, 40V and 19mm gap) with the same slag pool height are compared, the narrow gap weld illustrates greater heat strength ($Q = VIt$) at a given time and requires a smaller volume of slag pool. This will increase the slag temperature. In addition, the distance between electrode and base metal is also small compared to a standard gap weld. All of these conditions (magnitude and direction of temperature gradient, heat strength, slag volume, slag temperature and distance between electrode and base metal) provide increased heat transfer efficiency through both the slag pool and the molten metal pool to preheat and melt the base metal. The opposite is true in a standard weld. However, by considering the increased exposure time of the slag pool to the base

metal in a standard weld versus a narrow gap weld, as measured by welding speed, the net heat efficiency is thought to be almost identical in both welds.

Molten metal pool shape also greatly affects the heat distribution pattern toward base metal. Plate edges accumulate more heat, while the mid-thickness region delivers heat easily, due to radial shape. Thus, large HAZ size in plate edges and small HAZ size in mid-thickness region are produced[Fig. 44]. This effect is greater in a standard weld. If a mean value of HAZ size measurements at the edges and at the center of the weld is taken, total HAZ size, in general, will be greater in a standard weld (Table 6).

E. Quartz Grain Refinement

1. Heat Generation and Distribution

The quartz shrouded guide and electrode filler metal extended deeply into the slag pool(Fig. 45) inducing a low form factor(Fig. 50). A large portion of the current flows through the slag directly below the electrode tip to the bottom of the slag bath. Thus, much of the heat generated in the process is concentrated in a relatively small local region of the slag. The jet stream of superheated/vaporized slag, generated by Joule heating at the electrode tip area, was sufficient to blow the slag out and locally boil the slag introducing a gas envelope which caused a persistent arcing (Fig. 46).

The manner in which the thermal energy is distributed in the quartz shrouded welds has a profound effect on weldment soundness. The severe lack of fusion found in these welds was attributed to the heat loss by arcing, vigorous agitation of the molten pool, coldness and high resistivity of slag and poor heat transfer toward base metal sides. The quartz also requires heat to melt(Table 10). Slow welding speeds were required to increase thermal efficiency by changing the heat flow direction and molten pool shape from a deep kite-shaped weld pool to a circular weld pool. A slow welding speed also induces a less intense circulation of the molten pool resulting in improved utilization of the energy.

2. Weld Metal Grain Refinement

The mechanisms of grain refinement and dendrite renucleation were investigated. The application of the quartz shroud resulted in

substantial grain refinement because the guide tube provided a narrow jet stream of superheated/gaseous slag and a sharp thermal gradient between weld center and the unmelted base metal due to a high thermal shielding of guide tube and electrode(Fig. 71)(Table 10). Consequently, the intense forced convective field, in addition to electromagnetic Lorentz force, permitted an extensive dendrite multiplication by fragmentation or remelting of previously solidified dendrites protruding ahead of the advancing solid-liquid interface(Fig. 53).

The grain refinement shown in the room temperature microstructure was believed to be due to interdendritically segregated oxygen inclusions. Oxygen inclusions have a great influence on steel transformation behavior through its austenite grain growth inhibition effect and ferrite transformation acceleration effect[85-90].

The mechanically broken short columnar dendrites in a quartz grain refined weld still followed the maximum temperature gradient, but when Nickel alloy was added to these welds, perfect equiaxed dendrites developed with random dendritic growth due to a high degree of constitutional supercooling. Alloy additions also effectively controlled the solid-state microstructures giving high amount of acicular ferrite (Type V of Fig. 22).

From the study of the quartz shrouded guide tube and flux modification, the conditions required for as-welded thin grain refined ES welds were an uniform interdendritic distribution of a fairly high amount of oxide particles (around 600ppm of oxygen) throughout the weld and optimum conductivity of flux (less than 2.0/(Ω cm)) at 1700° C. Conductivity was controlled to not give melt-back of quartz. The development of columnar dendrites or dendrite fragments throughout the

weld was necessary to induce uniform oxide particles segregation interdendritically.

The greater resistance to hot cracking previously observed(Fig. 72) [4, 5] was believed to be associated with uniform distribution of impurities by dendrite fragments produced in weld center region.

Consequently, the outstanding capability of the quartz shroud is to increase the hot cracking resistance, promote uniform grain refined structures and uniform mechanical properties throughout the weld. However, the reliability in producing defect free welds and industrial applications is still in doubt.

VI. CONCLUSIONS

Based on the study of dendrite reorientation and renucleation during weld metal solidification, the following can be concluded :

1) Dendritic structures were significantly affected by solute bands. Several phenomena occuring at the solute bands were:

a) dendrite arm growth through solute bands

b) direct dendrite arm bending

c) partial and complete dendrite arm remelting

d) new dendrite nucleation

e) change of dendrite morphology and arm spacing

2) Development of tertiary dendrite arms was dependent upon a unique combination of the temperature gradient vector and primary dendrite arm growth direction

3) Pool shape, alloy and oxygen contents significantly affected extents of solute band and dendrite reorientation and renucleation

4) Microstructural characteristics of the weld were dependent upon solidification induced compositional variations.

From the comprehensive welding parametric studies of ESW A36 and A588 steels, the following can be concluded :

1) A new classification of macrostructures for ES welds has been developed. Five characteristric types of weld metal grain structures were proposed as a function of welding parameters, alloy content, oxygen potential and basicity of the slag.

2) Thin columnar structures were a result of high weld metal oxygen concentrations.

3) Fully coarse columnar structures occurred with highly basic, low

oxygen potential slags.

4) Equixed grains at the weld center were promoted by Ni-Mo addition, high oxygen content, and/or fast welding speeds.

5) Minor additions of Ni and Mo substantially increased the weld metal's resistance to hot cracking and increased the volume fraction of acicular ferrite.

The parametric study of narrow gap (19 mm) ESW on 50 mm and 76 mm thick A36 and A588 steel plates using wing or web guide plates has led to the following conclusions :

1) The optimum conditions for narrow gap ESW over standard conventional welds can provided increased welding efficiency, deposition rate, resistance to solidification cracking and improved microstructures.

2) Wing or web guide plates provided uniform penetration and greater current carrying capacity.

3) An increase in Charpy toughness was observed in the weld center region when compared to the standard welds.

The investigation of quartz grain refinement through dynamic stimulation in large ES welds has led to the following conclusions :

1) Intense stirring of the weld pool and significantly increased nucleation of polygonal, grain-boundary and widmanstatten ferrite due to excessive oxygen potential in the manganese silicate fluxes with quartz dissolution was revealed and was responsible for grain refinement.

2) Higher voltage (around 48V) than that used in welds without quartz shielding was necessary to generate sufficient heat to melt the base metal due to the thermal shielding behavior of the quartz shroud. Further over potential led to severe arcing.

3) The conductivity and basicity (oxygen potential) of slag were very important in the quartz shielded grain refinement.

4) Uniform Charpy impact toughness throughout the weld was produced.

REFERENCES

1. Skirinar, J., Metals Technical Conf., International Institute of Welding, Sydney, Australia, (1976)

2. Liby, A. L., et al., Quarterly of the Colorado School of Mines, 1, p.41, (1974)

3. Dorschu, K. E., et al., Welding J., p.710, (Nov. 1973)

4. DoT-FHWA Contract, DoT-FH-11-9612 by Battelle Pacific Northwest Lab. and Oregon Graduate Center, Final Report, "Improved Integrity and reliability in structural steel ESW" (1982)

5. Venkataraman, S., Ph. D. Thesis, Oregon Graduate Center (1982)

6. Culp, J. D., Welding J., p.27 (July, 1979)

7. Chalmers, B., "Physical Metallurgy", John wiley and sons, Inc., New York, (1962)

8. Eastering, K., "Introduction to the physical metallurgy of welding", Butterworths and co., Ltd., (1983)

9. Savage, W. F., et al., Welding J., p.175s, (April, 1965)

10. Bray, R. S., et al., Welding J., p.181s, (May, 1969)

11. Loper, C. R., et al., Welding J., p.171s, (Apr., 1969)

12. Tiller, W. A., et al., Acta. Meta., Vol.1, p.428, (July, 1953)

13. Loper, C. R., et al., Welding J., p.126s, (Mar., 1974)

14. Sarreal, J. A., et al., Met. Trans., Vol.17A, p.2063, (Nov., 1986)

15. Laxmanan, Acta. Meta., Vol.33, p.1023, (1985)

16. Hunt, J. D., Proc. of the Int'l Conf. on Soli. and Casting of Metals held at the Univ. of Sheffield on 18-21 (July, 1977)

17. Trivedi, R., J. of Crystal Growth, Vol.49, p.219, (1980)

18. Savage, W. F., et al., Welding J., p.522s, (Nov., 1968)

19. Arata, Y., et al., Tran. of JWRI, Vol.5, No.1, p.47, (1976)

20. Yoshimura, H., et al., Welding J., p.132s, (Mar., 1972)

21. D'Annesa, A. T., Welding J., p.41s, (Feb., 1970)

22. Nakagawa, H., et al., Tran. JWS, Vol.2, p.10, (1971)

23. Kato, M., et al., Tran. JWS, Vol.3, p.59, (1972)

24. Nakagawa, H., et al., Tran. JWS, Vol.2, p.1, (1971)

25. Jackson, K. A., et al., Tran. Met. Soc. AIME, Vol.236, p.149, (1966)

26. Johnston, M. H., et al., Met. Trans., Vol.13B, p.85, (Mar., 1982)

27. D'Annessa, A. T., Welding J., p.569s, (Dec., 1966)

28. Doherty, R. D., et al., Mat. Sci. and Eng., Vol.65, p.181 (1984)

29. Bridge, M. R., et al., Met. Tran., Vol.15B, p.581, (Sep., 1984)

30. Devletian, J. H., et al., Paper presented at the 67th annual AWS Con., Atlanta, GA, (1986)

31. Kato, M., et al., Met. Trans.,Vol.9A, p.1795, (Dec., 1978)

32. Cheever, D. L.., et al., Welding J., p.179s, (Apr., 1969)

33. Gurev, H. S., et al., Welding J., p.298s, (July, 1963)

34. Ishizaki, K., et al., J. of JWS, Vol.32, p.38, (1963)

35. Solari, M., et al., Welding J., Vol.56, p.274s, (Sep., 1977)

36. Okamoto, T., et al., Tran. ISIJ, Vol.21, p.641, (1981)

37. Flemings, M. C., et al., "Solidification Processing" McGraw Hill, (1974)

38. Bower, T. F., et al., Tran. of the Meta. Soc. of AIME, Vol.236, p.624, (May, 1966)

39. Taha, M. A., Metals Science, p.9, (Jan., 1979)

40. Quested, P. N., et al., Mat. Sci. and Eng., 65, p.171, (1984)

41. MaCartney, D. G., et al., Acta. Meta., Vol.29, p.1851, (1981)

42. Hurtuk, D. J., et al., Proc. of an Int. Conf. on Soli., London, (July, 1977)

43. Horwath, J. A., et al., Acta. Meta., Vol.10, p.1037, (1962)

44. Lanzafame, J. N., et al., Welding J., p.226s, (May, 1973)

45. Somboonsuk, K., et al., Met. Tran., Vol.15A, p.967, (June, 1984)

46. Kattamis, T. Z., et al., Tran. Met. Soc. AIME, Vol.239, p.1504, (Oct., 1967)

47. Taha, M. A., et al., Met. Tran., Vol.13A, p.2131, (Dec., 1982)

48. Okamoto, T., et al., J. of Crystal Growth, Vol.29, p.141, (1975)

49. Burden, M. H., et al., Met. Sci., p.156, (May, 1976)

50. Takahashi, T., et al., Tran. ISIJ, Vol.16, p.283, (1976)

51. Duckworth, W. E., et al., "Electroslag Refining", Chapman and Hall, Ltd., London, (1969)

52. Jones, J. E., et al., Welding J., p.245s, (Sep., 1980)

53. Tuliani, S. S., et al., British Nuclear Energy Soc., p.327, (Apr., 1979)

54. Gurev, H. S., et al., Welding J., p.298s, (July, 1963)

55. Thomas. R. D., Welding J., Vol.39, p.111, (Feb., 1960)

56. Frost, R. H., et al., Welding J., p.1s, (Jan., 1981)

57. Turpin, R. B., M.S. Thesis, Oregon Graduate Center (1983)

58. Patchett, B. M., et al., Welding and Metal Fab., p.216, (June, 1973)

59. Vaidya, V., et al., Welding and Metal Fab., p.345, (June, 1976)

60. Mitchell, A., et al., Met. Trans., p.3361, (Dec., 1971)

61. Hara, et al., Trans. of ISIJ, Vol.23, p.1053, (1983)

62. Technical Guide for ESW, EW-493, Hobart Brothers Co., Troy, OH

63. Debroy, T., et al., Met. Trans., Vol.11B, p.593, (Nov., 1980)

64. Dilawari, A. H., et al., Met. Trans., Vol.9B, p.371, (Sep., 1978)

65. Dorschu, K. E., et al., Welding J., p.710, (Nov., 1973)

66. Ito, Y., et al., Advanced Welding Technology, JWS, p.513, (1975)

67. Khakimov, A. N., et al., Welding Prod., Vol.1, p.39, (1974)

68. Smirnov, S. A., et al., Aut. Welding, Vol.9, p.45, (1973)

69. Eichhorn, F., et al., Schweissen and Schneiden, Vol.28, No.6, p.210, (1976)

70. Reynolds, G. H., MSNW, Inc., Report, (June, 1984)

71. Heintze, G. N., Australian Welding Research, p.32, (Dec., 1984)

72. Weiser, P., et al., J. of Metals, Vol.19, p.44, (June, 1967)

73. Garland, J. G., Metal Construction, p.121, (June, 1974)

74. Bramfitt, B. L., Met. Trans., Vol.1, p.1987, (1970)

75. Davies, G. J., et al., Int. Met. Reviews, Vol.20, p.83, (1975)

76. Gradwell, K. J., et al., Grain size control in cast metals, Loughborough, (Dec., 1973)

77. Johnston, M. H., et al., Met. Trans., Vol.13B, p.85, (Mar., 1982)

78. Brown, D. C., et al., Welding J., Vol.41, p.241s, (1962)

79. Goodell, S. E., et al., Welding J., Vol.49, p.372, (1963)

80. Rienko, F., et al., Welding J., Vol.50, p.222s, (1971)

81. Campbell, J., Int. Metals Reviews, No.2, p.71, (1981)

82. Jackson, K. A., et al., Tran. Met. Soc. AIME 236, p.149, (1966)

83. Hunt, J. D., Mat. Sci. and Eng., Vol. 65, p.75 (1984)

84. Glover, A. G., et al., Welding J., Vol.56, p.267s, (Sep., 1977)

85. Dolby, R. E., Metals Tech., Vol.10, p.349, (Sep., 1983)

86. Morcinek, p., et al., Microalloying, 75, p.272, (1975)

87. Choi, C. L., et al., Welding J., p.232s, (Aug., 1978)

88. Harrison, P. L., et al., Welding and Metal Fab., p.161, (April, 1981)

89. Abson, D. J., et al., Proc. Intl. Conf. on Trends in steels and consumables for welding, London, p.75, (Nov., 1978)

90. Cochrane, R. C., et al., Intl. Conf. on Trends in Steels and Consumables for welding, London, p.103, (Nov., 1978)

91. Terashima, H., et al., Welding J., Vol.63, p.173s, (1984)

92. Ricks, R. A., et al., J of Mat. Sci., Vol.17, p.732, (1982)

93. Kayali, E. S., et al., J of Mat. Sci. Lett., Vol.2, p.123, (1983)

94. Dolby, R. E., Metal Construction, Vol.14, No.3, p.148, (1982)

95. Ohashi, T., et al., Tran. ISIJ, Vol.17, p.262, (1977)

96. Bramfitt, B. L., Met. Trans. 1, p.1987, (1970)

97. Liu, S., et al., Welding J., p.139s, (June, 1986)

98. Fleck, N. A., et al., Welding J., p.113s, (May, 1986)

99. Harrison, P. L., et al., J. of Mat. Sci., Vol.16, p.2218, (1981)

100. Yoshinori I., et al., Metal Cons., p.472, (Sep., 1982)

101. Matsuda, F., et al., Tran. JWRI, Vol.14, No.2, p.135, (1985)

102. Ferrante, M., et al., J. of Mat. Sci., 17, p.3293, (1982)

103. North, T. H., et al., Welding J., p.63s, (Mar., 1978)

104. Dallam, C. B., et al., Welding J., p.140s, (May, 1985)

105. Kirkaldy, J. S., Met. Trans., Vol.4, No.10, p.2327, (1973)

106. Dorschu, K. E., WRC Bulletin 231

107. Evans, G. M., Welding J., p.67s, (Mar., 1980)

108. Grong, O., et al., Int. Metals Reviews, Vol.31, No.1, p.27, (1986)

109. Abson, D. J., et al., Int. Metals Reviews, Vol.31, No.4, p.141, (1980)

110. Nolan, M. V., et al., Welding and Met. Fab., p.464, (Nov., 1969)

111. Benter, W. P., National Cooperative Highway Research Program Report 201, Transportation Research Board, Washington D.C., (May, 1979)

112. Dieter, G. E., Mechanical Metallurgy, 2nd Ed., McGraw-Hill Co.

113. Cottrell, C.L.M., Metal Construction, p.740, (Dec., 1984)

114. Thomas, H., Welding Process Technology, Cambridge Univ. Press, (1977)

115. American Association of State Highway and Transportation Officials (AASHTO) Specification M270-77, p.781

116. Structural Welding Code, AWS D1.1, AWS, (1982)

117. Davies, G. J., Solidification and Casting, Univ. of Cambridge, Prentice Hall Co.

118. Okamoto, T., et al., J. of Crystal Growth, Vol.29, P.131, (1975)

119. Murakami, K., et al., Acta. Metall., Vol.31, No.9, P.1425, (1983)

120. Chalmers, B., Principles of Solidification, John Wiley and Sons, Inc., (1967)

121. Solomon, H. D., Treatise on Mat. Sci. and Technology, Vol.25, p.525, (1983)

122. Savage, W. F., et al., Welding J., p.185s, (Feb., 1966)

123. Widgery, D. J., et al., Weld. Inst. Res. Bulletin, Vol.16, p.277, (1975)

124. Bhadeshia, H. K. D. H., et al., Acta Metall., Vol.33, No.7, p.1271, (1985)

125. Yu, D., et al., Proc. of JDC, Univ. Research Sym., The State of Art Nippes, et al., (Eds), ASM, Metals Park, OH, p.21, (1986)

126. Lancaster, J. F., "Metallurgy of Welding" George Allen and Unwin, p.54, #rd Ed., (1980)

127. Savage, W. F., et al., Welding J., p.213s, (Aug., 1976)

Table 1. Compositions of base metals, electrodes and guide plate materials

Material	C	Mn	Si	Cr	Ni	Mo	Cu	S	P	V
A36	0.17	0.92	0.20	0.02	0.10	--	0.20	0.02	0.01	0.06
A588	0.18	1.20	0.37	0.56	0.16	--	0.32	0.02	0.01	0.08
Hobart-25p	0.11	1.12	0.50	--	--	--	0.32	0.02	0.02	--
Linde-WS	0.09	0.50	0.30	0.55	0.50	--	0.30	0.03	0.02	--
Hobart PS-588*	0.07	1.10	0.50	0.50	0.80	1.00	0.45	0.01	0.01	--
Airco-AX90	0.08	1.40	0.46	0.06	2.10	0.40	--	0.02	0.02	0.01
Stoody-TW8544*	0.03	1.20	0.45	--	2.30	0.45	--	0.02	0.02	0.05
17-4 PH	0.07	1.00	1.00	16.5	3.50	--	3.50	--	0.04	0.03
304	0.08	2.00	1.00	18.2	9.50	--	--	0.03	0.05	--
309	0.20	2.00	1.00	22.3	13.0	--	--	0.03	0.05	--
1010	0.10	0.45	--	--	--	--	--	0.05 (max)	0.04 (max)	--

Balance : Fe

* Powder-cored tubular wire

Table 2. Flux chemistries used in this study(wt.%)

1. Hobart PF201*

2. 100% CaF_2

3. Mixtures of CaF_2-Al_2O_3-CaO

   (1) 50% CaF_2 - 25% CaO - 25% Al_2O_3
   (2) 33% CaF_2 - 33% CaO - 33% Al_2O_3
   (3) 80% CaF_2 - 10% CaO - 10% Al_2O_3

4. Hobart PF201 + CaF_2-CaO-Al_2O_3 flux

   (1) $\frac{1}{2}$(Hobart PF201) + $\frac{1}{2}$(50% CaF_2 - 25% CaO - 25% Al_2O_3)
   (2) 2/3 (Hobart PF201) + 1/3(50% CaF2 - 25% CaO - 25% Al_2O_3)

* Hobart PF201 running flux chemistry

Compound	Amount (wt.%)
SiO_2	32.95
Mno	22.46
CaO	12.20
CaF_2	8.62
Al_2O_3	8.32
TiO_2	8.02
MgO	2.34
FeO	1.81
K_2O	0.88
Na_2O	0.57
P_2O_5	0.05

Table 3. Significant variables promoting each type of characteristic structure in A36 and A588 ES welds

	VOLTS (V)	AMP (A)	GAP (mm)	WELDING SPEED (mm/s)	FLUX		REMARK
					OXYGEN (ppm)	BASICITY INDEX	
TYPE I	35 - 45	600	25 - 32	>0.28	HIGH >600	ACIDIC <0.7	HIGH O
TYPE II	35 - 45	500 - 1100	19 - 32	0.25 - 0.75	250	NEUTRAL 0.7	COMMERCIAL PRACTICE
TYPE III	35 - 45	600	19 - 32	0.25 - 0.30	LOW 80	BASIC 3.6	LOW O LOW IMPURITY
TYPE IV	35 - 40	>1100	19	>0.75	250	NEUTRAL 0.7	HIGH SPEED
TYPE V	35 - 45	600 - 1100	19 - 32	>0.28	<600	NEUTRAL 0.7	Ni - Mo STEEL FILLER

Table 4. Chemical compositions of weld metals of each type (wt.%)

Type	C	Mn	Si	Cr	Ni	Mo	Cu	Al	S	P	V	O (ppm)	N (ppm)
Type I	0.08	1.03	0.52	--	0.08	--	0.13	--	0.02	0.01	0.03	678	67
Type II & IV	0.15	1.12	0.34	0.02	0.08	--	0.17	--	0.03	0.01	0.03	246	58
Type III	0.14	1.24	0.33	0.03	0.05	--	0.09	0.01	0.01	0.01	--	83	54
Type V	0.14	1.32	0.36	0.03	1.12	0.20	0.10	0.02	0.02	0.01	0.01	260	55

Table 5. The optimum welding parameters of narrow gap(19mm) ESW

Material	Thickness	guide plate	Current Voltage
A36 A588	50 mm	Wing	900-1000 A 35-38 V
A36 A588	76 mm	Web	1000-1100 A 38-40 V

Table 6. Technical data comparison between standard and optimized narrow gap ESW

Item	Standard Gap (600A, 42V)	Narrow Gap (1000A, 38V)
Heat Input (KJ/mm)	100	68
Efficiency (VW/4a)	0.4	0.7
Welding speed (mm/sec)	0.25	0.58
BM Dilution(%)	45	47
BM Penetration(mm)	60	45
HAZ(mm)*	14	12

(Data taken from 50mm thick plate)

* Mean value of measurements at the edges and at the center of the HAZ

Table 7. Flux and slag chemistries before and after quartz dissolution

(composition : wt.%)

Material Analyzed	SiO_2	MnO	CaO	Al_2O_3	FeO	MgO	Rem't
PF 201	33.1	22.9	12.5	8.5	1.8	2.7	18.5
Slag	38.5	29.2	11.2	7.2	6.0	2.8	5.1

Table 8. Weld metal, and base metal CVN toughness summary

Alloy	Thickness (mm)	Weld Condition (gap, wire)*	CVN Data (Average of 3 tests)			
			WM½T (-18°C)**		Base metal (+4°C)	
			Joule	Ft lb	Joule	Ft lb
A36	50	SG, 25P	22	16		
		NG, 25P	27	20	83	61
	76	SG, 25P	13	10		
		NG, 25P	21	16	52	37
A588	50	SG, WS	5	4		
		NG, WS	15	11	50	37
	76	SG, WS	4	3		
		NG, WS	5	4	73	54

* SG : Standard gap (32mm) 25P : A36 matching filler
NG : Narrow gap (19mm) WS : A588 matching filler

** Average of 6 tests

Table 9. Transition temperatures at 20 Joules (15ft-lb) of CVN toughness

Alloy	Thickness (mm)	Weld Condition (gap, wire)*	20 Joules Notch Location $\frac{1}{2}$T
A36	50	SG, 25P	-19
		NG, 25P	-32
	76	SG, 25P	- 9
		NG, 25P	-22
A588	50	SG, WS	- 3
		NG, WS	- 9
	76	SG, WS	26
		NG, WS	20
A36	50	Quartz + Alloy	-65

* SG : Standard gap(32mm) 25P : A36 matching filler
NG : Narrow gap(19mm) WS : A588 matching filler

Fig. 1. Layout of consumable guide ESW process[Ref : 58]

Table 10. Data comparison between steel and quartz

ITEM	Steel	Quartz(SiO_2)
Required heat to melt (KJ/g)	1.3	2.14
Melting point (^oC)	1510	1713
Density (g/cm^3)	7.3	1.5

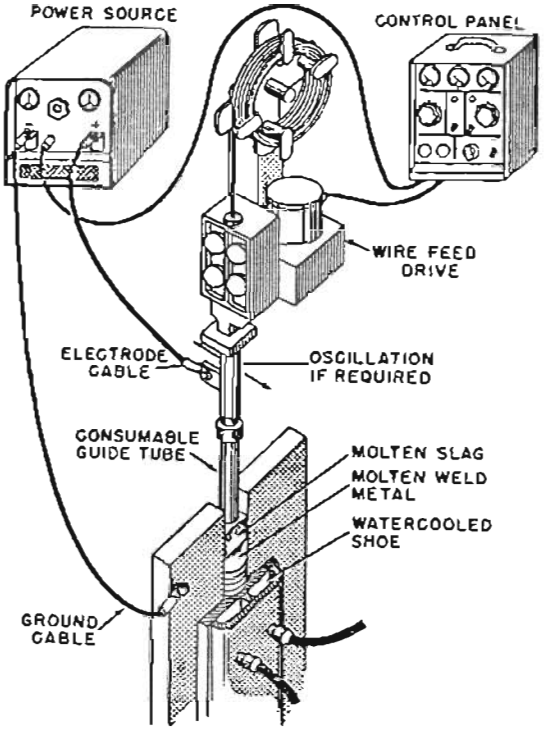

Fig. 1. Layout of consumable guide ESW process[Ref : 58]

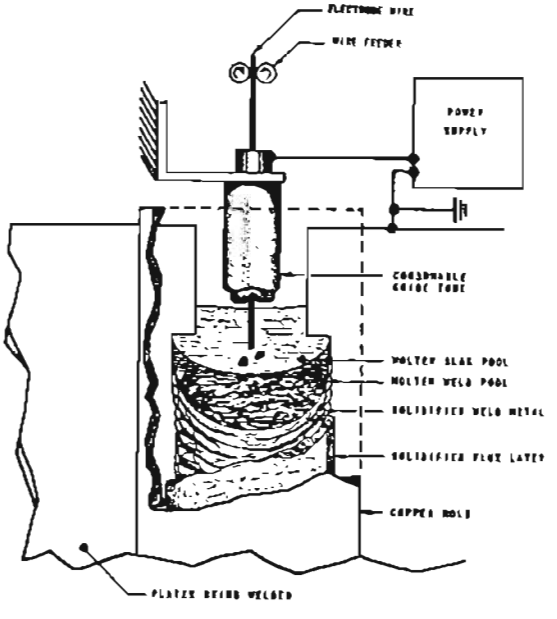

Fig. 2. Principle of consumable guide ESW process[Ref : 62]

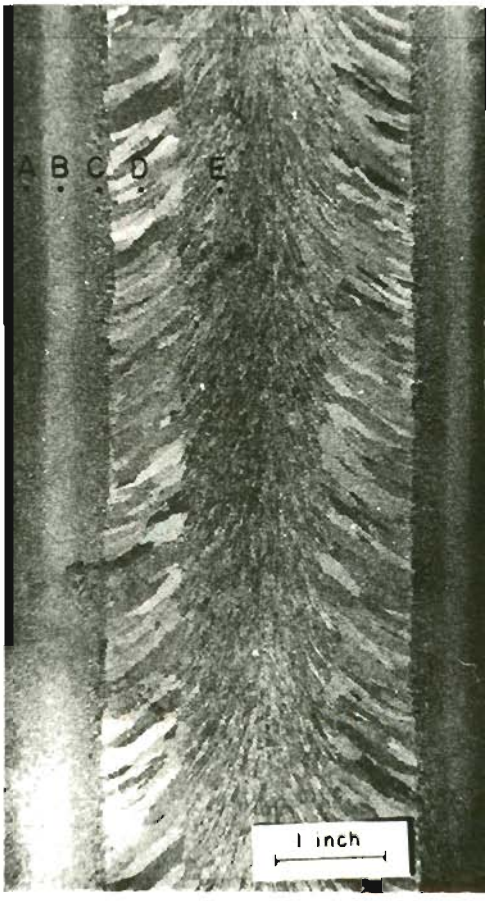

Fig. 3. Standard ES weld macrostructure indicating various structural zones [Ref : 4 and 5]

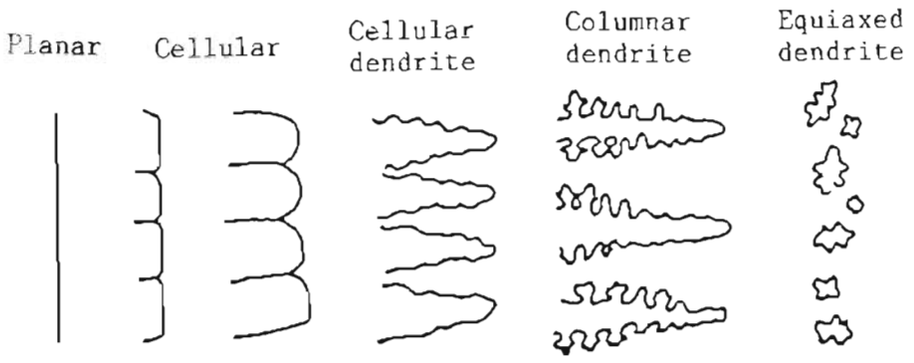

Fig. 4. Types of solidification structural growth mode

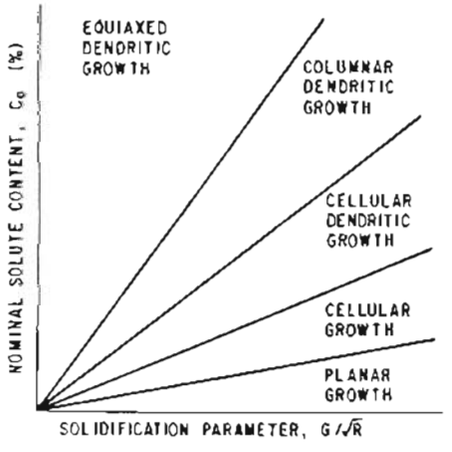

Fig. 5. Factors controlling the solidification structural growth mode

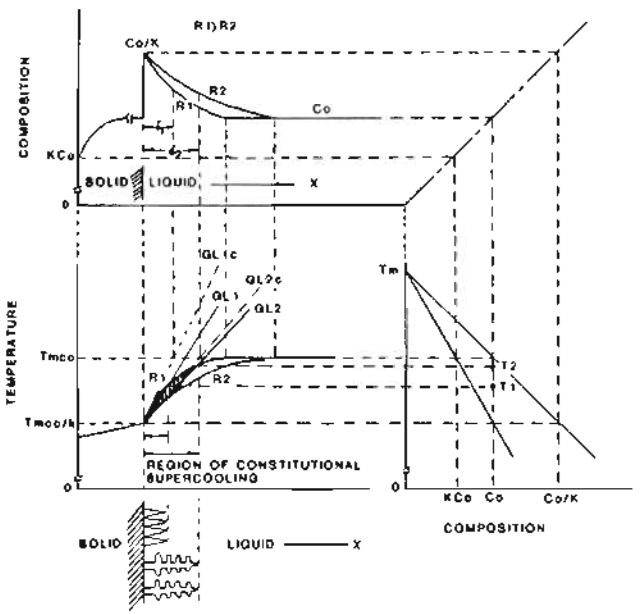

Fig. 6. Effect of welding parameters on the region of constitutional supercooling

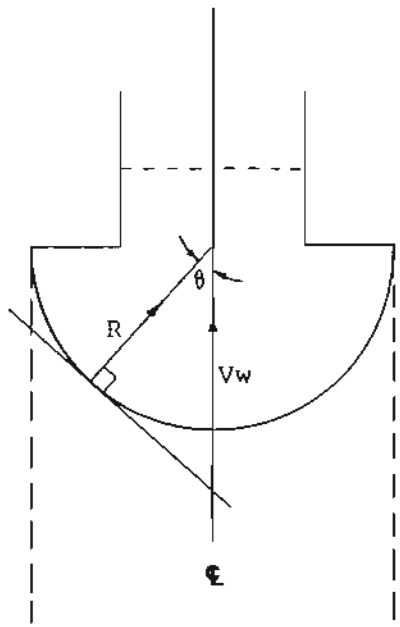

$$R = V_w \cdot \cos\theta$$

Fig. 7. Growth rate as a function of welding speed

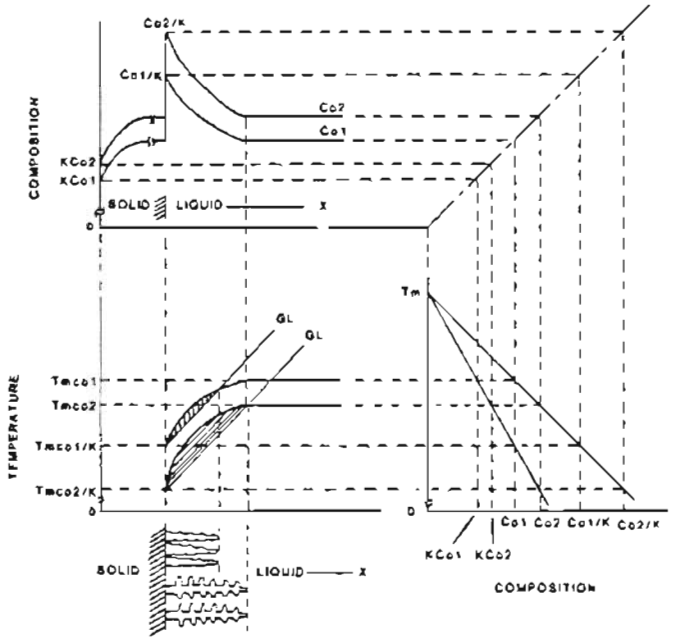

Fig. 8. Effect of alloy addition on the region of constitutional supercooling

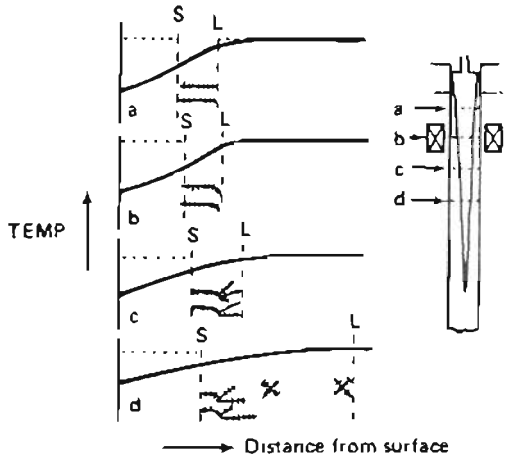

Fig. 9. Effect of fluid flow on dendrite curving
[Ref : 29]

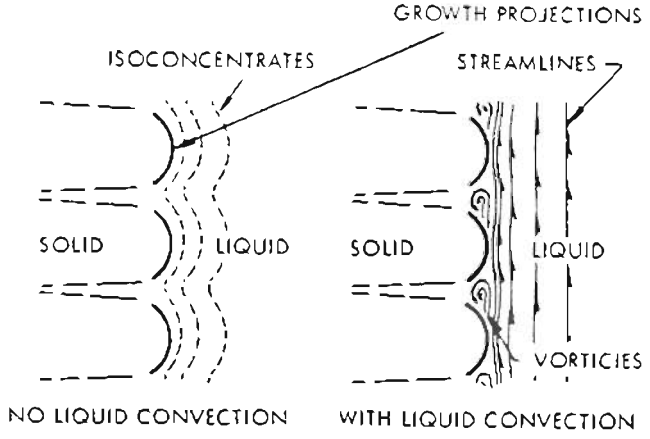

Fig.10. Solute segregation as an influence of liquid flow
[Ref : 27]

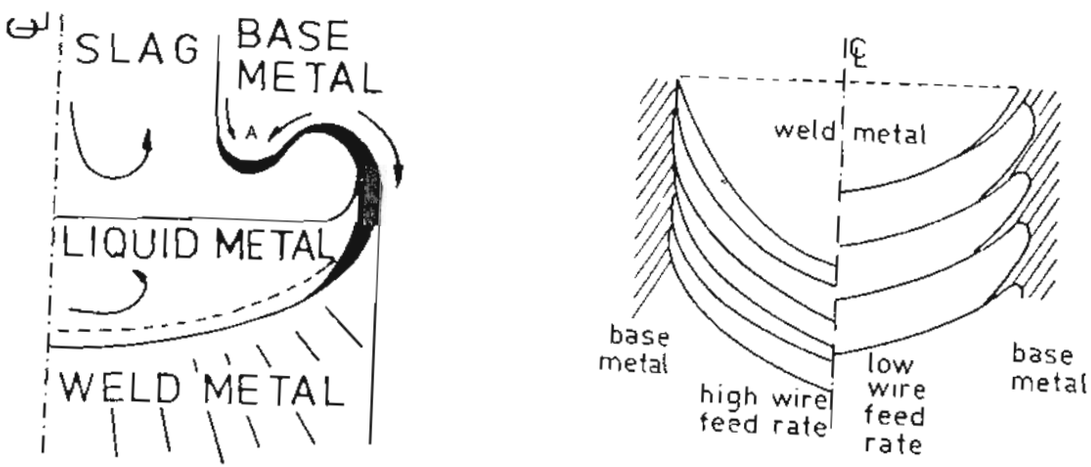

Fig. 11. Molten base metal sliding into the molten metal pool during ESW [Ref : 35]

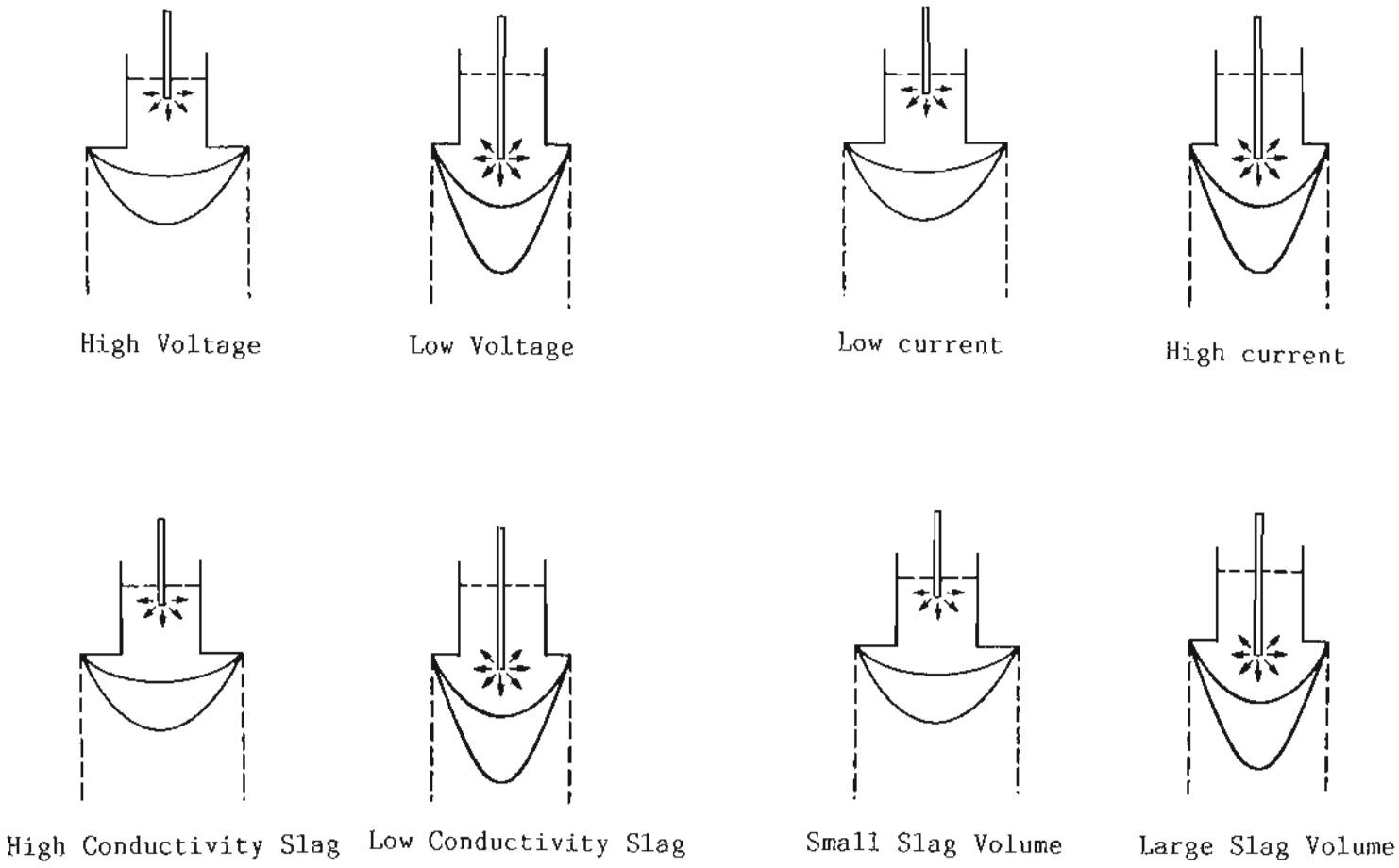

Fig. 12. Effect of welding parameters on weld pool characteristics

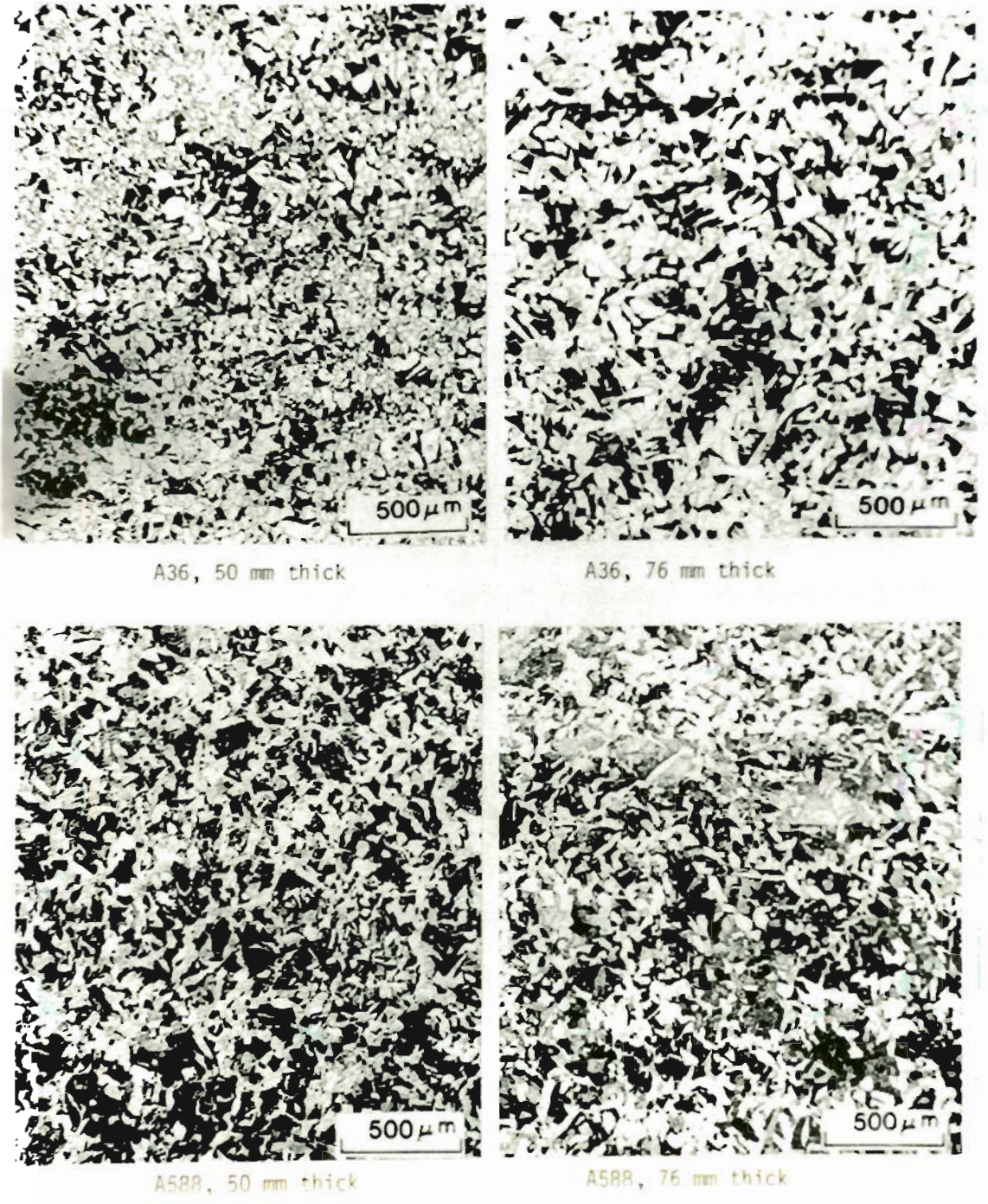

Fig. 13. Microstructures of as-received alloys

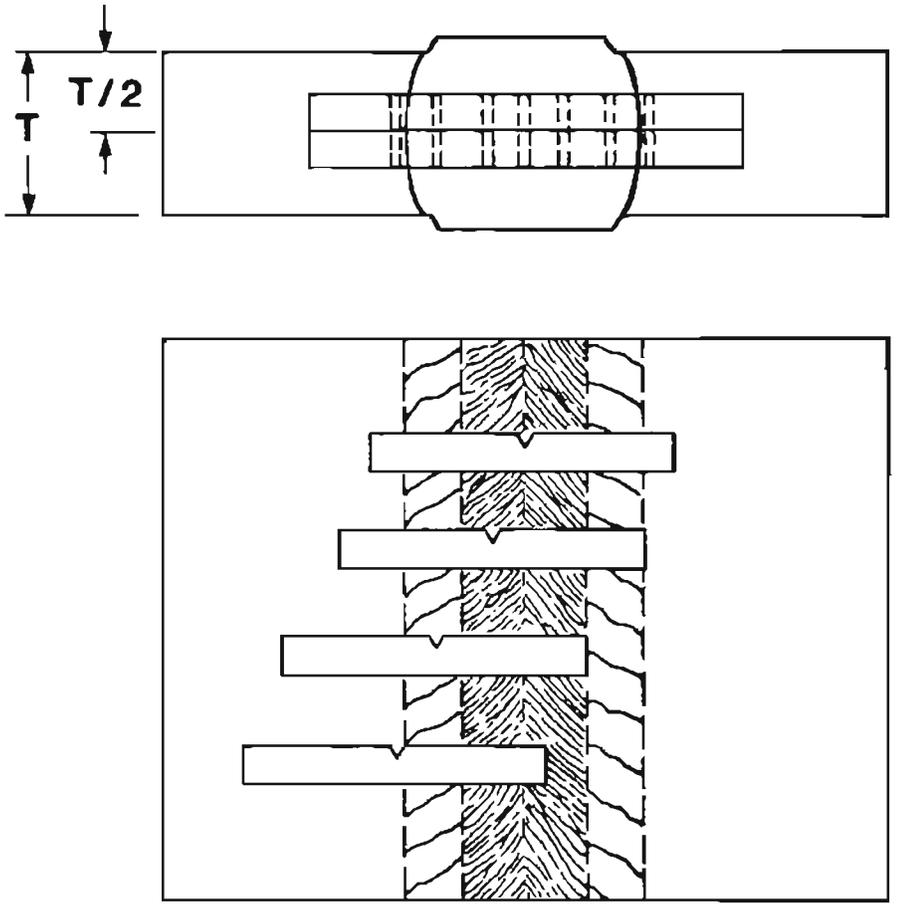

Fig. 15. CVN specimen location configuration for ES welds

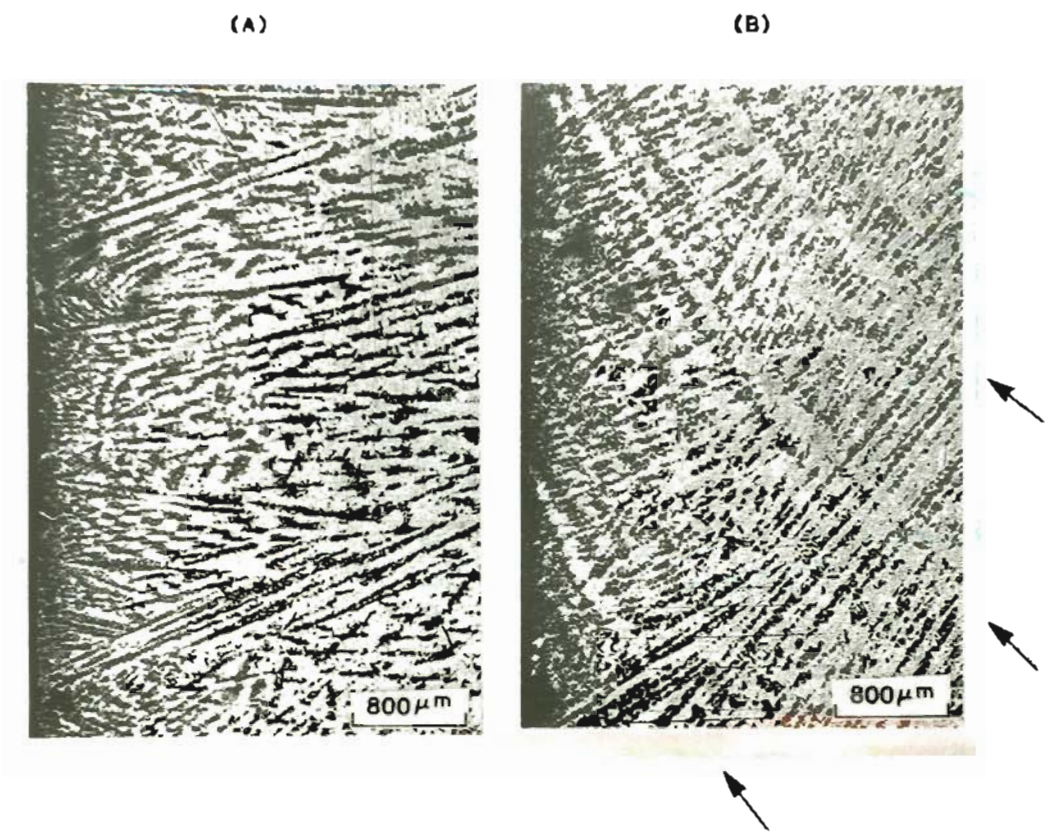

Fig. 16. The reorientation of primary dendrite arms as a function of the frequency of solute bands in ES welds :

(A) few solute bands
(B) multiple solute bands

* Arrows indicate typical solute bands

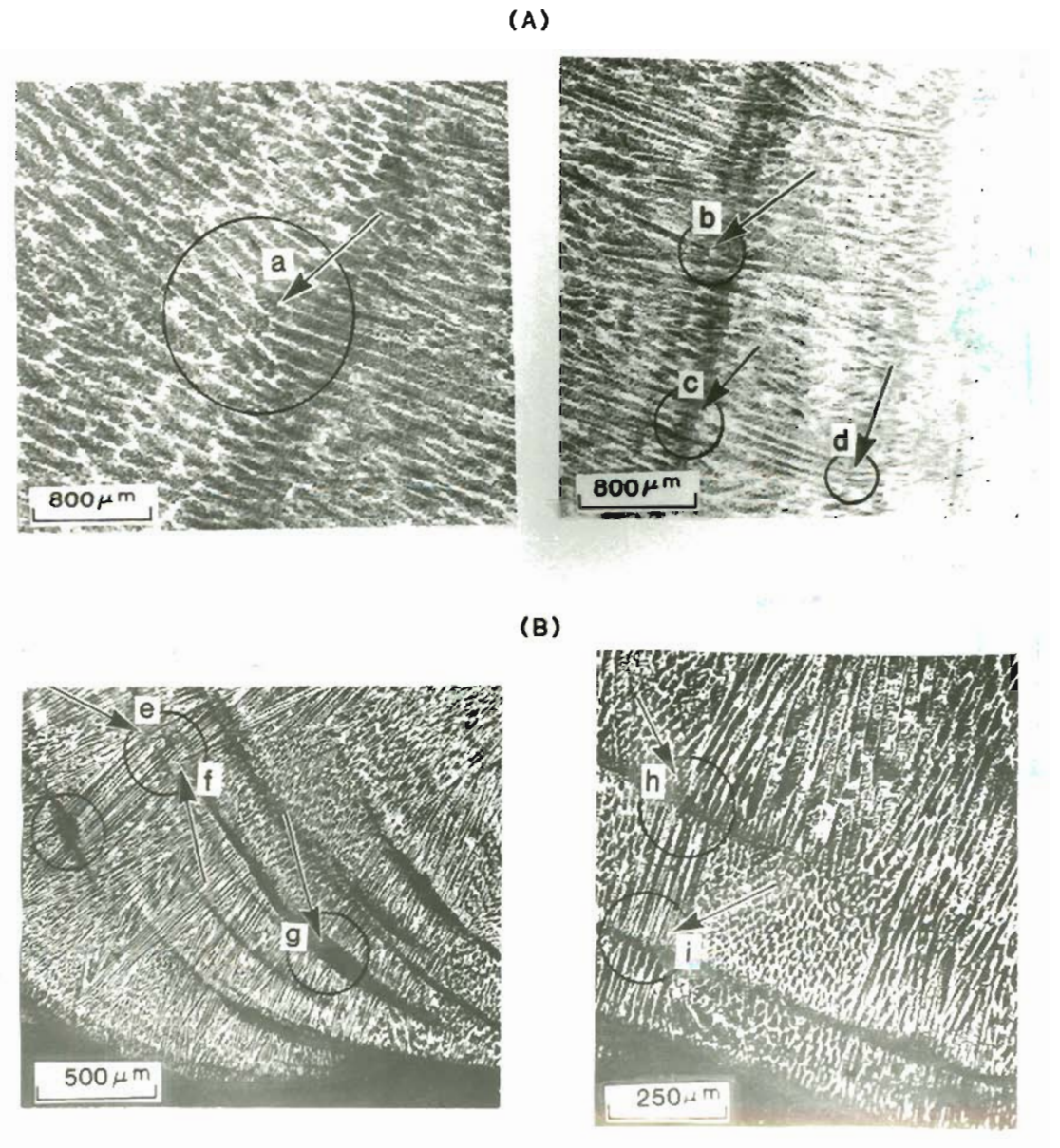

Fig. 17. Illustrations of dendrite bending and renucleation at solute bands :

(A) 17-4 PH stainless steel ES weld deposited on A36 base metal
(B) 304 stainless steel GTA weld deposited on A36 base metal

* Arrow a indicates partial dendrite arm remelting and change of dendrite morphology
b,f,g and i indicate new dendrite nucleation
c indicates direct dendrite growth
d,e and h indicate dendrite arm bending

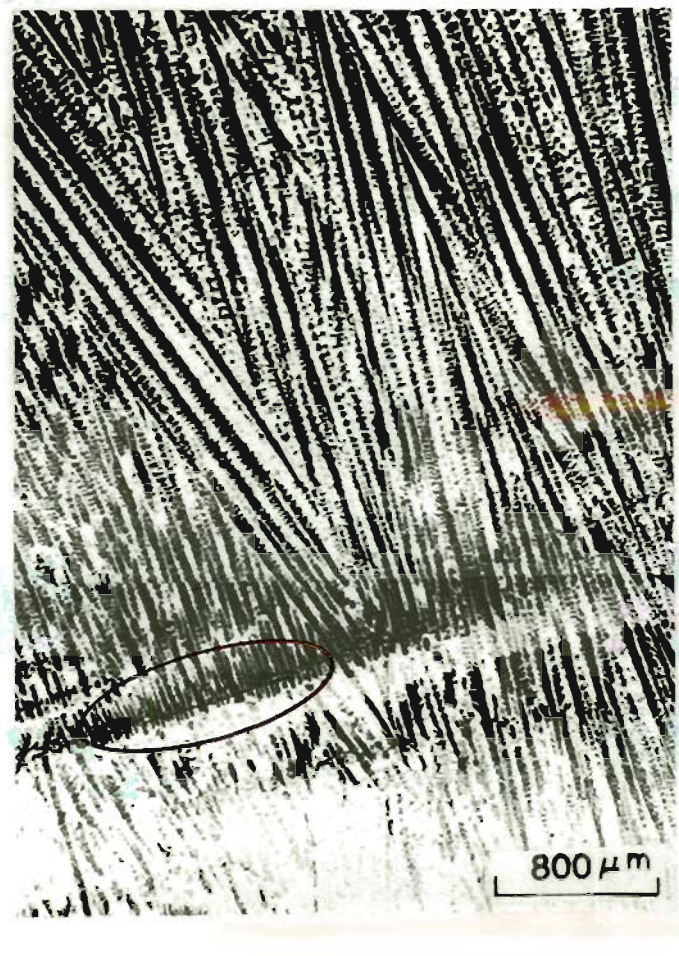

Fig. 18. Development of tertiary dendrite arms when the direction of maximum temperature gradient is different from primary dendrite gross direction in ES weld of 309 stainless steel deposited on A36 base metal

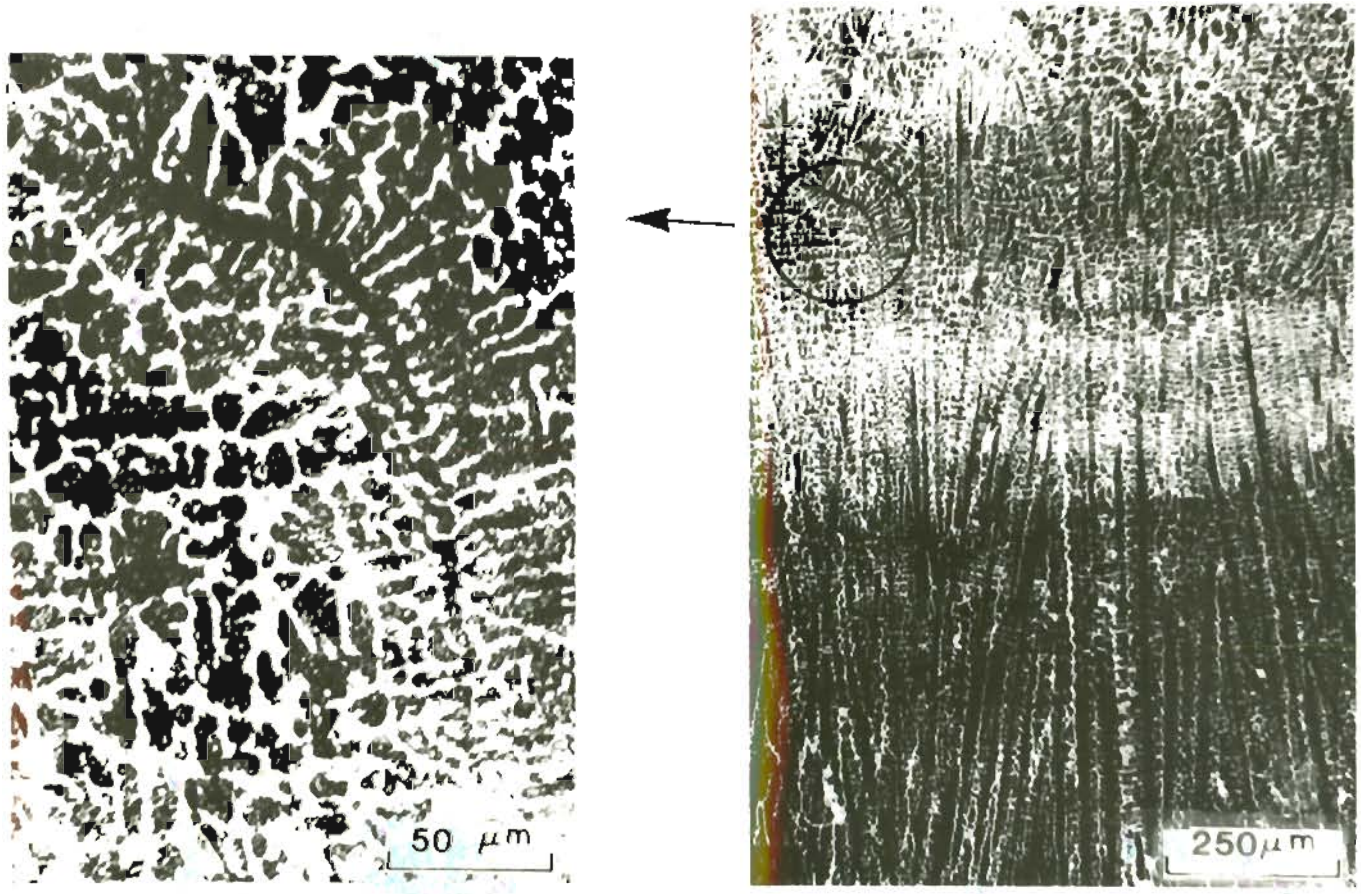

Fig. 19. Dendrite curving in 304 stainless steel GTA weld deposited on A36 base metal

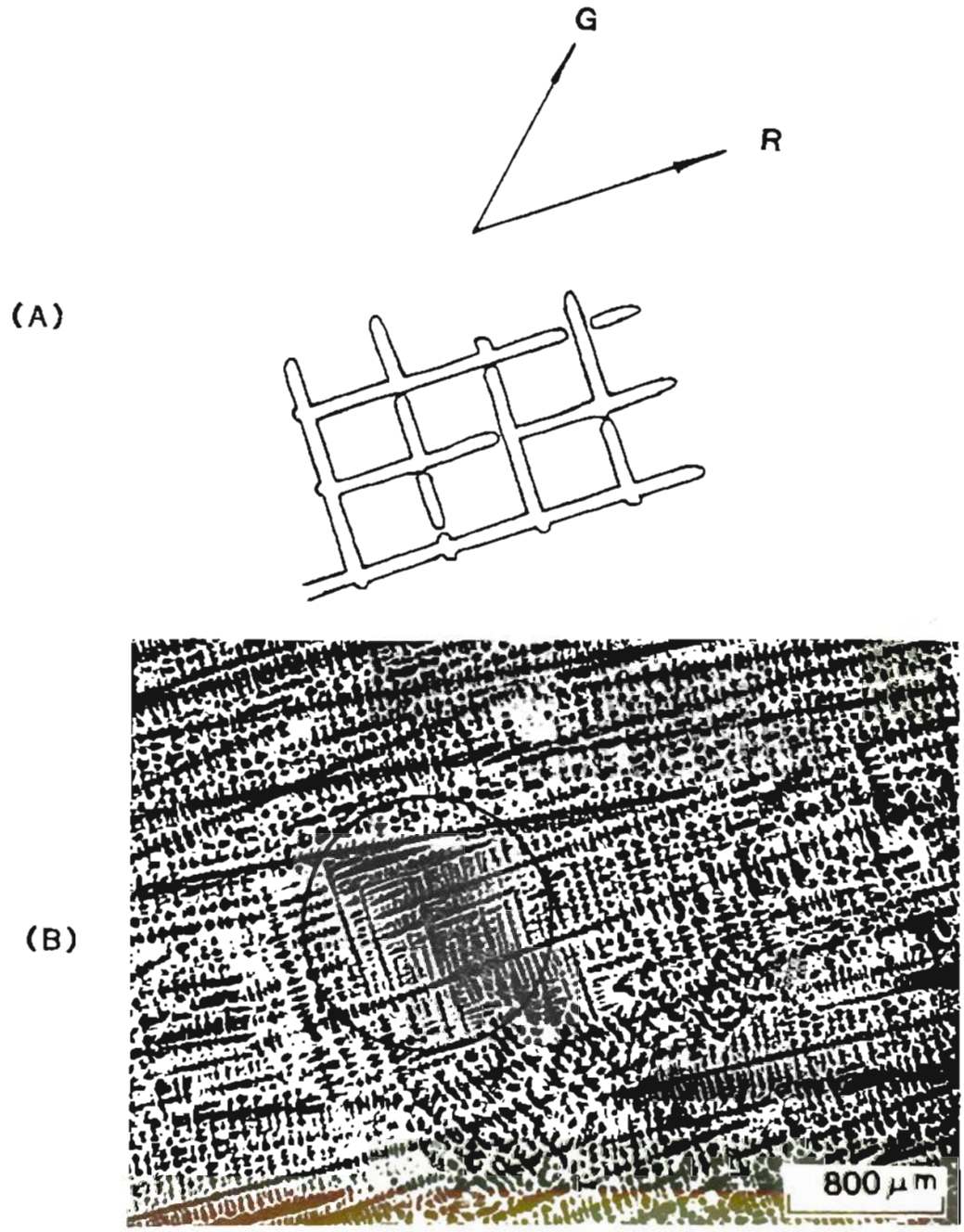

Fig. 20. Development of tertiary dendrite arms when the direction of maximum temperature gradient is different from primary dendrite growth direction in ES weld of 309 stainless steel deposited on A36 base metal (A) schematic representation and (B) solidification structure

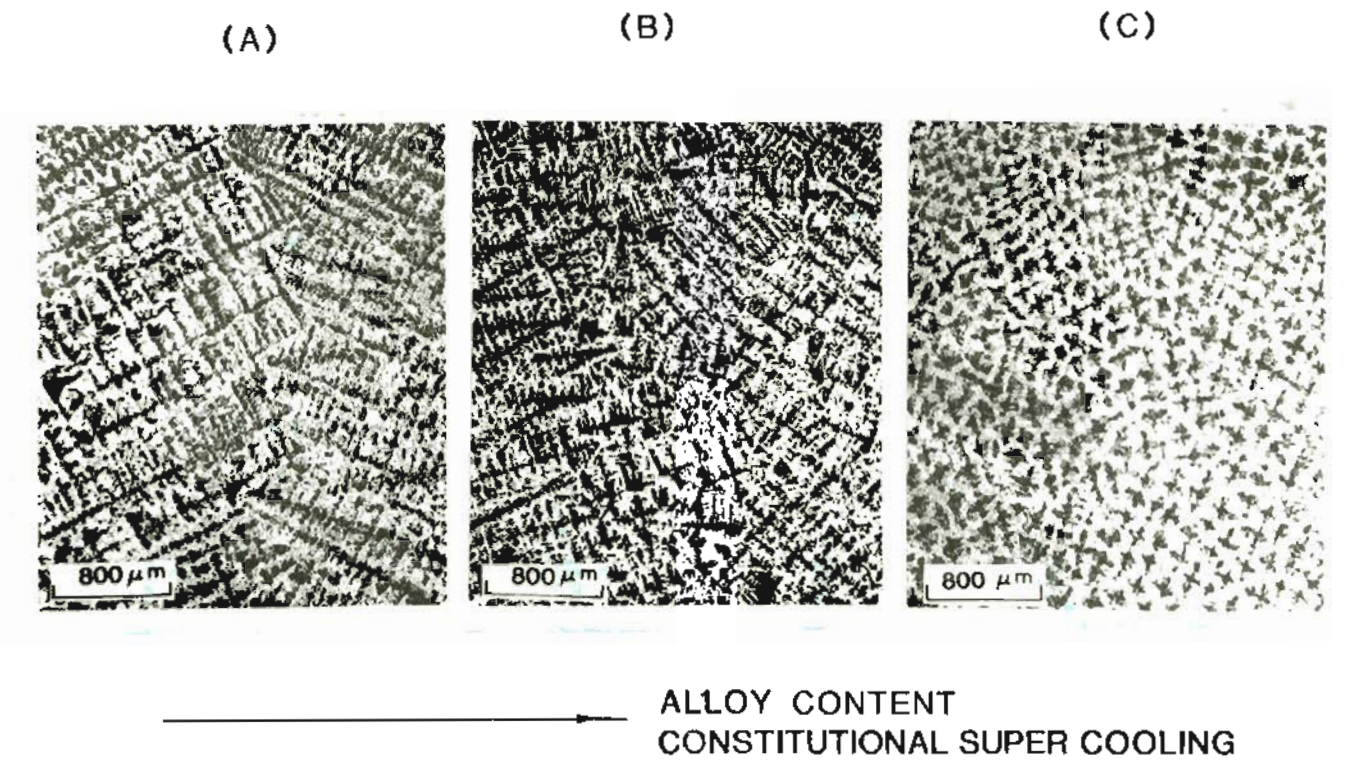

Fig. 21. Dendrite arm development at weld center line as a function of alloy content in ES welds (A) HP 25 electrode (forming a fully columnar structure) (B) PS588 electrode (partially equiaxed) (C) AX90 electrode (fully equiaxed)

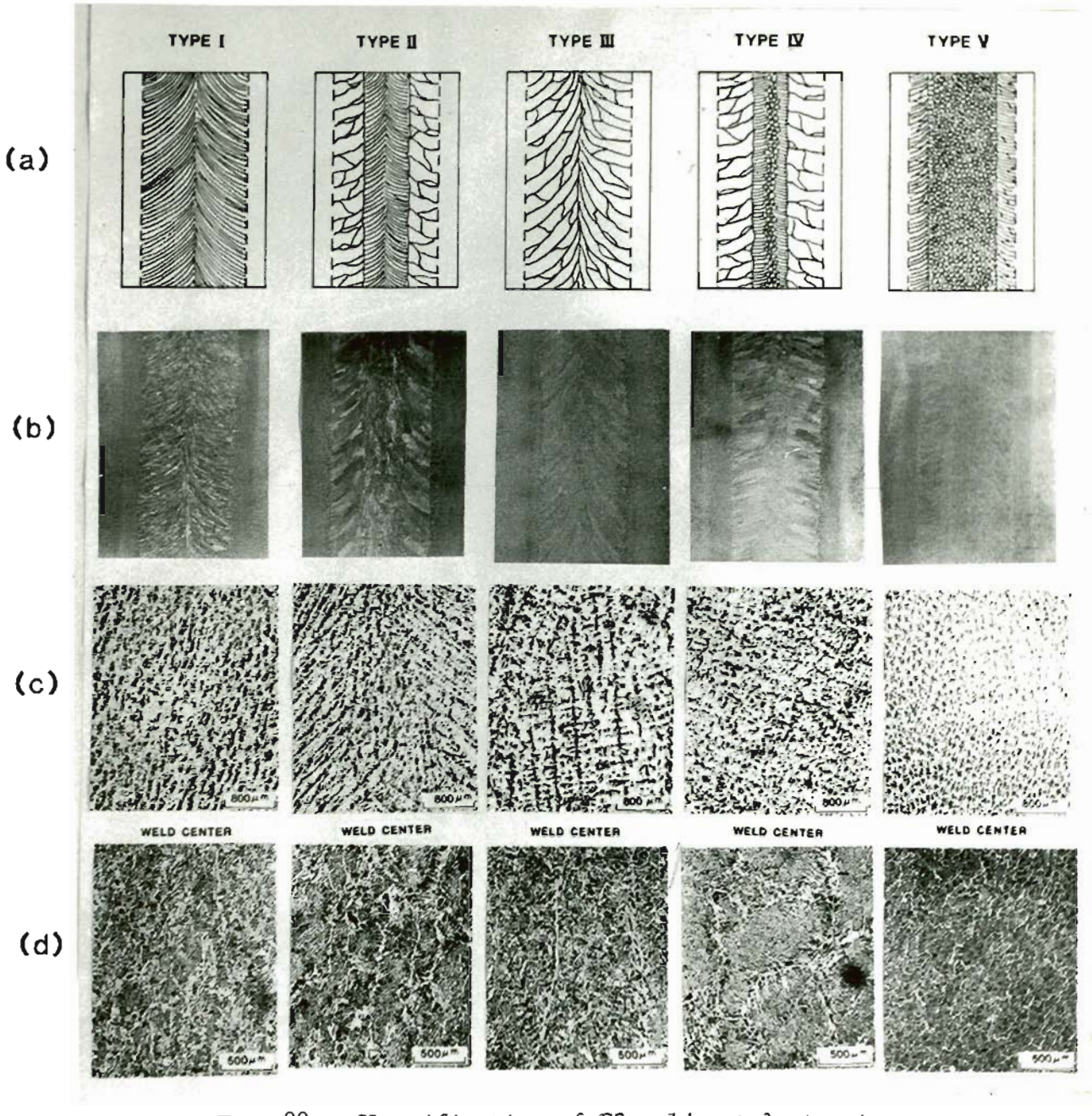

Fig. 22. Classification of ES weld metal structures

(a) schematic sketch of macrostructures
(b) macrostructures
(c) dendrite structures
(d) solid-state microstructures

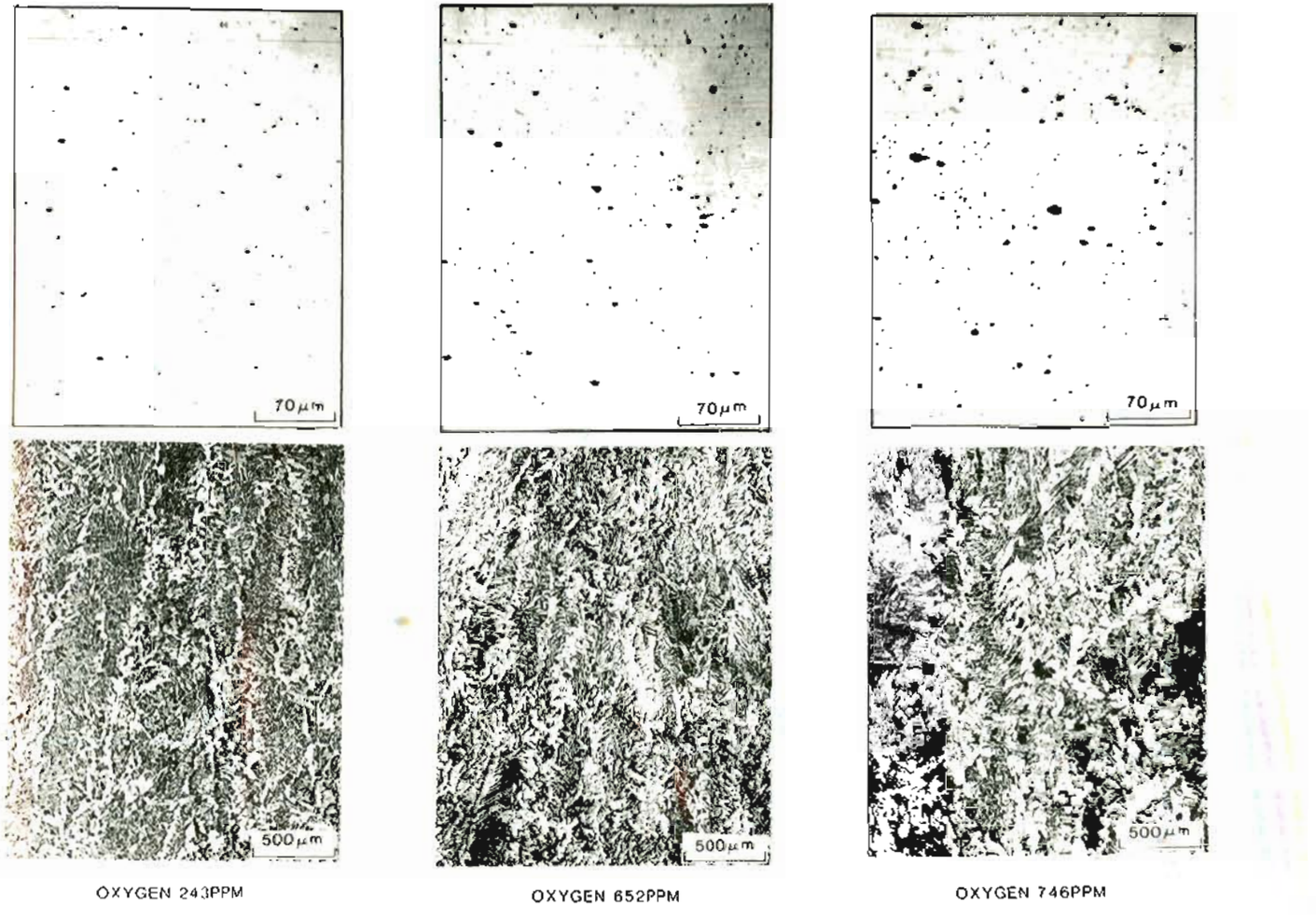

Fig. 23. Inclusion distribution as a function of oxygen potential and oxygen content

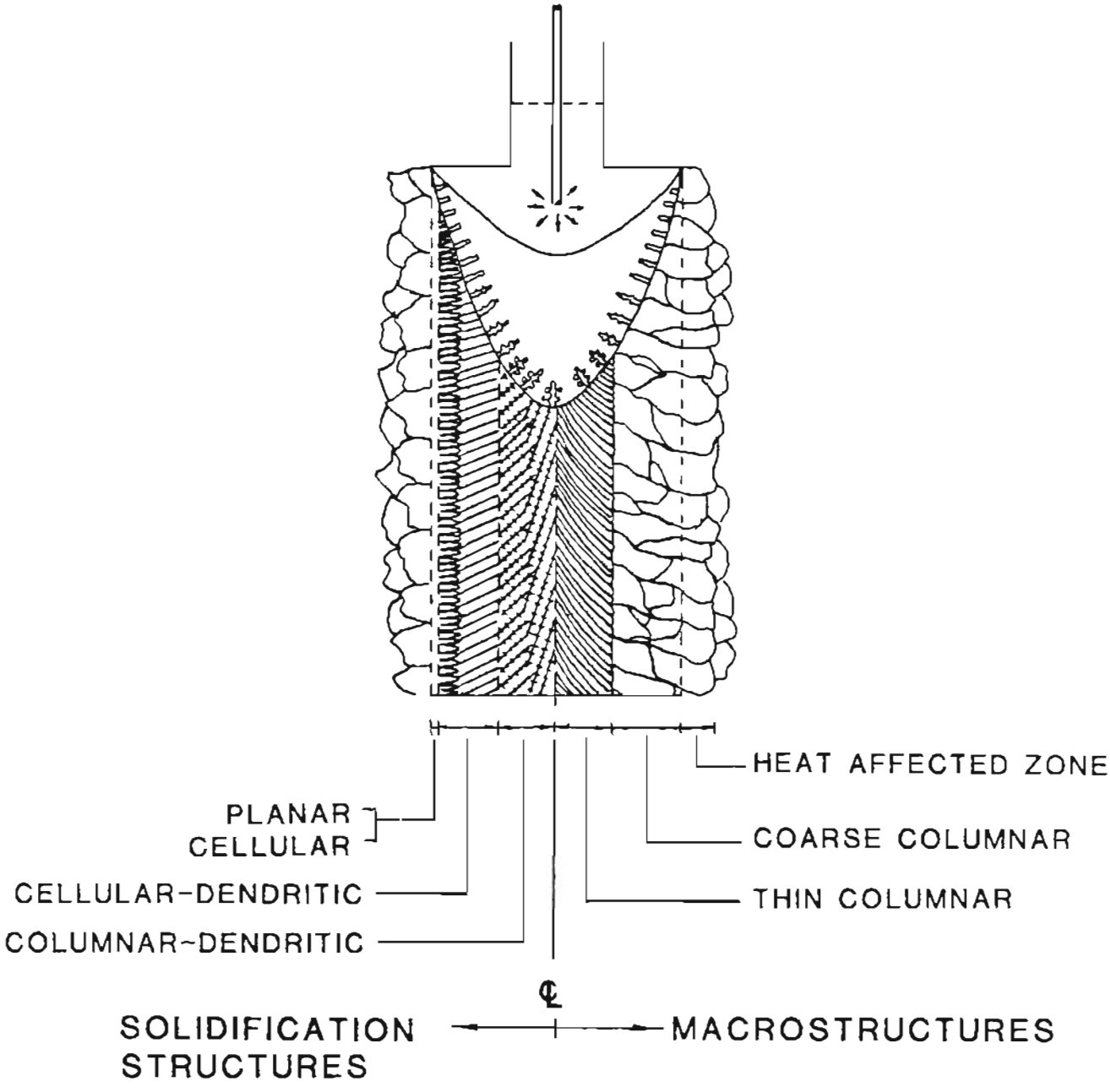

Fig. 24. Relationship between weld metal solidification structure and subsequent solid state structure

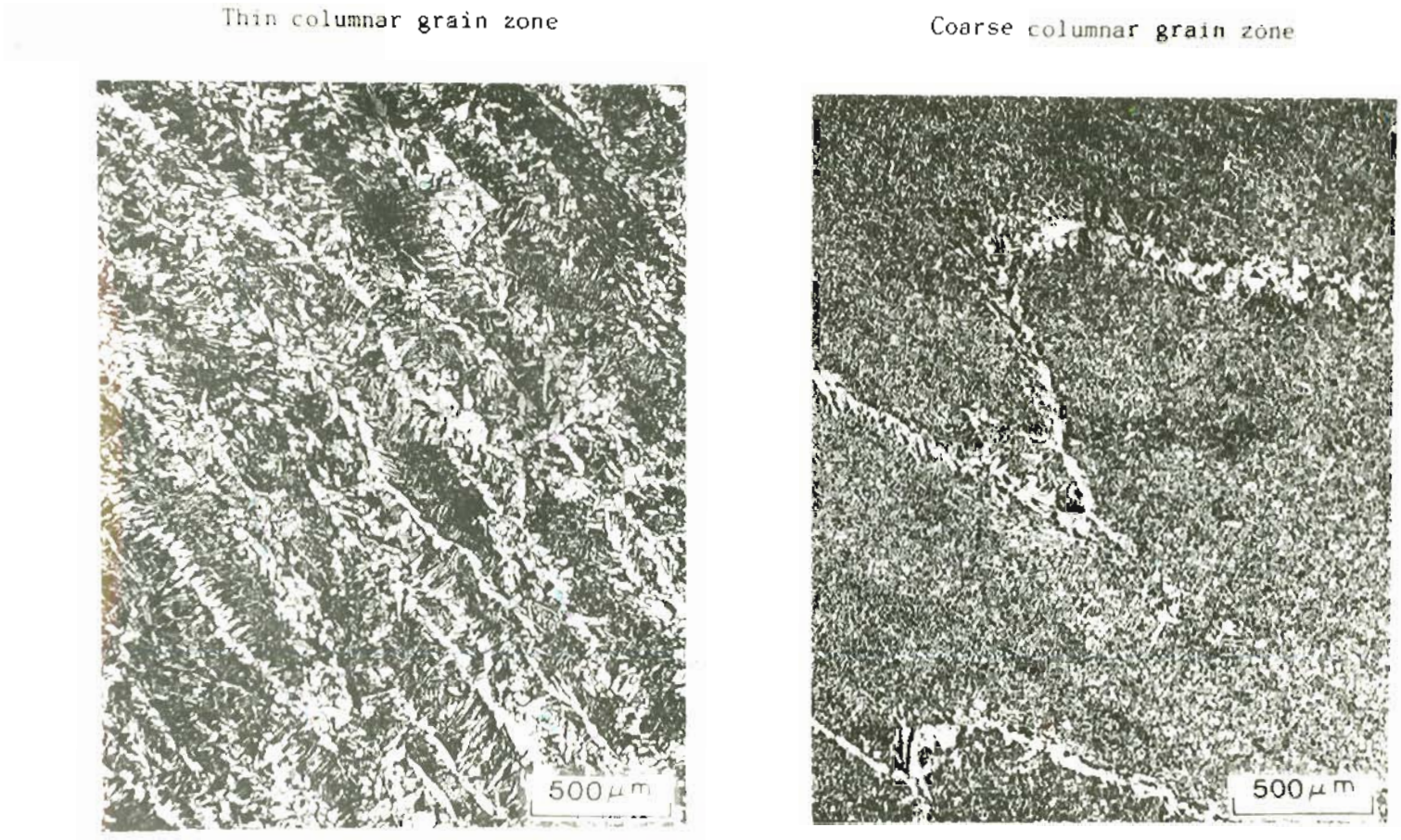

Fig. 25. Typical thin columnar grain and coarse columnar grain microstructures

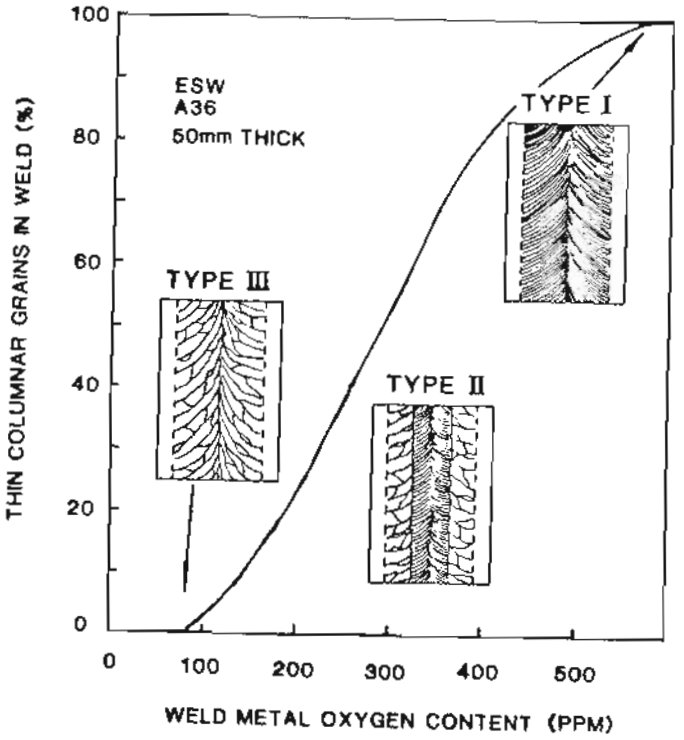

Fig. 26. Macrostructure as affected by weld metal oxygen content

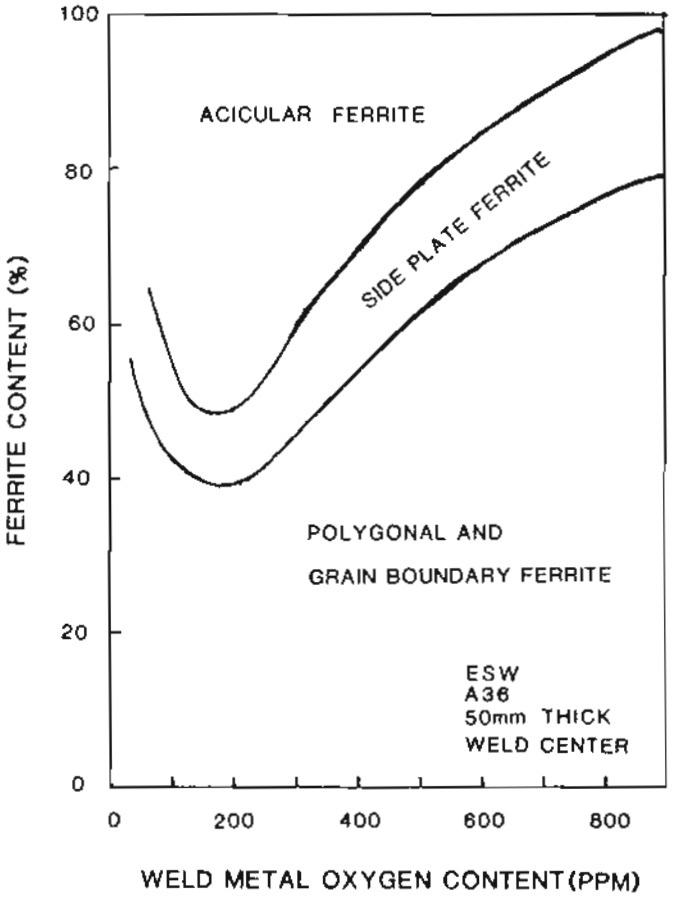

Fig. 27. Ferrite content at weld center as a function of weld metal oxygen content

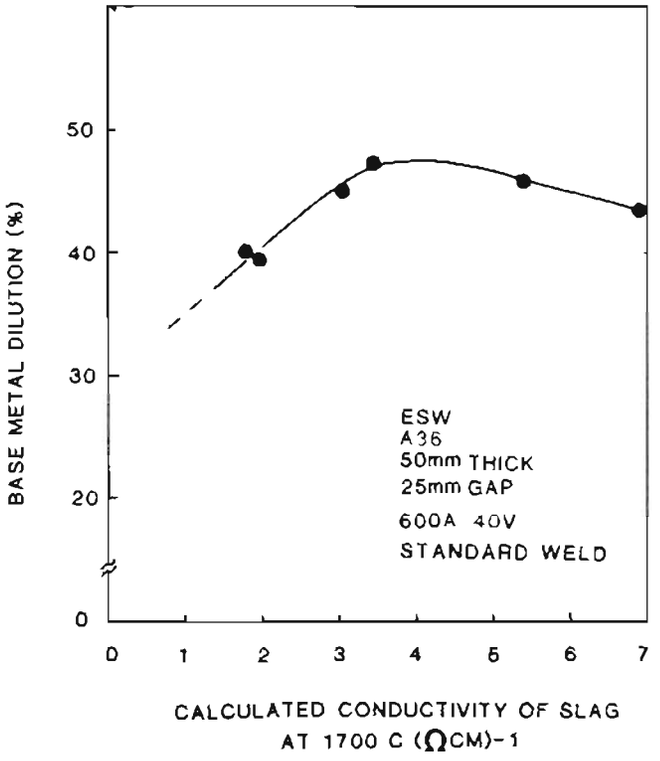

Fig. 28. Relationship between slag conductivity and base metal dilution

Fig. 29. SEM micrograph showing dendrite structures

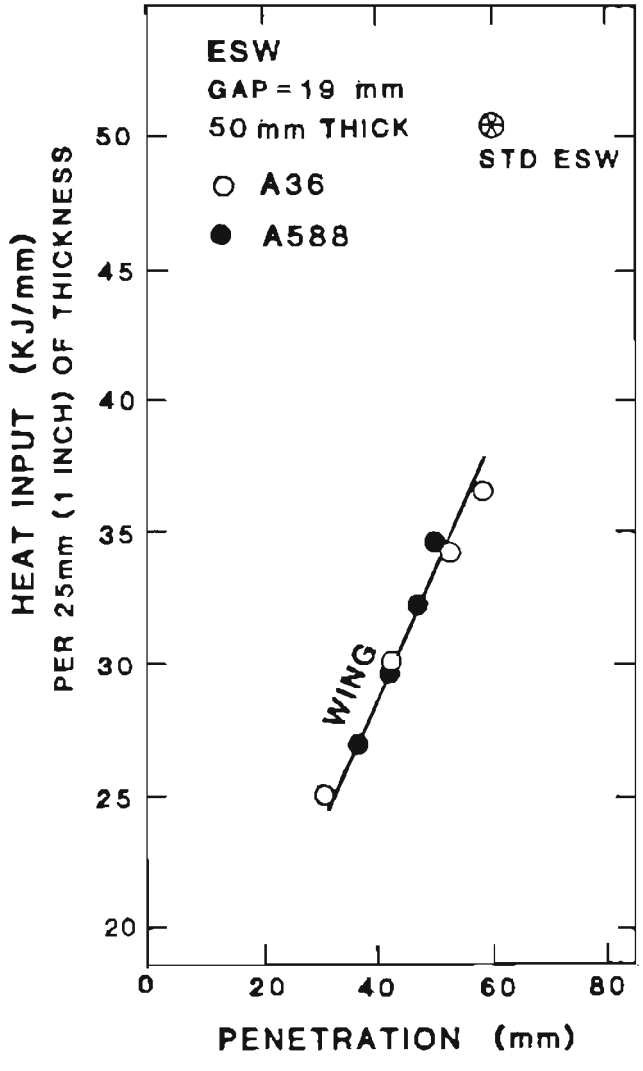

Fig. 30. Effect of heat input on base metal penetration

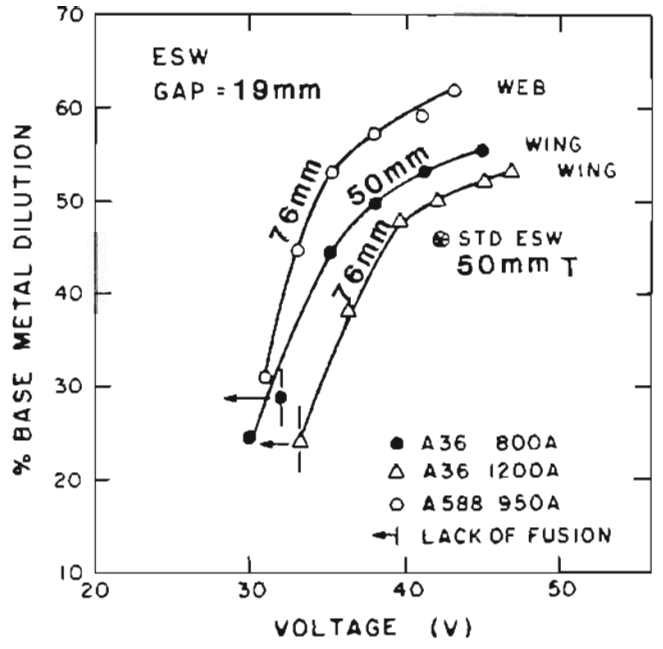

Fig. 31. Influence of voltage on base metal dilution

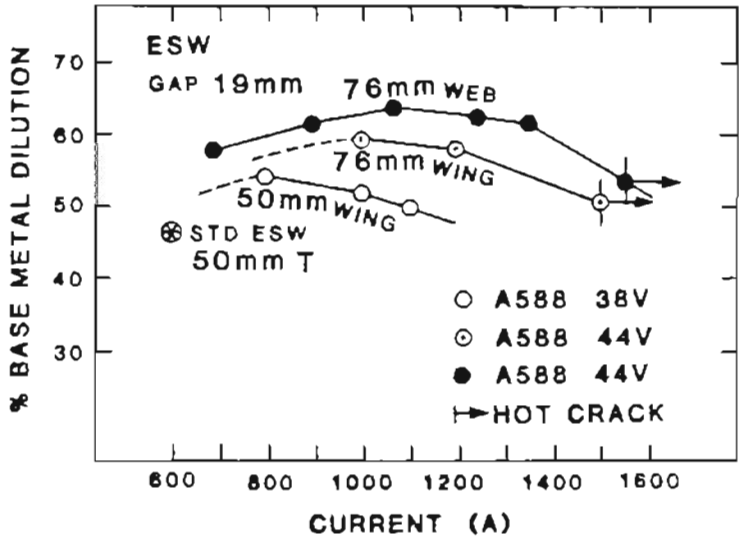

Fig. 32. Influence of current on base metal dilution

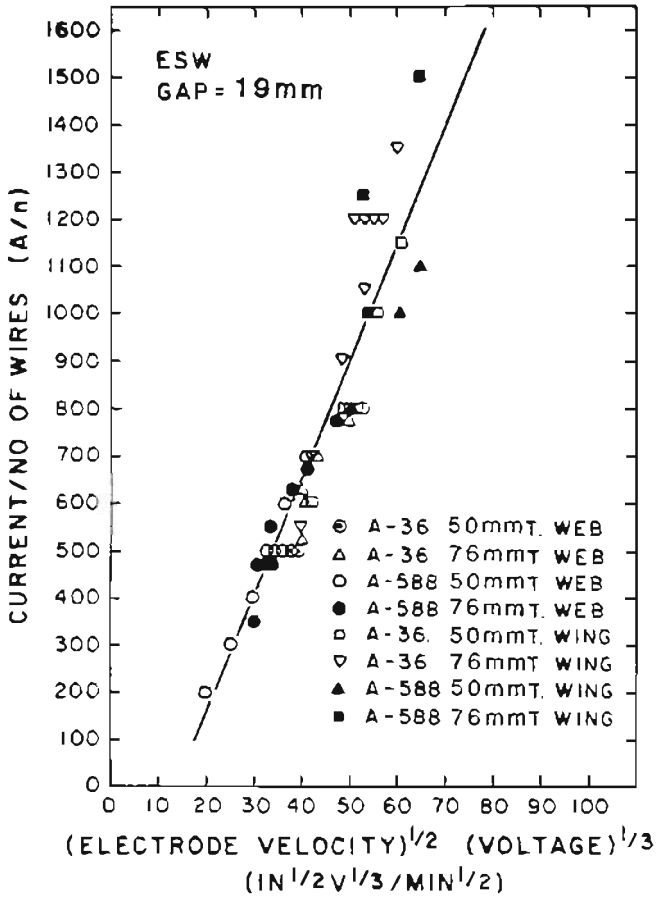

Fig. 33. Relationship between welding current and electrode velocity and welding voltage

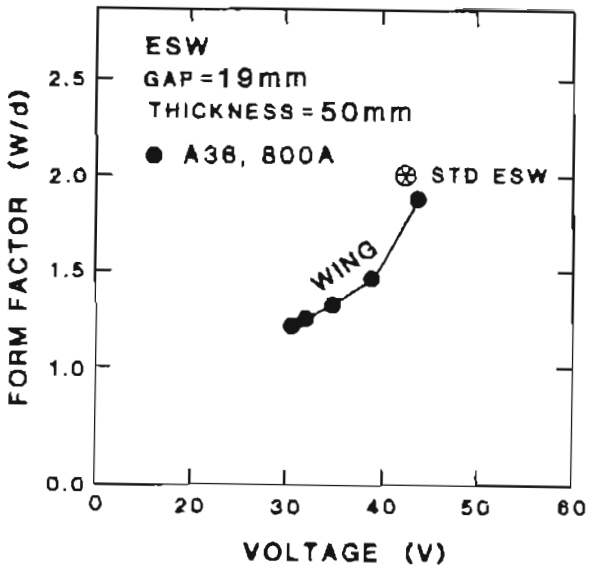

Fig. 34. Form factor as a function of voltage

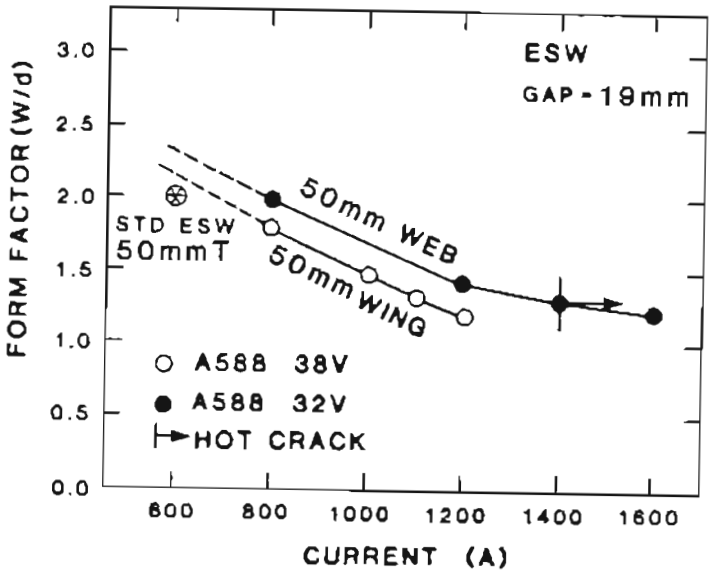

Fig. 35. Form factor as a function of current

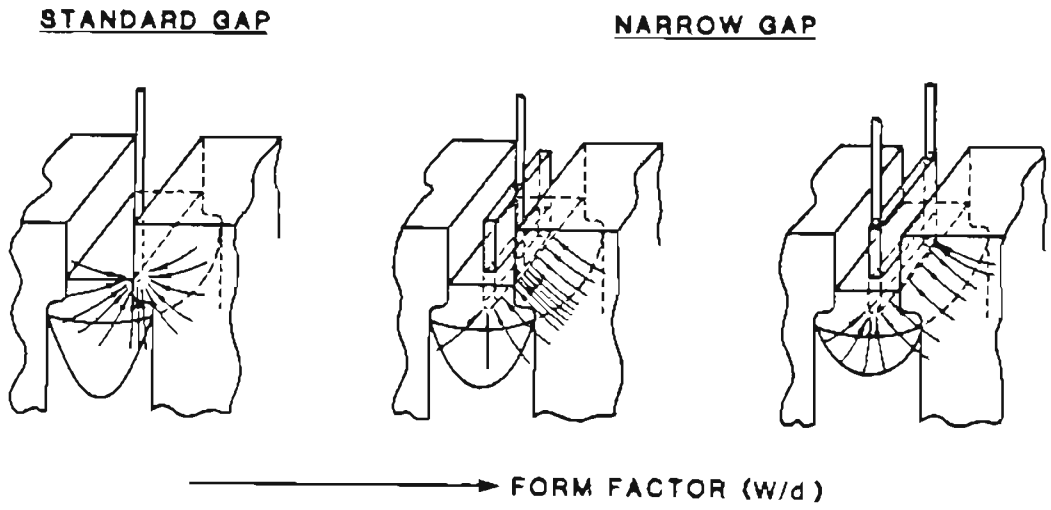

Fig. 36. Heat, current density and impurity distributions comparison between standard weld and narrow gap welds

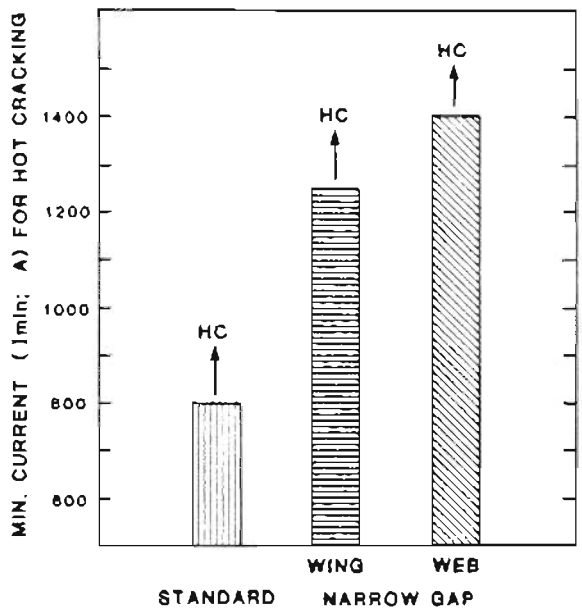

Fig. 37. Hot crack resistance between standard and narrow gap welds

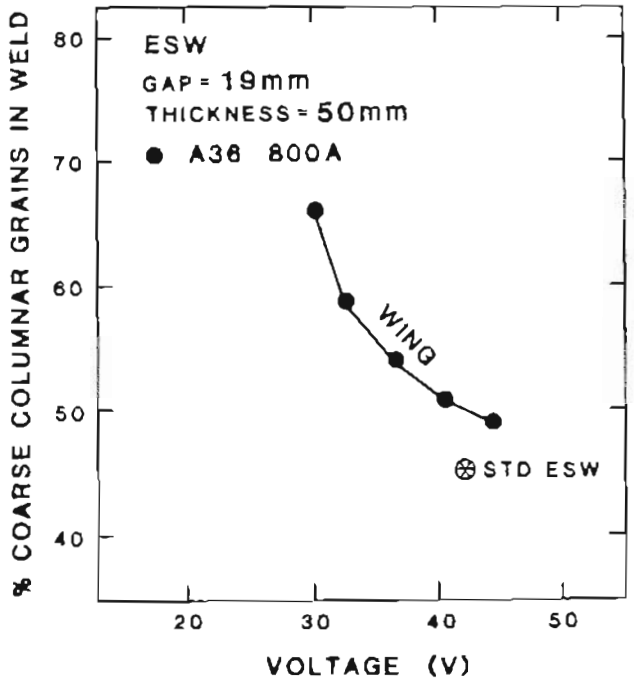

Fig. 38. Influence of voltage on the coarse columnar grain zone

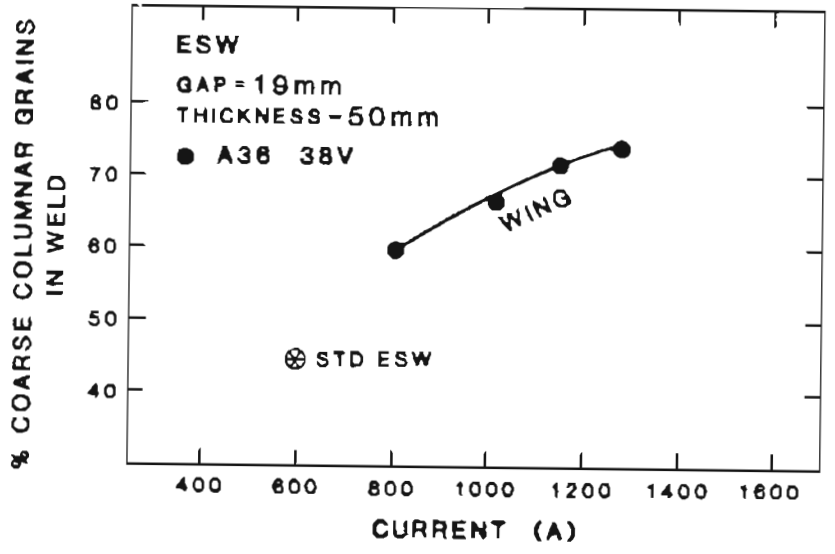

Fig. 39. Influence of current on the coarse columnar grain zone

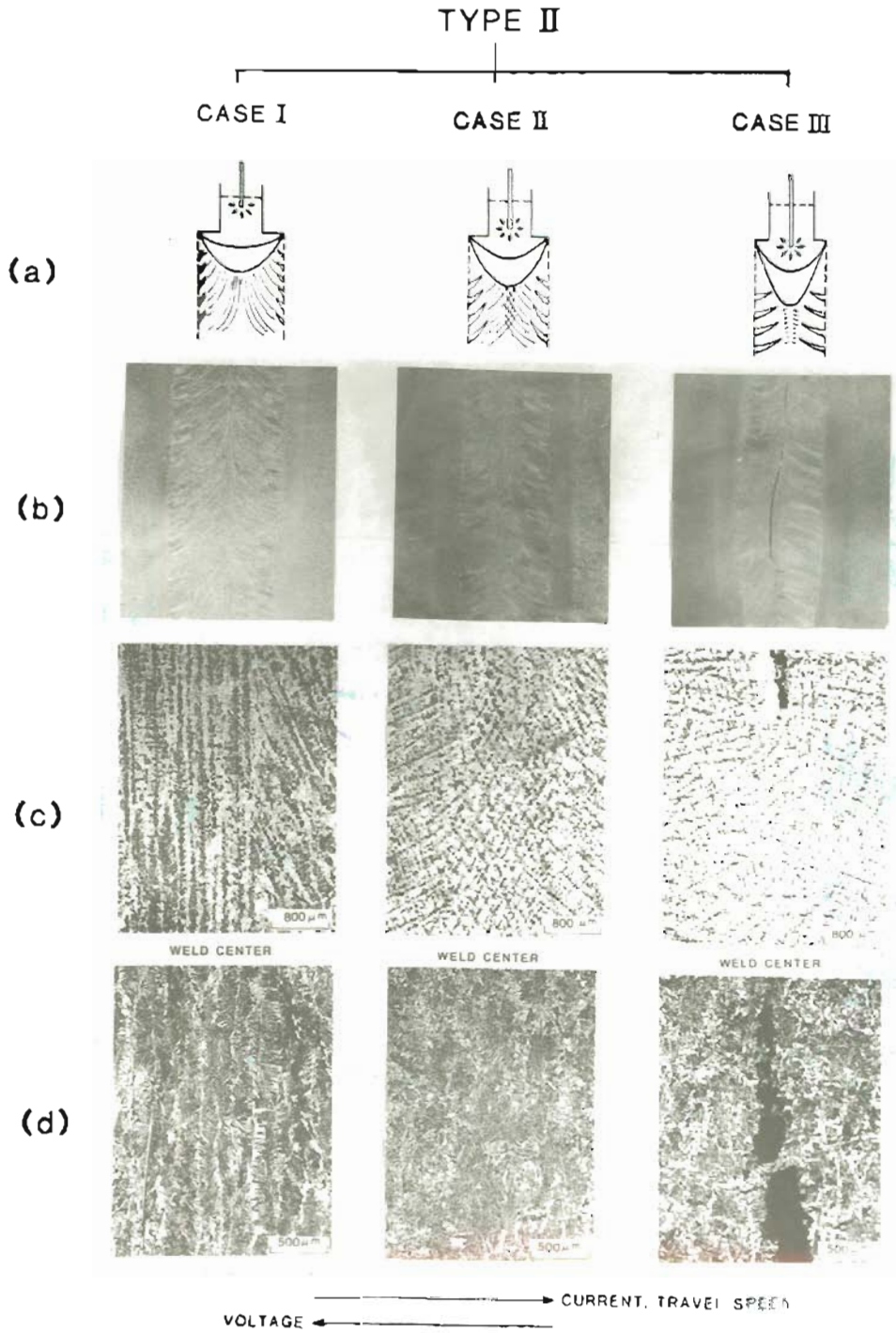

Fig. 40. Three characteristic cases of grain structure in narrow gap ES welds

(a) molten pool shape
(b) macrostructures
(c) dendrite structures
(d) solid state microstructures

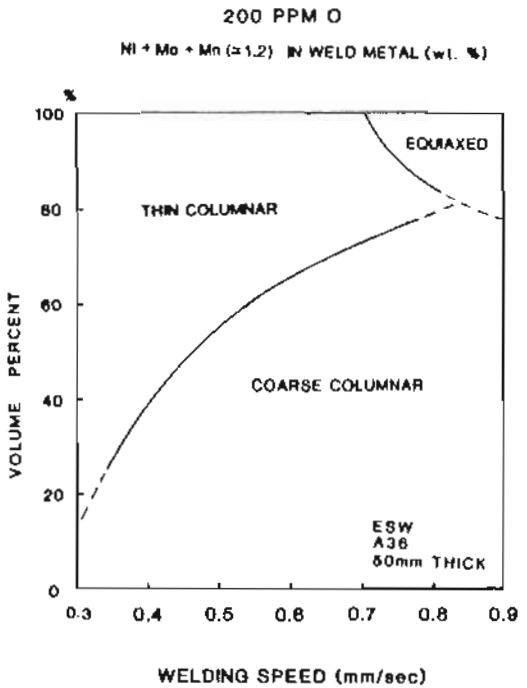

Fig. 41. Effect of welding speed on the volume percent of coarse columnar, thin columnar and equiaxed zones in weld metal

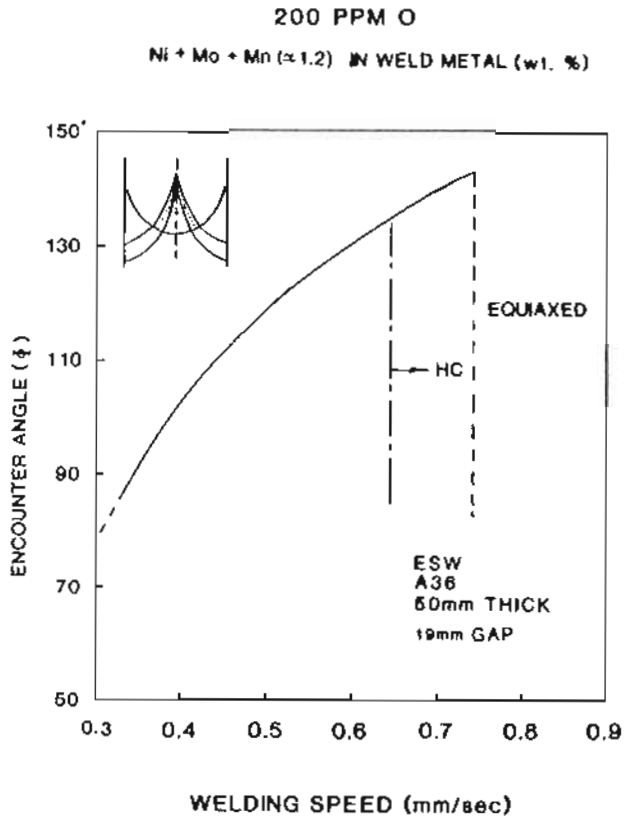

Fig. 42. Effect of welding speed on the encounter angle, hot crack and equiaxed grains formation

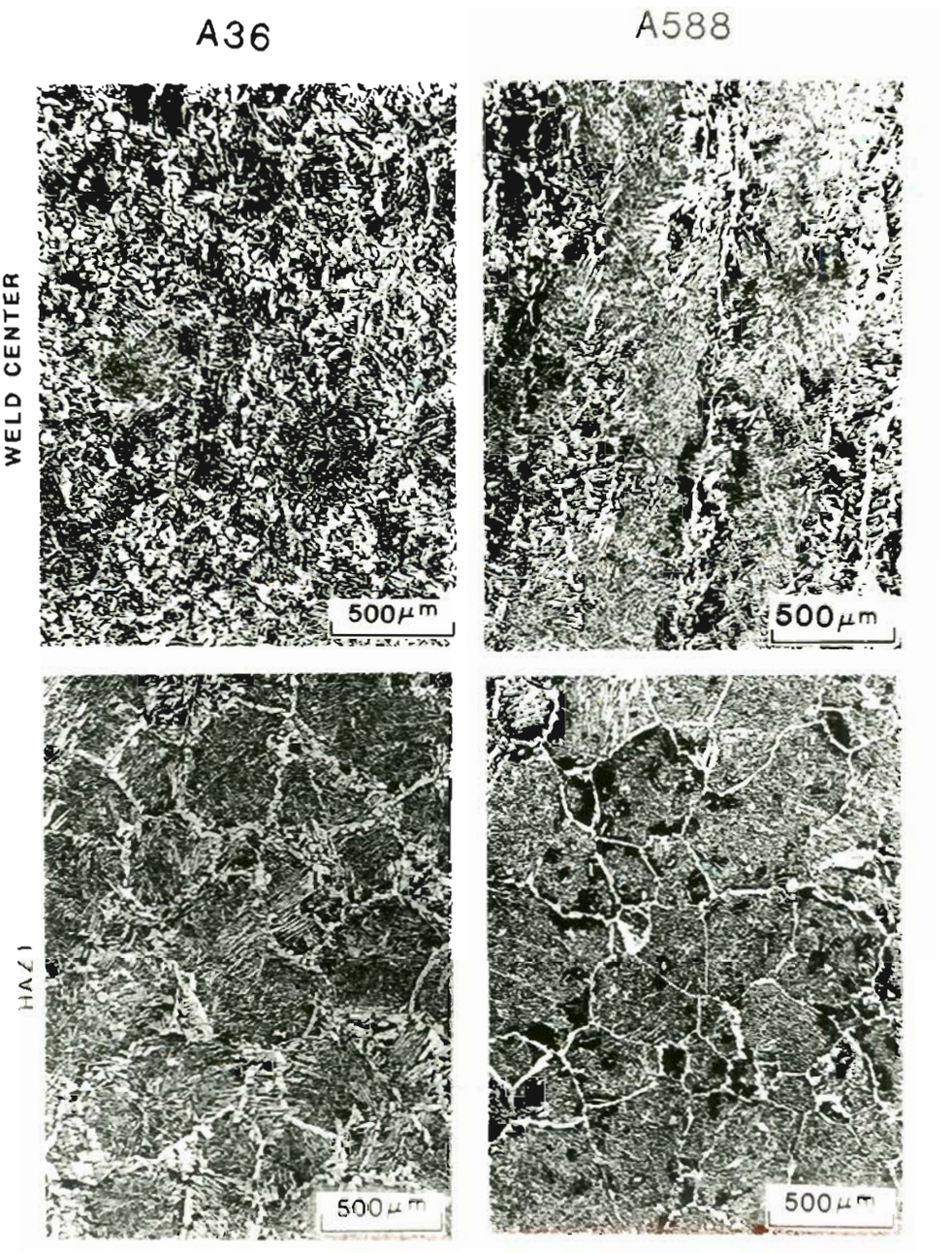

Fig. 43. Typical microstructures at weld center and HAZ 1 of optimized weld between A36 and A588

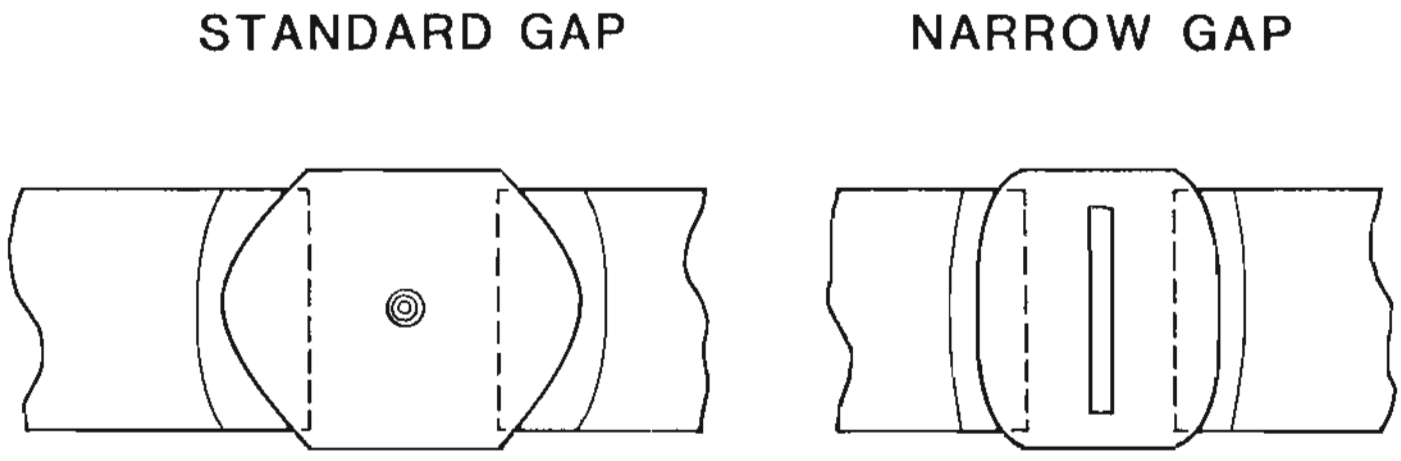

Fig. 44. Schematic sketch of base metal penetration, dilution and HAZ size between standard weld and narrow gap weld

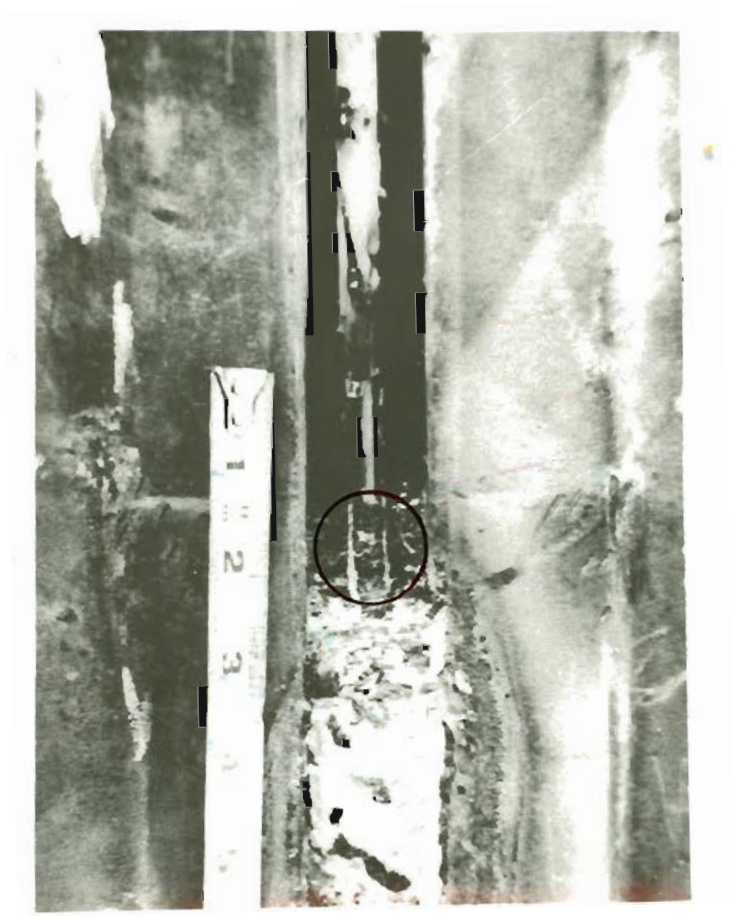

Fig. 45. Quartz penetration into the slag pool in quartz grain refined welding

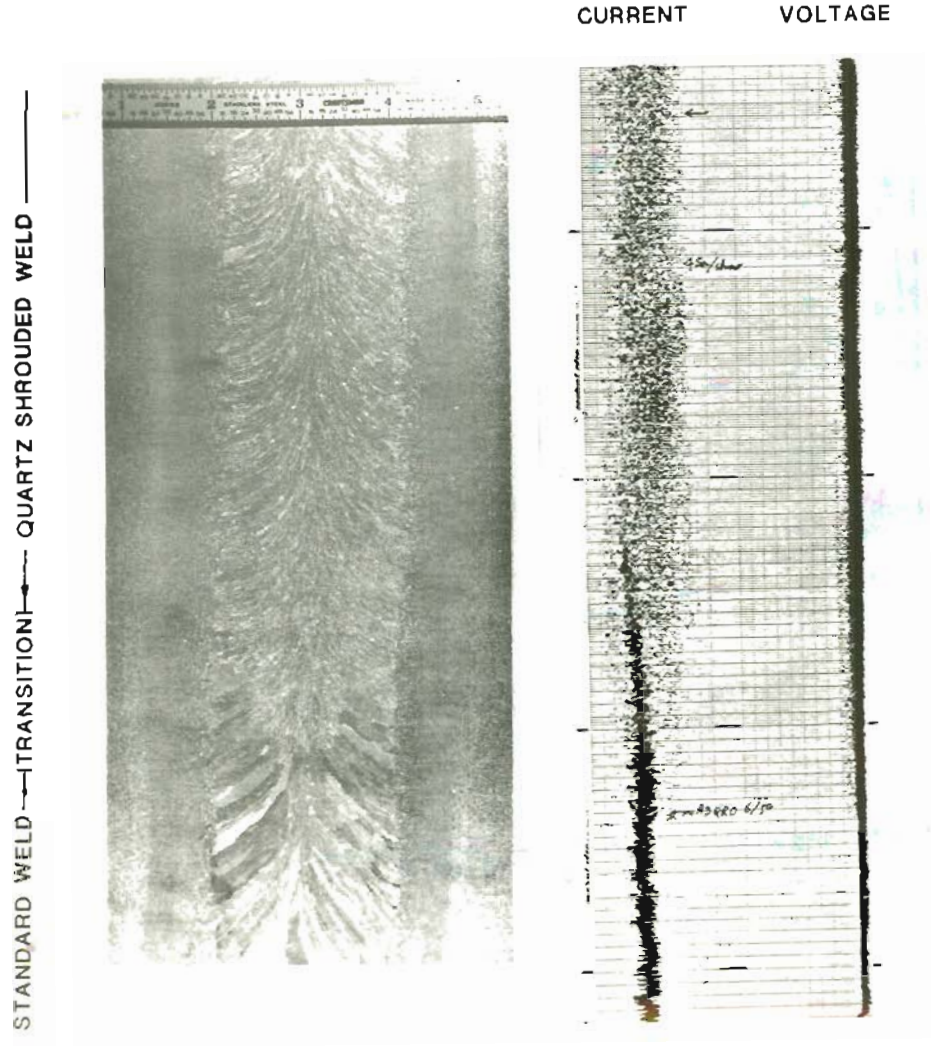

Fig. 46. Grain refinement and current and voltage fluctuations in quartz grain refined welding

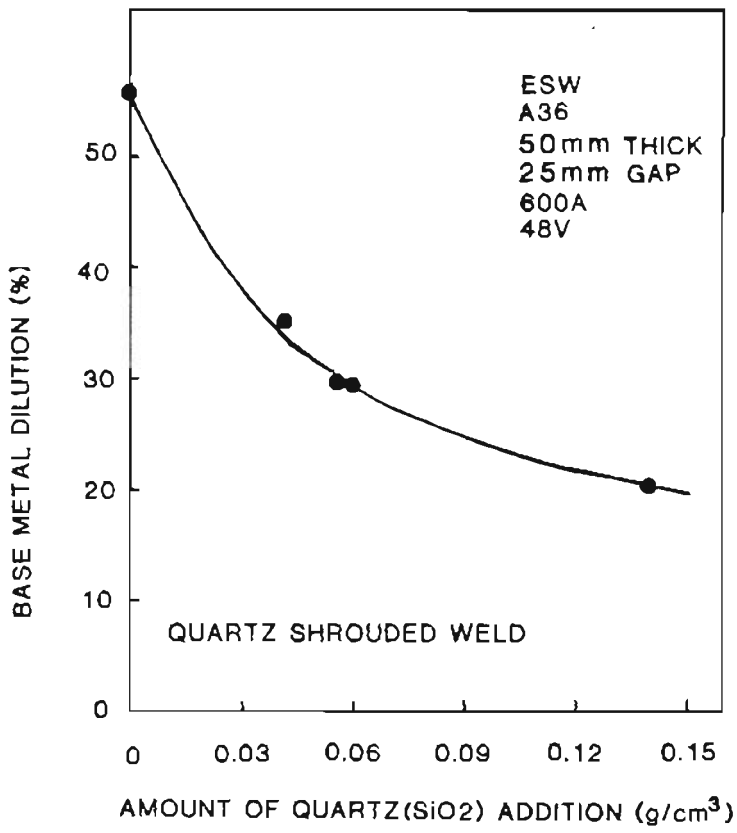

Fig. 47. Base metal dilution as a function of amount of quartz addition during quartz grain refined welding

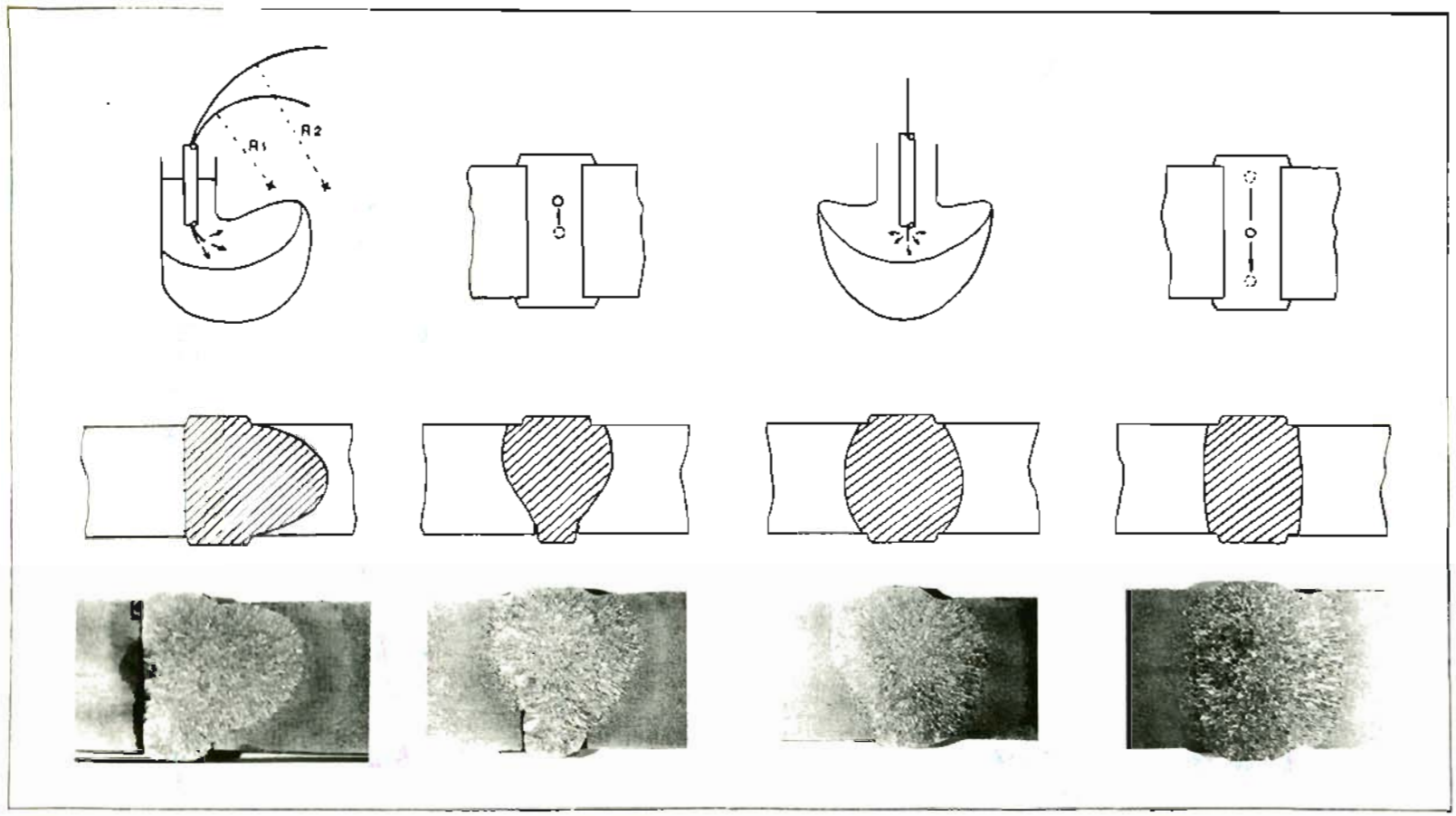

Fig. 48. Influence of electrode misalignment and asymmetrical heat generation during quartz welding

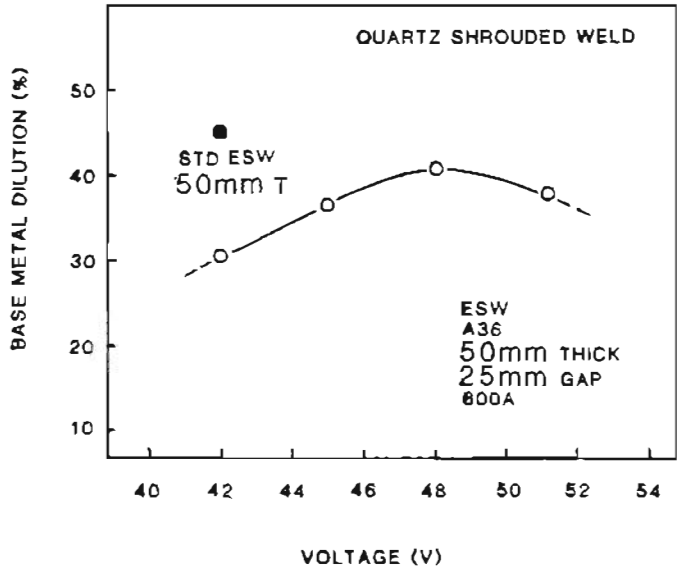

Fig. 49. Effect of voltage on the base metal dilution during quartz welding

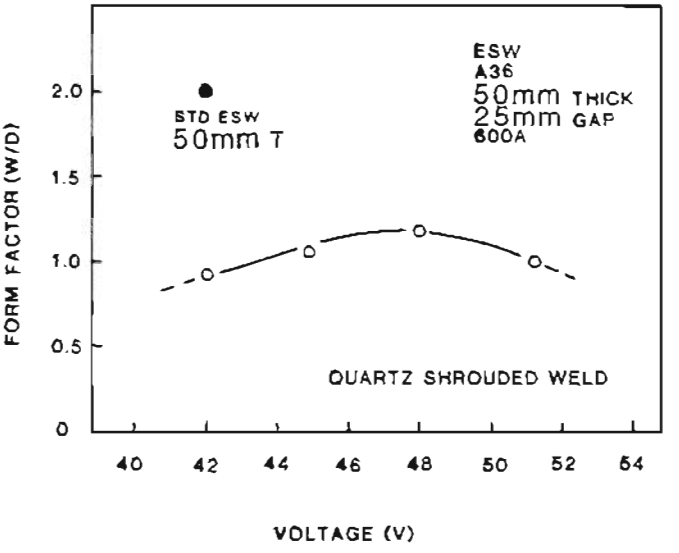

Fig. 50. Effect of voltage on the form factor during quartz welding

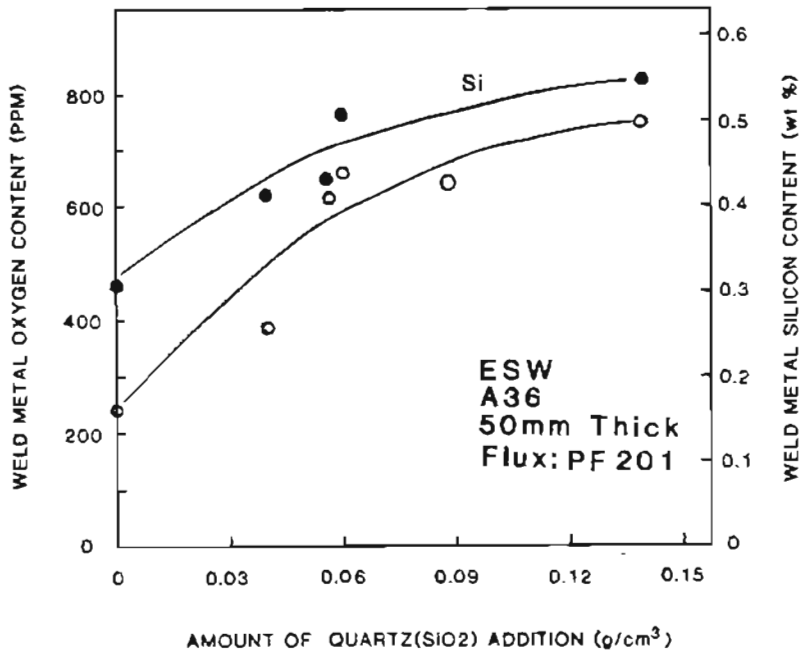

Fig. 51. Influence of amount of quartz addition on the weld metal oxygen and silicon content during quartz welding

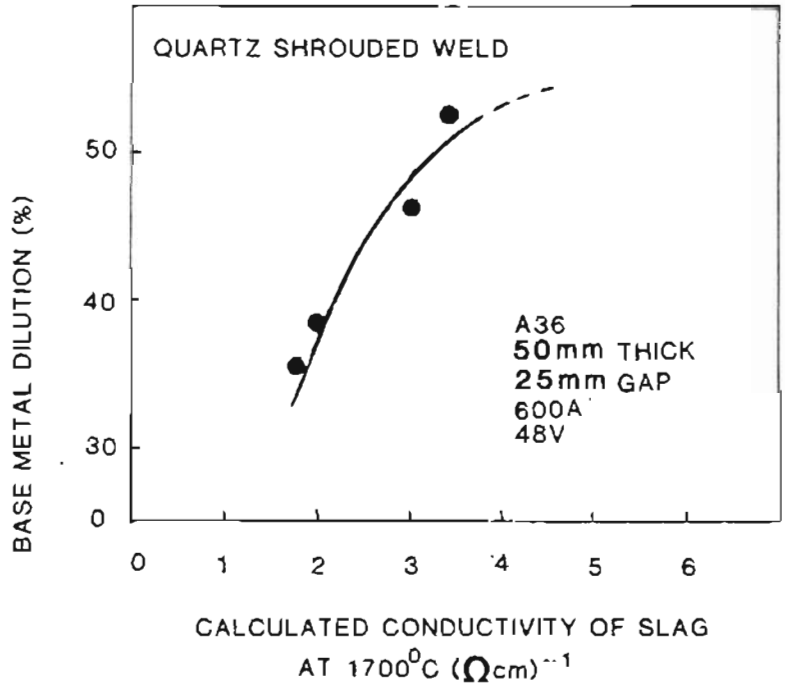

Fig. 52. Base metal dilution as a function of slag conductivity

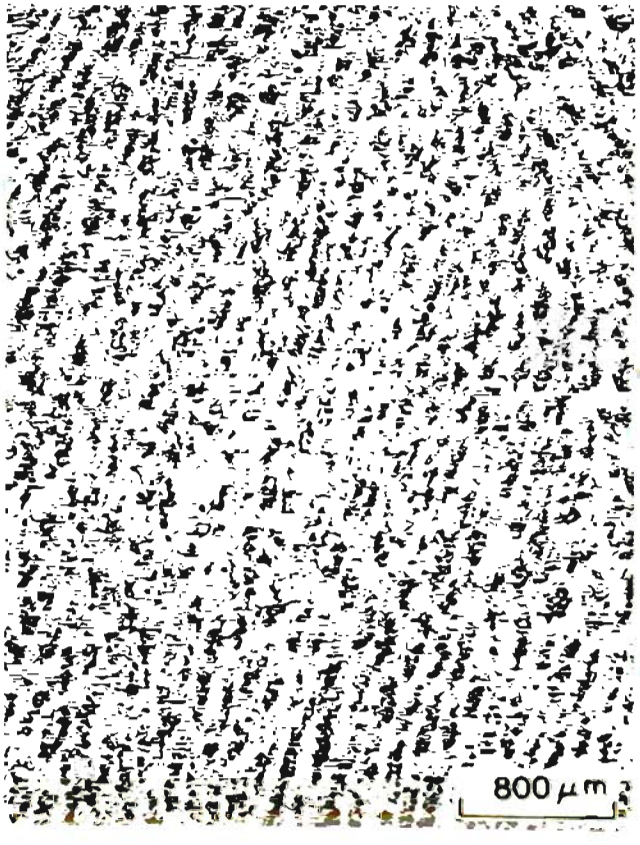

Fig. 53. Fragmented dendrites due to intense molten pool stirring during quartz grain refined ESW

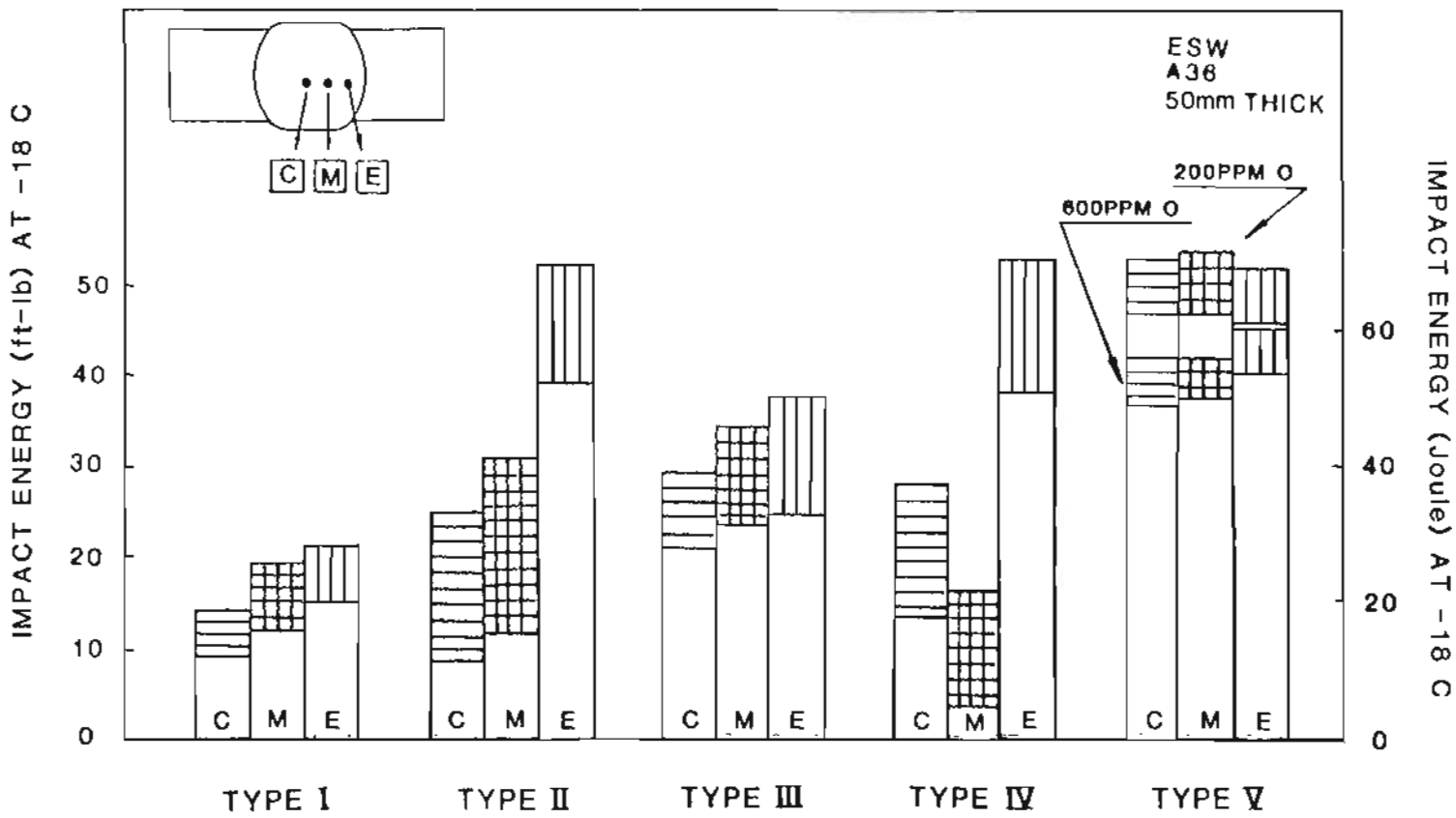

Fig. 54. CVN toughness of each type of weld structures

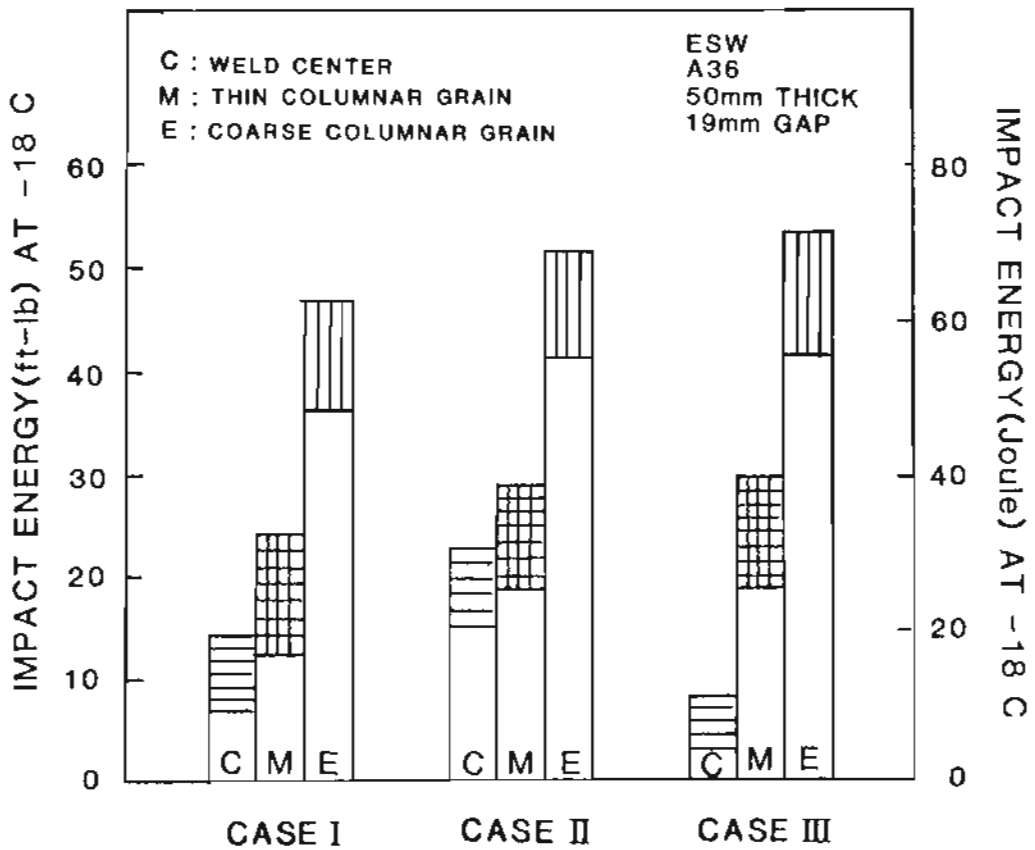

Fig. 55. CVN toughness of each case of weld structures in narrow gap ES welds

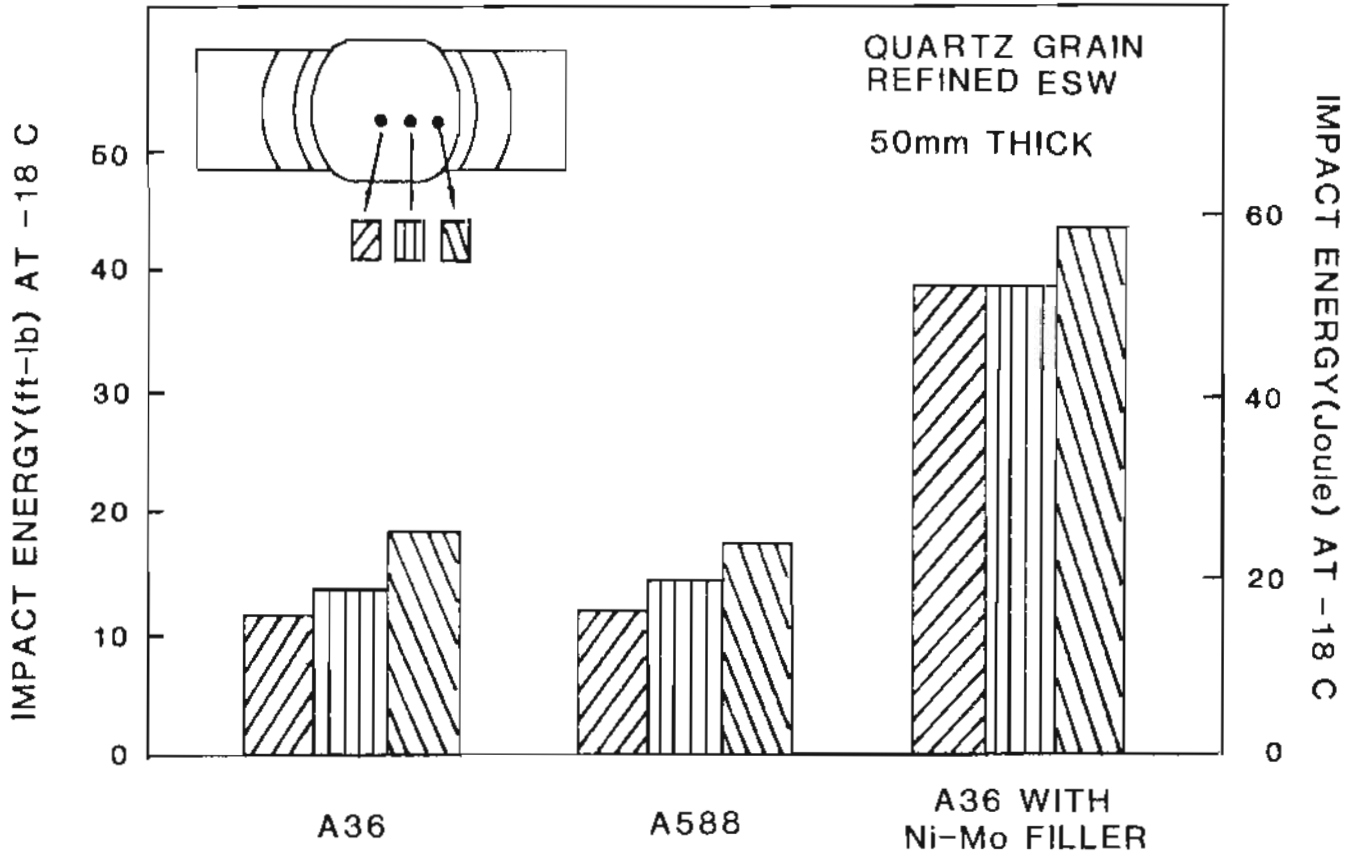

Fig. 56. CVN toughness for quartz grain refined plus the influence of alloy additions

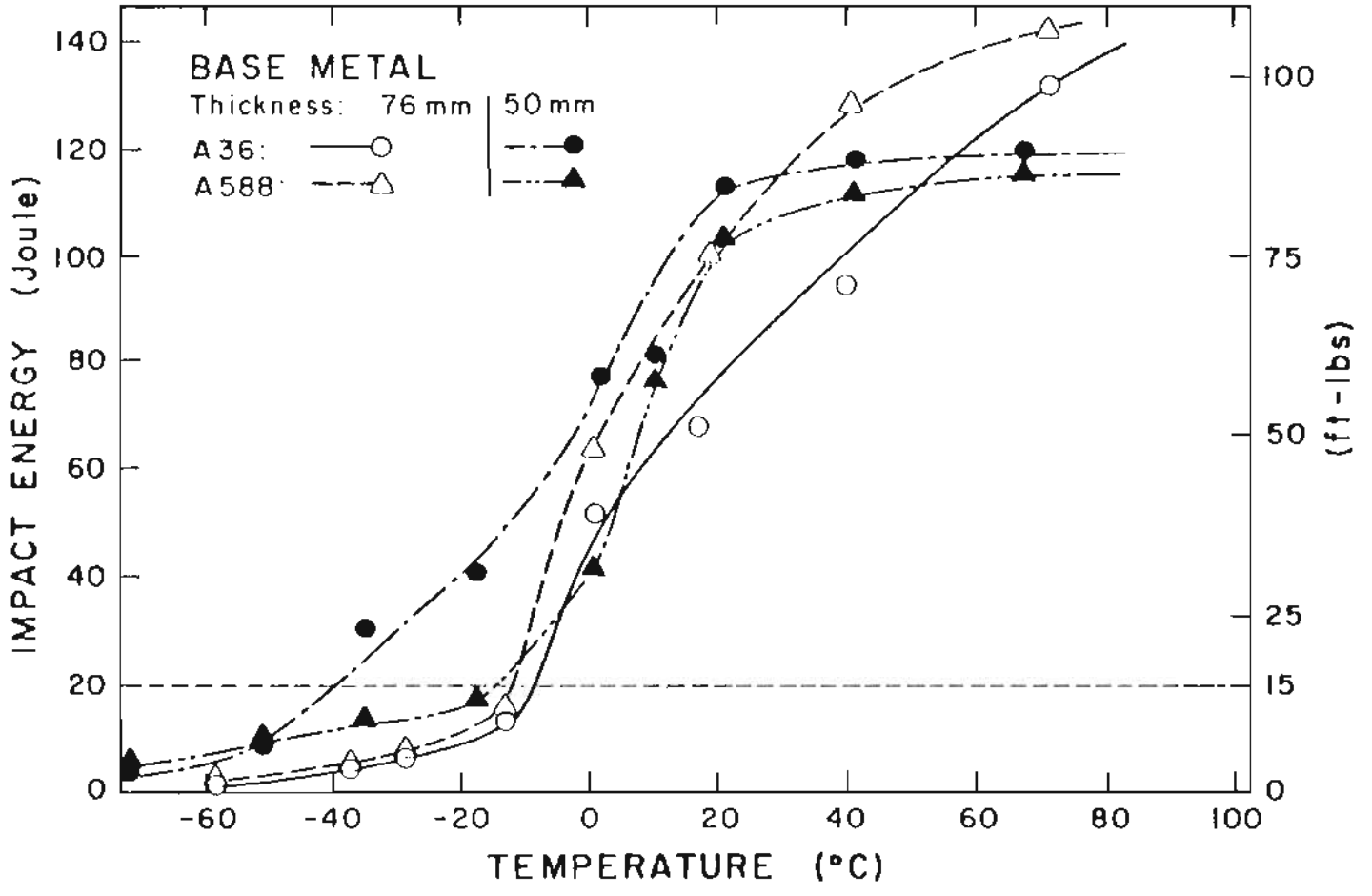

Fig. 57. CVN transition curves for A36 and A588 base material

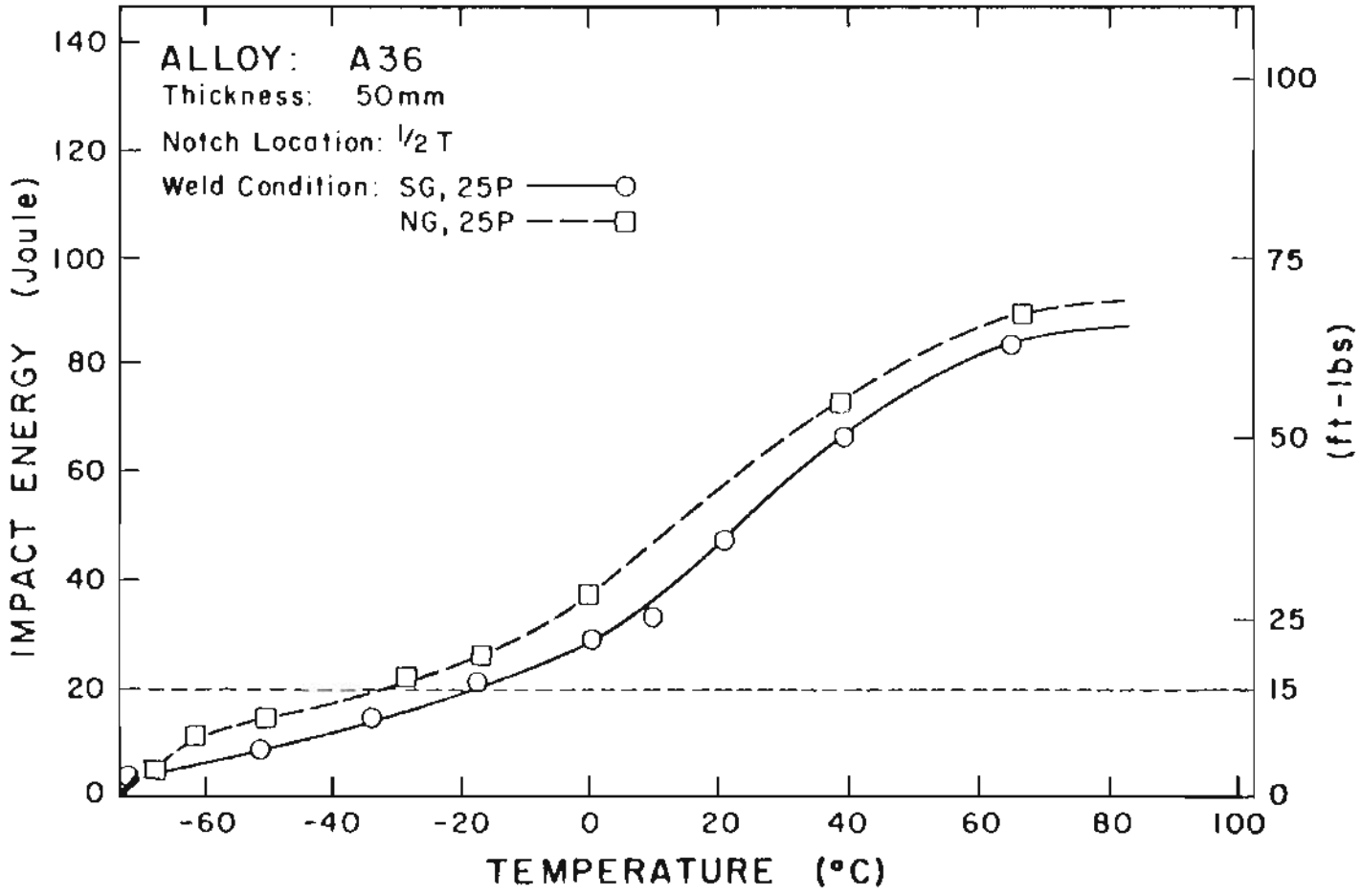

Fig. 58. CVN transition curves for A36 50mm thick ES welds
SG : Standard gap (32 mm) 25P : A36 matching filler
NG : Narrow gap (19 mm)

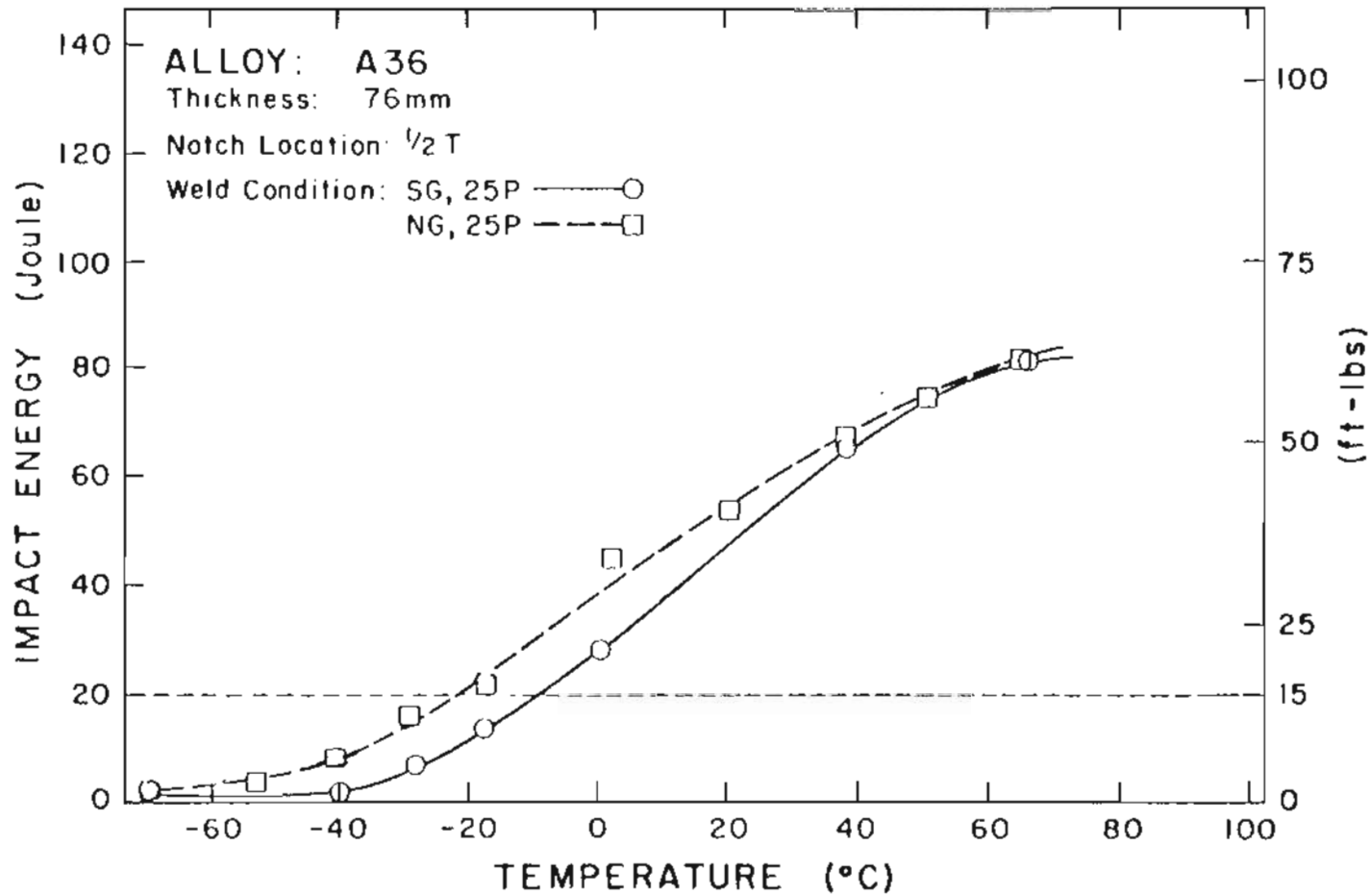

Fig. 59. CVN transition curves for A36 76mm thick ES welds
SG : Standard gap (32 mm) 25P : A36 matching filler
NG : Narrow gap (19 mm)

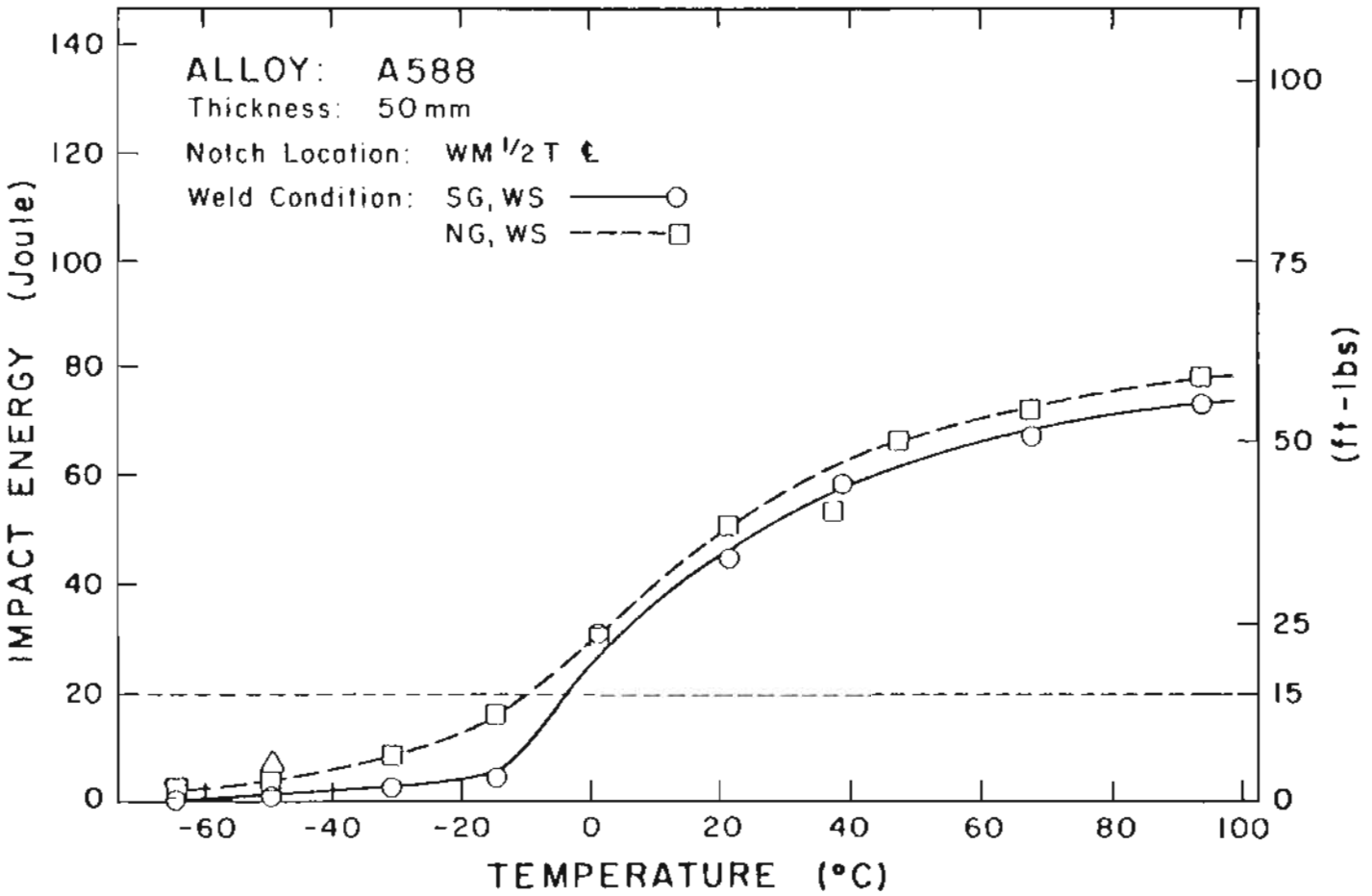

Fig. 60. CVN transition curves for A588 50mm thick ES welds
SG : Standard gap (32 mm) WS : A588 matching filler
NG : Narrow gap (19 mm)

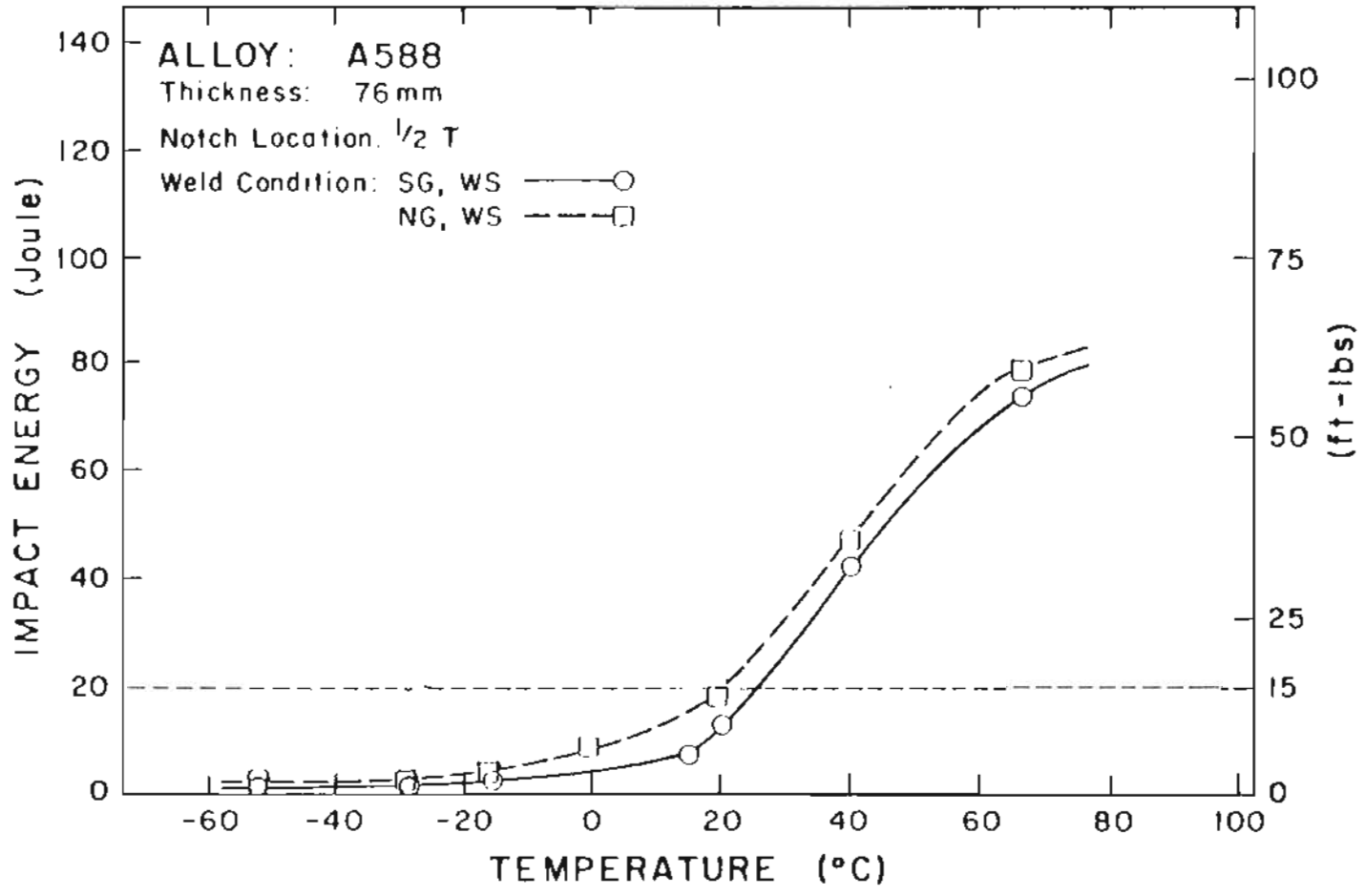

Fig. 61. CVN transition curves for A588 76mm thick ES welds
SG : Standard gap (32 mm) WS : A588 matching filler
NC : Narrow gap (19 mm)

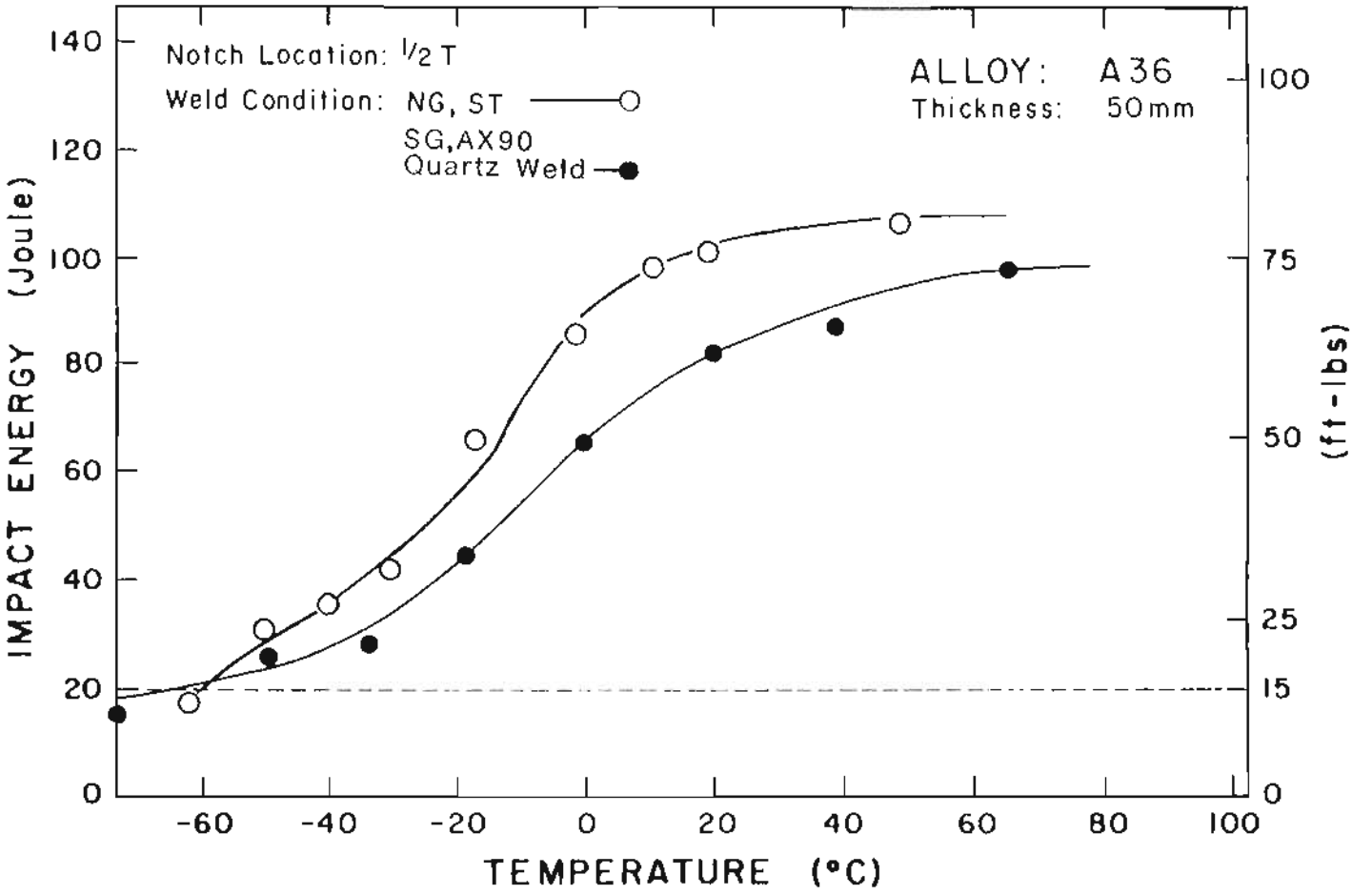

Fig. 62. CVN transition curve for quartz grain refined weld with alloy additions in A36 50mm thick

SG : Standard gap (32 mm) NG : Narrow gap (19 mm)
ST : Alloyed (Ni-Mo) powder cored tubular wire

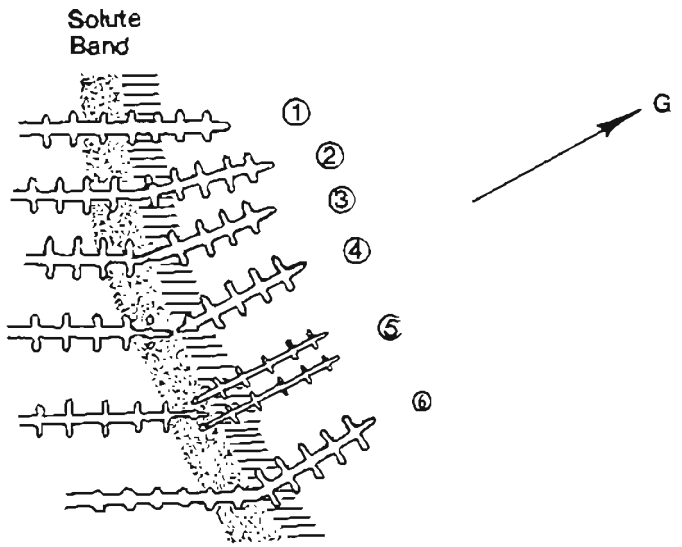

Fig. 63. Schematic representation of dendrite reorientation, renucleation and change of morphology at solute band

(1) dendrite arm growth through solute band
(2) direct dendrite arm bending
(3) partial dendrite arm remelting
(4) complete dendrite arm remelting
(5) new dendrite nucleation
(6) change of dendrite morphology

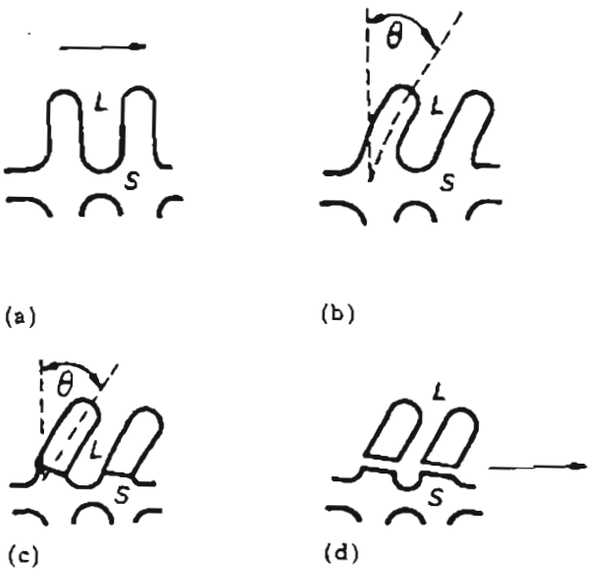

(a) an undeformed dendrite, (b) after bending, (c) reorganization of lattice bending to give grain boundaries, (d) for $\gamma_{gb} > 2\,\gamma_{S-L}$, the grain boundaries have been wetted by the liquid phase

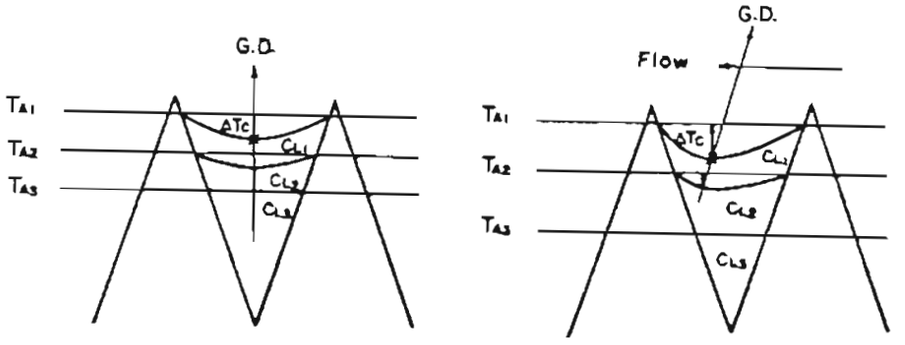

G.D. : Growth direction of dendrite
T_A : Actual temperature at a given level in the solidifying zone
C_L : Solute iso-concentration profile in liquid
ΔT_c : Degree of undercooling
X : Nucleation site of dendrite

Fig. 64. Effect of fluid flow on the growth direction of dendrite [Refs. Top: 28, Bottom: 50]

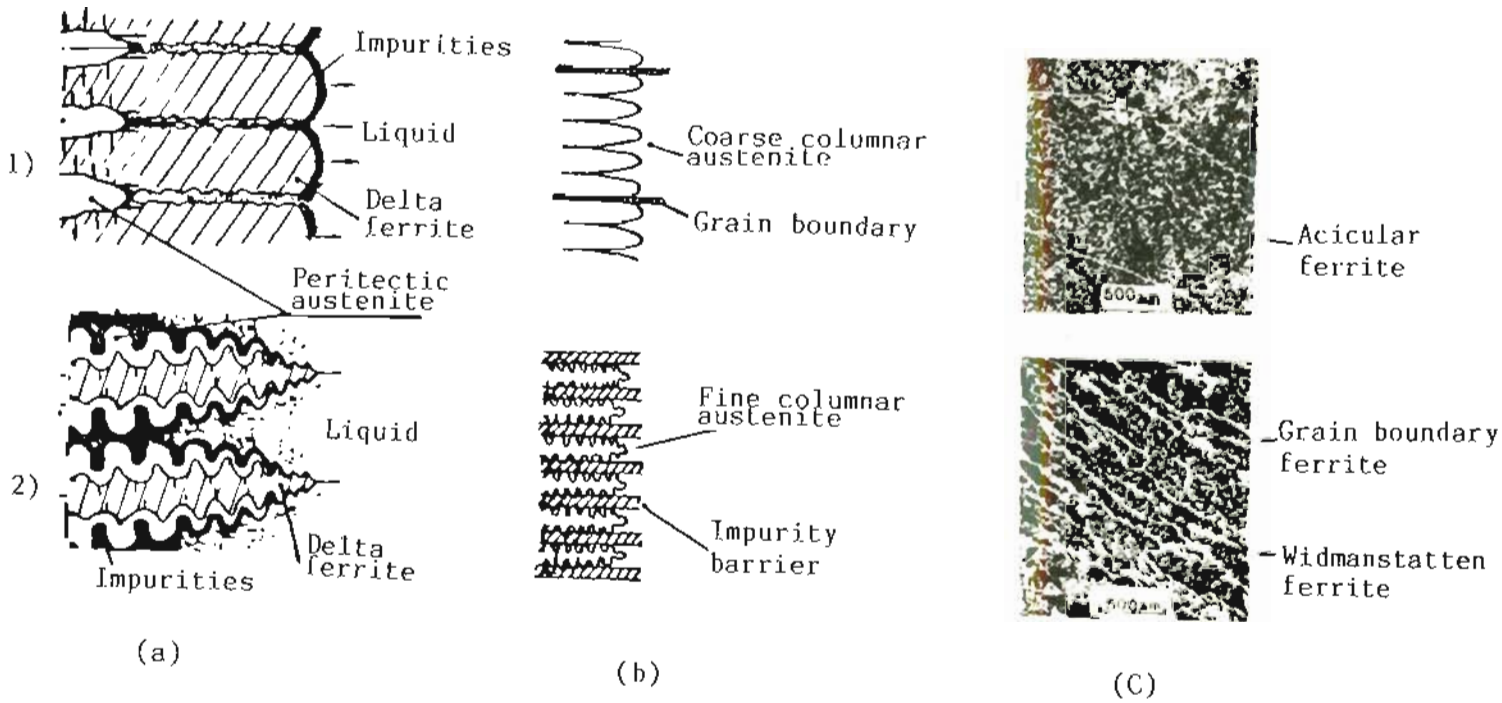

Fig. 65. Variation of morphology during solidification and subsequent transformation of (1) the cellular dendritic region, and (2) the columnar dendritic region for [Ref : 125]

(A) primary solidification morphology
(B) austenite grain structure, and
(C) room temperature microstructure

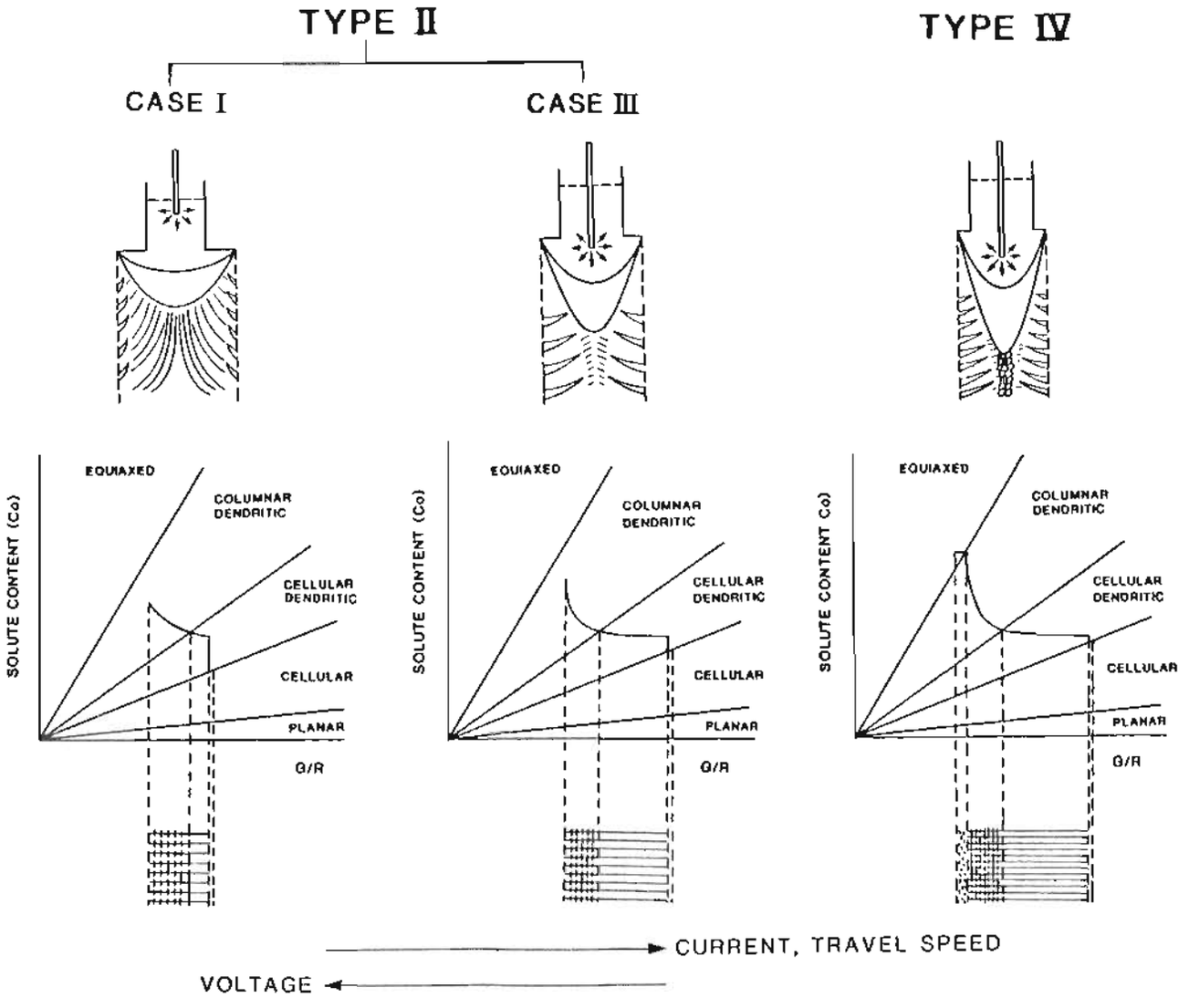

Fig. 66. Effect of welding conditions on the solidification structure formation

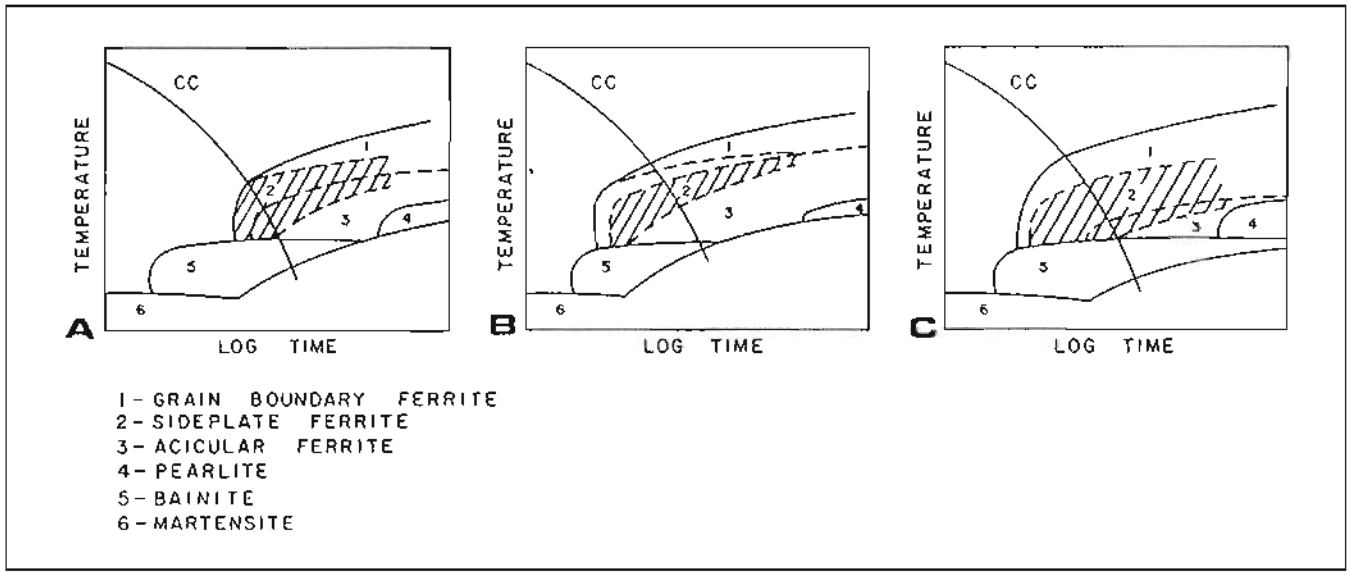

Fig. 67. Effect of oxygen content on the ferrite transformation [Ref : 97]

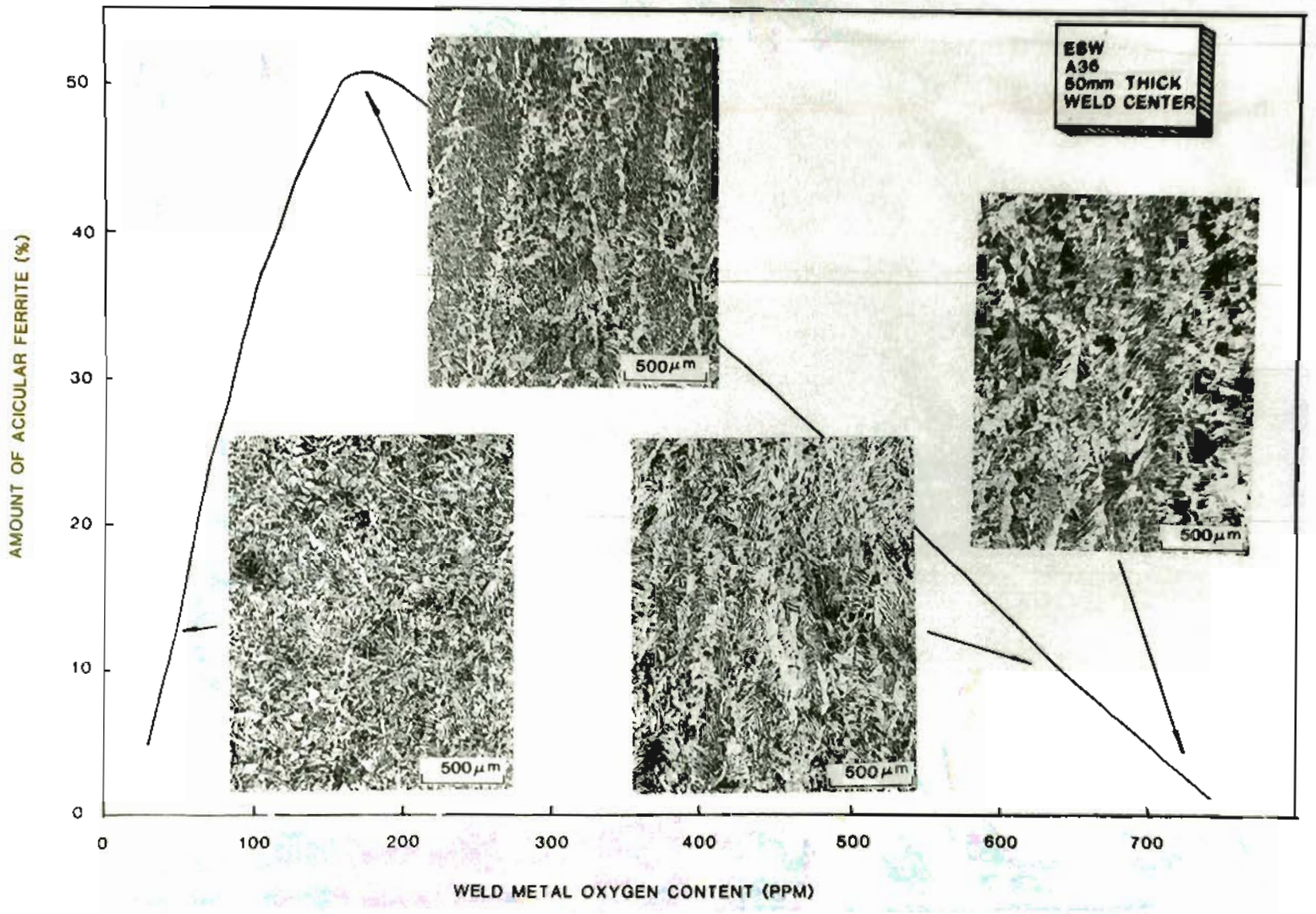

Fig. 68. Effect of weld metal oxygen content on the amount of acicular ferrite

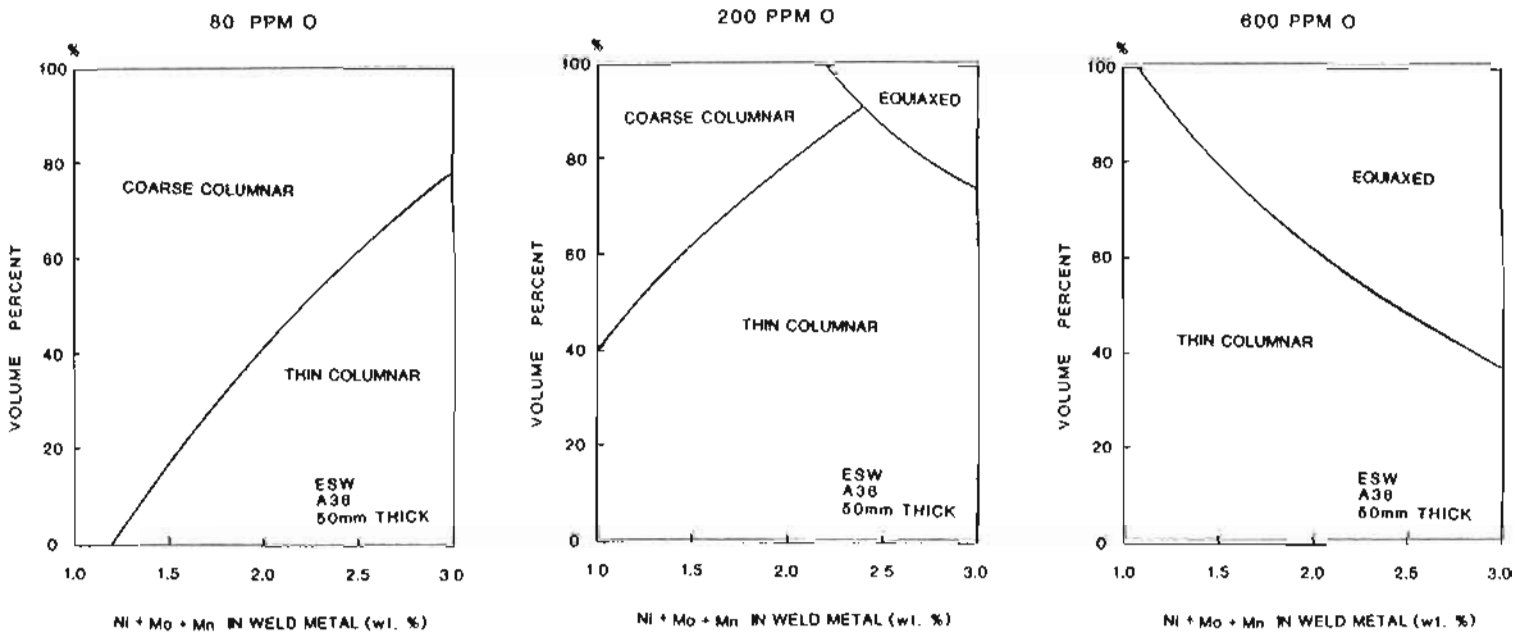

Fig. 69. Effect of alloy and oxygen contents on the volume percent of coarse columnar, thin columnar and equiaxed zones in weld metal

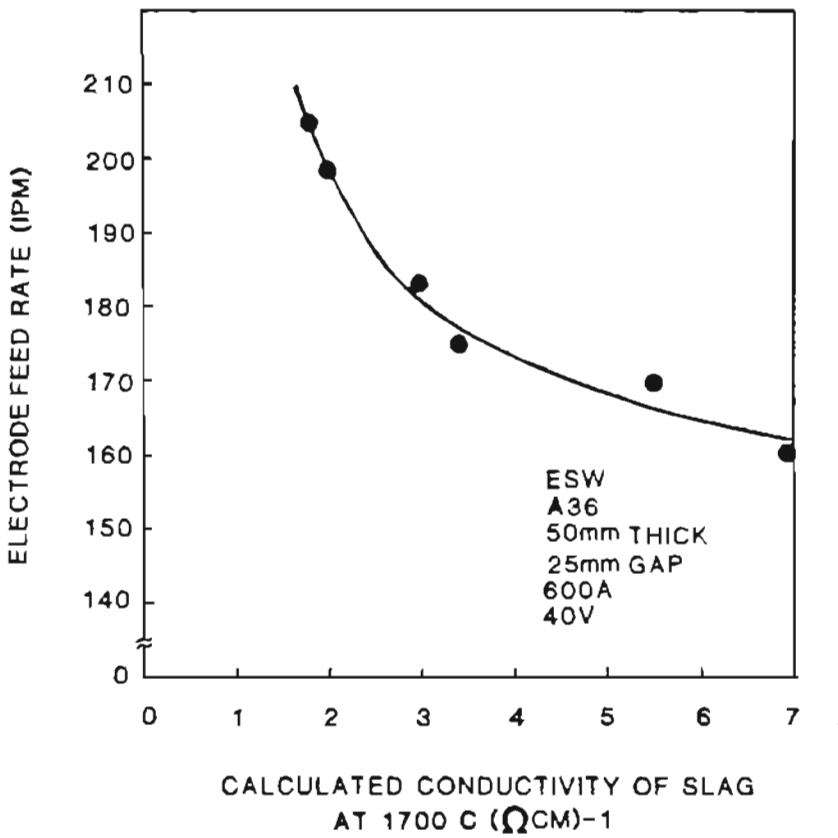

Fig. 70. Electrode feed rate as a function of slag conductivity

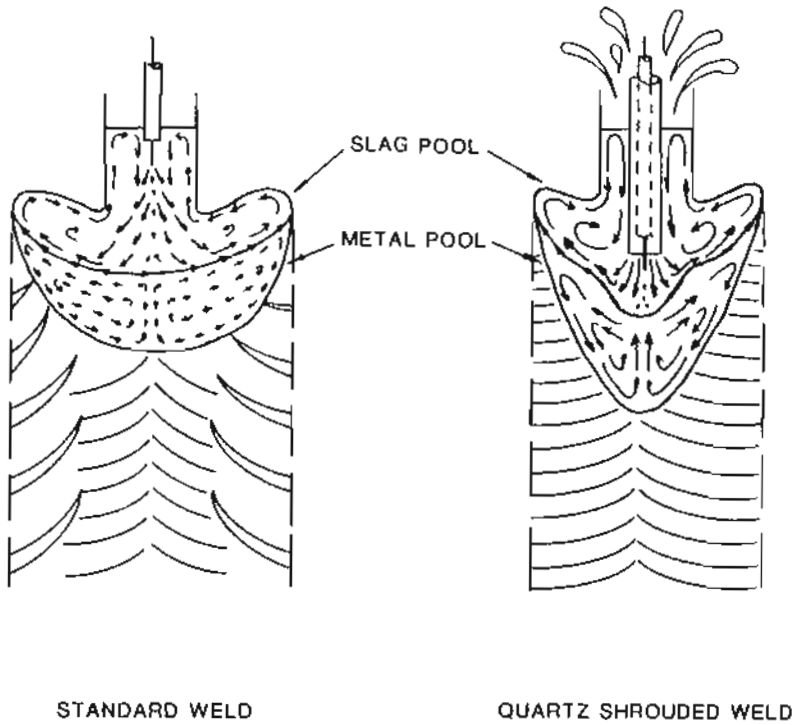

Fig. 71. Proposed fluid flow motion between standard weld and quartz shrouded weld

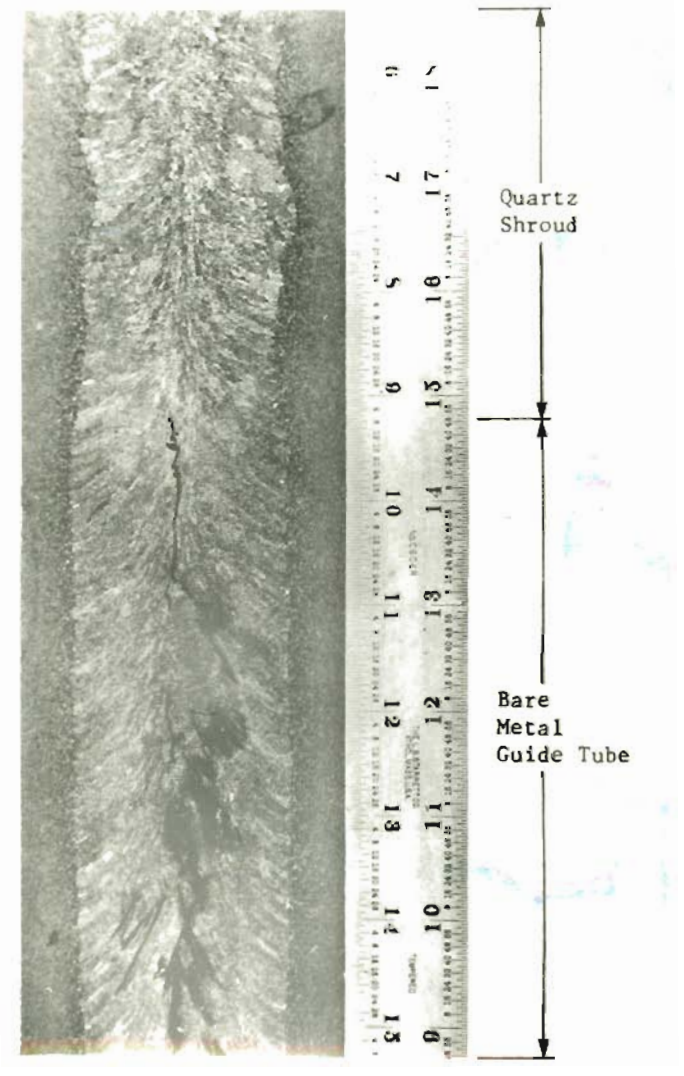

Fig. 72. Hot cracking resistance influenced by the addition of a quartz shroud during ESW [Ref : 4 and 5]

BIOGRAPHICAL NOTE

The auther was born March 7, 1953 in Chungnam, Korea

He received his Bachelor of Science degree in Metallurgical Engineering in February, 1978 from Hanyang University, Seoul, Korea.

In March 1978, he joined Korea Atomic Energy Research Institute (present name : Korea Advanced Energy Research Institute) in Seoul, Korea, where he engaged in research of ultrasonic to examination of materials, pre/inservice inspection (PSI/ISI) of nuclear power plant components, quality assurance/control (QA/QC) and also management responsibilities of PSI/ISI. He also participated in government QA auditings as a government inspector and ensured compliance with ASME code and regulatory requirements.

He has worked at Southwest Research Institute in San Antonio, Texas for 15 months (1979-1980) through International Atomic Energy Agency fellowship program. Responsibilities included ISI of Korea nuclear plant, unit 1. He also involved boiler inspection of over 15 paper mills and manual/mechanized examinations.

He joined the Oregon Graduate Center in the Fall of 1983, and finished the requirements for the degree of Doctor of Philosophy in Materials Science in August 1987. During his study, he presented and published several papers.

He is an ASNT-certified NDT Level III in the field of UT, PT and MT (Cert. No. DP 732) and also an AWS-certified welding inspector (Cert. No. 87040504).

The auther is married to Yeon-Sung and has one daughter of age 4.